ABSTRACT

Title of Dissertation: POLYMER ASSISTED ASSEMBLY OF INORGANIC MATERIALS FOR NEXT GENERATION BATTERIES

Marcus Carter, Doctor of Philosophy 2019

Dissertation directed by: Professor Efrain Rodriguez, Chemistry and Biochemistry Department

Nanoscale materials have desirable electronic features (e.g. high surface areas, reduced mass and transport paths) that can be harnessed for a variety of technological applications. In most storage devices, there is a particular interest in nanostructured electrodes and solid-state electrolytes. A key challenge is the reproducible fabrication of these nanostructured materials. Polymers are nanoscale materials that could be used for nanoscale fabrication with improved reproducibility. In this thesis I explored two nanostructured systems using novel polymer assisted assembly methods. I fabricate a nano-structured MoS_2 electrode and a nano-structured Li7La3Zr2O12 solid-state electrolyte with a garnet-type structure.

A clear redox mechanism for MoS_2 is currently being sought. Using our electrode, we propose a mechanism to understand the total or partial decomposition of the electrode and the formation of long soluble polysulfides. We complete a

fundamental study to determine the peaks on a cyclic voltammetry curve of nanostructured MoS_2. We resolve these peaks by building a novel but simple system of restacked MoS_2 with a conformal polyaniline (PANI) coating. We propose that the novel coating functions by absorbing, capturing, and promoting charge transfer (oxidization and reduction) of sulfur atoms remaining at the surface. Our data suggests that PANI acts as redox mediator. Redox mediators can be molecules or solid surfaces that aid in the charge transfer to redox species, traditionally oxide species. Our findings suggest that sulfur behavior dominates the redox chemistry at 0.7 V even earlier than the proposed deep discharge. We propose that longer chain polysulfides are formed through surface mediated interactions with persistent lattice planes of MoS_2.

Solid-state electrolytes like cubic garnet type $Li_7La_3Zr_2O_{12}$ offer safety advantages over flammable liquid electrolytes, which is especially significant to the advancement of high energy density battery devices. Garnet however is unstable in air, suffers from low preparation efficiency and degradation into a two competitive phases, tetragonal type garnet and lithium carbonate phases, which have low conductivity. For two polymers systems, poly(styrene)-block-poly(acrylic acid), PS(0.3)-b-PAA(0.7) and PS(0.8)-b-PAA(0.2), we synthesize cubic $Li_7La_3Zr_2O_{12}$ garnet. We systematically investigate the effect of growth parameters, temperature and excess lithium content, to find the optimized synthesis conditions of 750 °C for ~5 h with 60 wt.% and 65 wt.% excess lithium salt, for the polymer systems.

POLYMER ASSISTED ASSEMBLY OF INORGANIC MATERIALS FOR NEXT GENERATION BATTERIES

by

Marcus Carter

Dissertation submitted to the Faculty of the Graduate School of the
University of Maryland, College Park, in partial fulfillment
of the requirements for the degree of
[Doctor of Philosophy]
[2019]

Advisory Committee:
Professor Efrain Rodriguez, Chair
Professor Zhihong Nie
Professor Liangbing Hu
Professor Janice Reutt-Robey
Professor Mohamad Al-Sheikhly

Preface

Employing nanoscale materials instead of conventional bulk materials can lead to unique material properties or property enhancements, that cannot be found using bulk materials or from conventional preparation methods, such as localize surface plasmon resonance (LSPR) in gold colloids. For energy storage, nanoscale materials have been observed to have faster kinetics and increased capacity due to increased exposed surface area.

My work investigates known dimensional relationships nanoscale of MoS_2 and $Li_7La_3Zr_2O_{12}$ (LLZO) garnet. Nanoscale MoS_2 has shown high capacities, faster kinetics, and distinct redox behavior from the bulk. Nanoscale LLZO has been reported to be more resistance to decomposition in air. This work examines novel fabrication methods using polymers towards more uniform and reproducible products to better understanding of the chemistry related to their nanoscale dimensions.

I am grateful to the Nie, Hu, and Rodriguez Groups for their discussions, expertise, and experimental aid in the completion of these projects.

Dedication

I dedicated this dissertation to Maria Teresa Perez Cardenas, one of the best mentors, labmates, and friends. The efforts you gave and the contributions you have made are immeasurable. You had an immeasurable impact on the group morale that helped foster a sense of comradery.

Acknowledgements

This section was written to acknowledge those who have empowered me to get to this final step of the PhD process. If a reader happened to examine my dissertation, I want them to know how I arrived at this final step. I will forever be grateful, honored and humbled to have had the opportunity to pursue and complete my degree at the University of Maryland. Although the efforts to complete these projects and write this document were my own, the time, suggestions, instruction, criticism, and input which advisors, friends, and lab-mates provided were invaluable to improving the quality, and clarifying the concepts and refining the work that I have labored for. Though I do not have the space to thank everyone for their efforts and encouragement, I am convinced that it takes a community of support to reach a PhD. My pursuit was aided by the Chemistry Department who provided summer funding and by friends who helped cover my courses during conferences. There are a few individuals whose efforts, actions, and sentiments have been the greatest motivation to me and have enhanced my work tremendously.

To Rachel, who has read and revised countless important emails, manuscript revisions, dissertation chapters, abstracts and summaries. Who has listened to various presentations that are far from her interests and now learned more chemistry that she would ever care to know. I would like to thank you for the culmination of your many efforts, conversations, encouragement and steadfast belief. To the Wolf Pack, my gang of lively, housemates and colleagues who have commiserated, car-pooled, karaoked, cajoled me into game nights and cook-outs, encouraged and drove me to hospitals. Our adventures will be memories of this time that will make me smile.

This section of thanks goes to those who helped me to start my PhD journey and those who were influential in its completion. Thanks to my parents who taught me the value of education. Thanks to Dr. Nie and Dr. Hu for my graduate school experience, allowing me to work on interesting multidisciplinary projects, and hiring great scientists with variety of expertise and experiences for me to work alongside. The emphasis on innovation and going after new ideas and demonstration of concepts with a sense of haste has definitely molded my outlook on science: Do quality work fast. What I admire most about Dr. Nie is that he was able to integrate his diverse interest in polymers, microfluidics, biology, and films in to a research area. I hope that I can emulate this approach in my future work. Special thanks goes to Dr. Efrain Rodriguez, Dr. Marlon Walker, Dr. Linda Macri, and the writing center that gave me critical feedback on my writing, which was no doubt an arduous task. Thanks to Rishvi Jayathilake, Timothy Diethrich, and Tao Wu for their assistance with XRD data, refinements, and helping me to generate the model crystal structures. Finally, thanks to my scientific soul-mate, Maria, for giving constant pep-talks and feedback when I felt like trash.

Table of Contents

List of Tables

List of Figures

Figures from Appendix

List of Abbreviations

2D	Two-dimensional
3D	Three-dimensional
AFM	Atomic Force Microscopy
CV	Cyclic Voltammetry
LLZO	Lithium Lanthanum Zirconium Oxide
c-LLZO	cubic type $Li_7La_3Zr_2O_{12}$
t-LLZO	tetrahedral type $Li_7La_3Zr_2O_{12}$
MoS_2	Molybdenum Disulfide
NIBs	Sodium-ion batteries
NsM	Nanostructured Material
NsB	Nanostructured Battery
PANI	Polyaniline
SAED	Small area electron diffraction
SEI	Solid Electrolyte Interphase
SEM	Scanning Electron Microscopy
TEM	Transmission Electron Microscopy
TMD	Transition Metal Dichalcogenide
XANES	X-ray absorption near edge structure
XRD	X-ray Diffraction
XRF	X-ray Fluorescence analysis

Chapter 1: Introduction

1.1 **Nanoscale Structures and Networks in Nature**

Nature is filled with nanostructures. Nanostructures are materials with features having dimensions in the range of tens to hundreds of nanometers. In nature, these structures are not isolated in most cases, but are organized into precisely ordered, highly uniformed networks. The presence of a network is as important as the nanoparticle building block. Similarly, these networks have at least one dimension in the nanoscale, but can extend from over a few micrometers to tens of centimeters in length or width. The interest in fabricating and employing nanomaterials composed of nanostructures or nanoscale networks is to achieve lightweight and tunable properties similar to ones found in nature. Natural nanoscale networks often offer unmatched efficiency in response to stimuli such that despite the size, exhibited properties are measureable in the macro-world. Researchers are especially interested in nanomaterials that possess duality and/or multi-functionality in their properties. The duality in the response or properties, could originating from the nanostructures' ability to behave as individual units or as a network under particular conditions or stimulation.

Such networks with amplified responses to stimuli and multi-functional qualities can be found in the wings of the blue jay and the Morpho butterfly. From a materials perspective, these lightweight structures are characterized by their multi-functionality in unrelated areas such as hydrophobicity and colorimetric response. Studies found that the blue hues in the wings of the blue jay and the Morpho butterfly (figure 1) are a result of the nanostructures that are present on the feathers and in the wings, respectively.[1] The efficiency of color response is strong such that the color is quite vivid no matter the lighting conditions of the environment. This intense and shimmering hue is difficult to replicate as a paint or on digital screens. To replicate these properties scientists must create artificial structures, which replicates the morphology and shape of the nanostructure and the organization of the network.

While the structures and the networks of the Morpho wing are on the order of the nanoscale, some nature materials have subunits on the nanoscale, but networks on the micrometer scale such as naturally occurring solid-state materials such as graphite. For clarity, we view the smallest subunit that can create a response as a nanostructure, such as a single ridge in figure 1.1d, and the smallest 2D repeat unit as the network. As shown in figure 1, to cover the entire surface area of a butterfly's wings the full structure is composed of stacked networks in which the length and width are extended into the centimeter range.

Solid-state materials can be considered to be composed of both atomic subunits and structural subunits, but the atomic subunit does not always define properties of the material. Graphite's basic structural unit is graphene, a lattice with atomic thickness. Graphene is a monolayer composed of hexagonally coordinated sp^2 hybridized carbon atoms also has multi-functionality in unrelated areas such as hydrophobicity, high tensile strength, and high conductivity. The graphene is the stacked into networks to compose graphite. By exerting control over, the dimensions of the graphene subunits and the organization of possible graphene networks, scientist can tailor the properties of the artificial structure composed of graphene. These properties can be distinct from that of a single graphene unit and from bulk material (graphite). An exact number of layers of its subunit (graphene) does not define graphite. Instead, graphite is described by its properties and behaviors, which can be predicted by knowing the micrometer dimensions of the graphite sample.

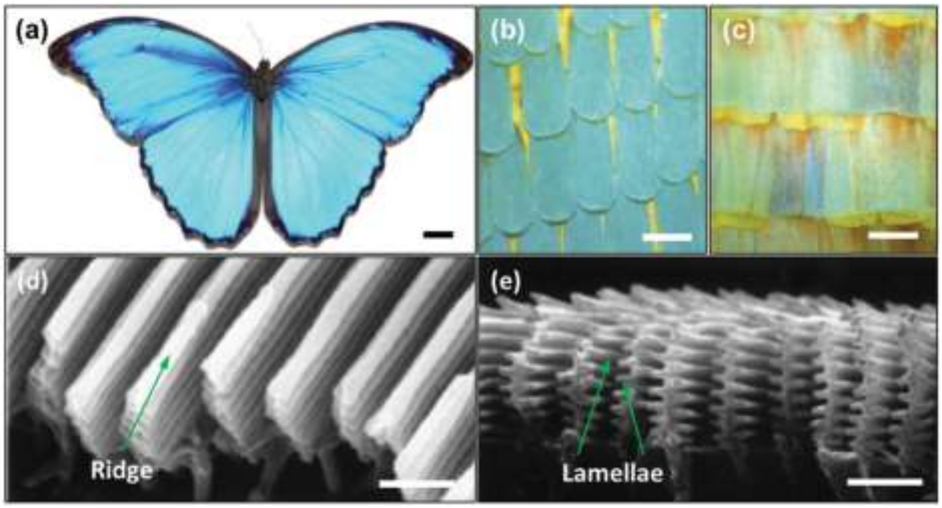

Figure 1.1. Nanostructures of the Genus *Morpho* a) An image of a specific species: *Morpho didius* butterfly showing its blue hue. Scale bar = 1 cm b) microscope image of an *M. rhetanor's* wing scales. Scale bar = 100 μm c) microscope image of an *M. didius's* wing scales. Scale bar = 100 μm d) SEM image (oblique view) of the *M. didius* male butterfly scale. Scale bar = 1 μm e) SEM image (cross section view) of the *M. didius* male butterfly scale. Scale bar = 1 μm. Image taken from ref 1.

1.2 Artificial Nanostructured Networks for Advance Batteries Applications

The implementation of organized nanostructures, similar to those discussed in section 1.1, towards **electrical energy storage applications** could result in the development of lightweight, multi-functional electrodes that are robust, highly conductive, and having high energy density.[2] The researchers that employ the strategy of incorporating nanomaterials within battery electrodes propose several obvious advantages over conventional battery material such as larger exposed surface area (high surface area to volume ratio) resulting increased redox reactions, shorten ion diffusion paths leading to faster kinetics[3-4] and potentially less charge transfer resistance, better cycling performance, improve conductivity, and longer cycle lifetimes .[2, 5-10] Additionally, a fundamental understanding of the complex redox reactions during battery cycling could be gained by minimizing excess active material, employing a simple fabrication method, and forming well-defined nanostructures.[11]

The methodology of fabricating (nano-structuring) these materials with at least one dimension in the nanoscale encompasses various techniques such as vapor disposition[12], lithography, soft-templating, self-assembly, electrospinning, solvothermal/hydrothermal methods, aggregation and crystallization[6, 13-15]. These techniques results in a variety of structures and morphologies with ranges of complexities and compositions such as single crystal and polycrystalline mosaics, nanoparticle and nanotube arrays, and novel nanostructures with complex forms and hierarchies.[13] Nano-structures for batteries have shown great potential to advance battery performance. Electrodes with nano-sized features have been fabricated with precise and uniform arrangements and have shown enhancements in battery performance attributed to their increased surface area and quantized dimensions. However, increased surface area can potentially lead to drawbacks. Researchers have predicted that an increased surface area can leading to increased side reactions and instability, especially in a thick solid electrolyte interphase (SEI). Recent studies have shown the feasibility of the applied nanostructure approach. The improvements in capacity and transport kinetics of reported battery systems suggest that the nanostructures provide considerable more positive contributions over the potential drawbacks.[12]

The fabrication of artificial structures can be completed by a nanopatterning methodology, forming the nanostructure and network simultaneously one layer (lattice) at a time, or a nanostructuring methodology, which relies on a piecemeal fabrication, by forming the structures first and organizing them in subsequent steps. Figure 2 shows a survey over various nanopatterned electrodes. We define nanopatterning as an approach that attempts to fabricate highly uniform nanoarrays by simultaneously constructing nanostructures and their networks. The nanopatterned structures are generally created through top-down methods such as deposition, lithography, and etching methods. Templating can also be categorized as a nanopatterned approach, because it replicates an original structure, which is generally created using top-down methods. The templating approach consists of covering an original structure (template) with a new, desired material to copy the shape and morphology, and removing the original material through burning or etching.

Of the two nano-structuring techniques, nanopatterning offers the most consistent strategy for fabricating active material with precise locations and morphologies, leading to more reproducible and reliable battery performance. However, these artificial structures lack versatility, atomic precision, and the possibility for large-scale production. The fundamental drawbacks of lithography and deposition processes limits the practical use of nanopatterning fabrication techniques and, thus, are cost prohibitive.[16]

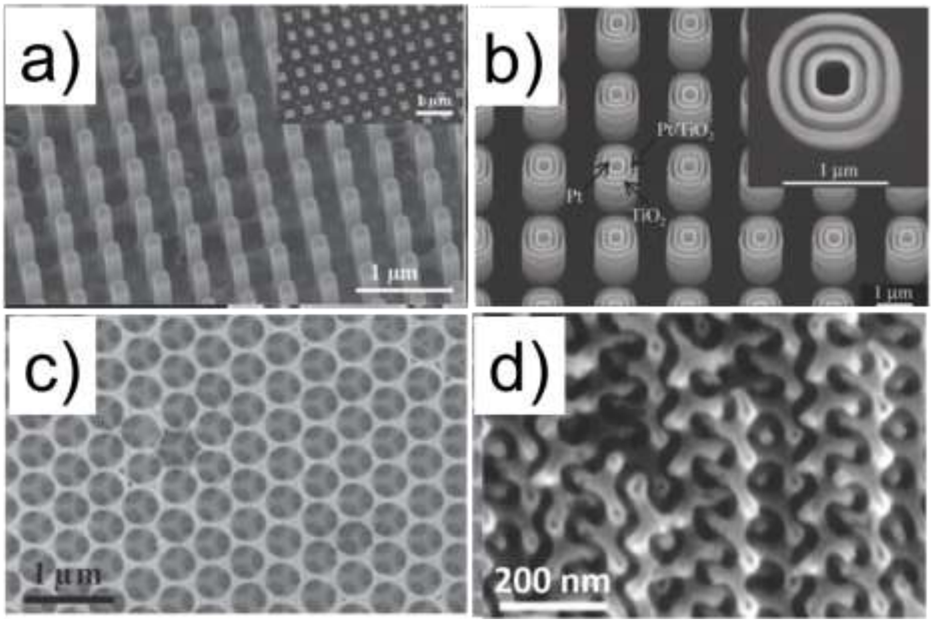

Figure 1.3. Various nanopatterned electrodes for electrical energy storage.[12]

The selection of the design strategy and fabrication process are critical to actualize nanoscale battery devices. Due to the various limitations, as seen above, the fabrication processes of many advanced batteries with nano-scale features are not commercially viable. The lack of scalable fabrication technique is compounded by the lack of fundamental understanding of redox chemistries and mechanisms of nanostructured batteries. To actualize nanostructured batteries, the obstacles such as production cost, scalability, consistency, and fundamental redox mechanism need to be considered in the design approach before the selection a fabrication and assembly process. Nanopatterning techniques have yet to offer a detailed strategy to scale-up this approach towards advancing a renewable energy based society.

1.3 **Self-Assembly Nanofabrication**

With the above-mentioned limitations of nanopatterning (top-down) techniques, more practical and actualizable nanofabrication methods must be considered. The shift toward bottom-up fabrication using solution based self-assembly approaches has become one fast growing research areas to align and precisely arrange building blocks for electrical energy storage.[16] Solution-based nanofabrication offers advantages over nanopattering methods such as increased scalability, versatility, and easier implementation from the bench-top to industrial manufacturing processes as current manufacturing techniques (*i.e.* roll-to-roll) operate using solutions. Solution-based methods are represented by self-assembly, electrospinning, solvothermal/ hydrothermal, aggregation and crystallization methods.[6, 13-15] Many of these nanostructuring approaches are versatile as they can be mapped on to existing processes and modified to accommodating various building pre-modified, un-modified, *in situ* created before the assembly process. Among published articles on MoS_2 electrodes, there is a growing preference for solvothermal and hydrothermal methods as they seem to be correlated with higher battery capacities, especially for the MoS_2 electrodes. These methods employ the addition of reagents in aqueous or non-polar liquids, followed by heating in a sealed autoclave toward finding novel electrode material. By controlling the ratio of reagents, the solvents conditions, and the heating rate and final temperature, the goal is to find a local thermodynamic minimum state with either a unique composition or morphology. The advantage of this method is that the heat process allows for the fabrication of novel, usually metastable, states that can be tested as electrodes for systematic method to finding and identifying potentially useful materials.

1.4 **Stacked MoS_2 Nanostructures as Electrode Material**

While novel designs and improving performance values have always been a focus of battery research, the focus on achieving improved measurables over fundamental study is even more pronounced for some emerging nanostructured systems, such as MoS_2.[17] The current solution based methods, though they offer increased scalability and versatility over nanopatterning methodologies, fail to deliver critical information needed to continue to advance MoS_2 electrodes toward wide spread adoption.

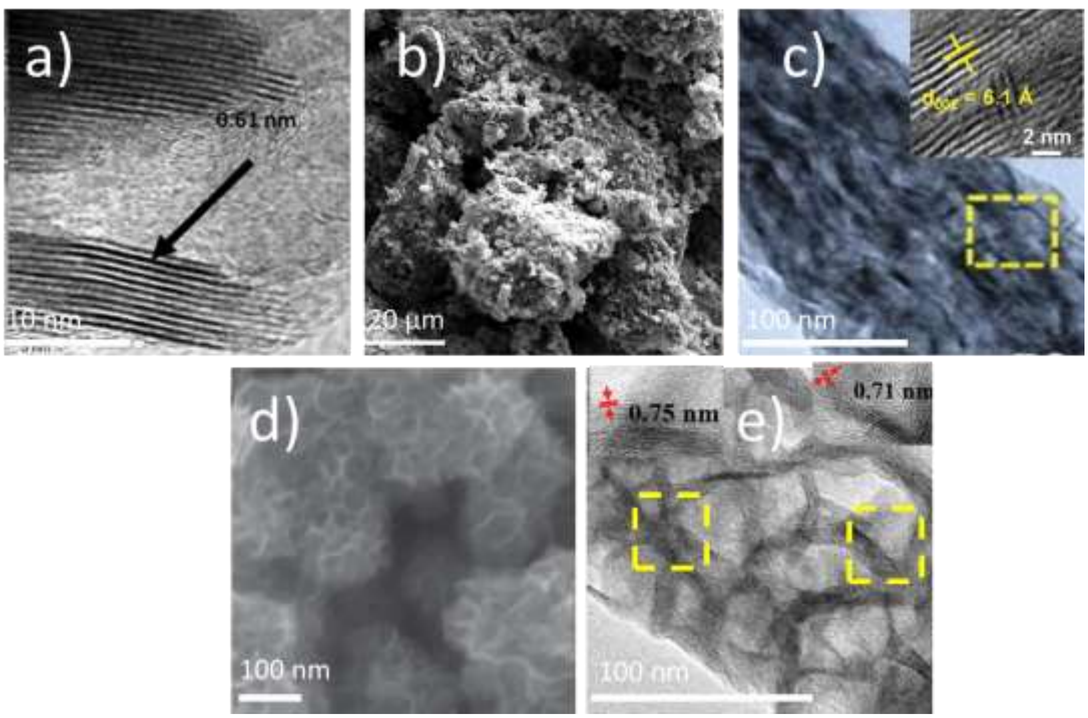

Figure 1.2. Representative micrographs showing the morphology of nano-structured Na-MoS_2 electrodes. (a) TEM and SEM images of restacked PEO/ MoS_2 nanocomposite with expanded spacing after the incorporation of PEO, respectively.[18] (c) Electrospun TiO_2-coated MoS_2 nanofiber electrode, with an inset showing interlayer spacing.[19] (d) MoS_2/carbon nano-spheres[20] (e) MoS_2 porous nanofiber electrode[21]

Recent articles have reported battery capacities that are approaching the theoretical capacity of 670mAh/g for the MoS_2 electrode. However, the performance improvements seem highly variable, even in the research that employs similar morphologies from similar synthesis methods (*i.e.* hydrothermal and solvothermal).[5, 21-27] The variability could be partially attributed to a lack of knowledge of a consensus of compatible battery components to match with novel experimental electrodes.[17] However, for the MoS_2 electrode there are no clear design principles for electrode morphology and even formation of the intercalation products are currently contested.[5, 19, 27-28] Variability in battery performance of the nanostructured batteries could also result as a function of the preference toward hydrothermal and solvothermal as assembly techniques. These techniques often produce a final result of which the performance can be electrochemically tested, however, these methods have no way to monitoring the reaction's progress which limits the ability to reproduce a consist product. The addition of larger quantities of carbon additives have major trade-offs; they reduce mass loading of MoS_2 and lower energy density of the electrode. Further, increased carbon additives often obscure cyclic voltammetry (CV) peaks and lead to differences in phase of MoS_2 on the electrode, decreasing potential insights into ongoing redox chemistries. Specifically, due to their improved charge transfer versus synergistic effects of increased amount of inactive components, graphene-based carbons obscure the mechanism for capacity gains.

MoS_2 redox chemistries have always been complex. MoS_2 was largely abandoned as an insertion material in favor of the study of simpler systems such as TiS_2 due to its complex redox reaction.[29-30] In response to electron transfer, which drives intercalation of ions, the atoms within the lattice of MoS_2 rearrange and the layers of the structure shift with respect to each other, as the structure undergoes redox-driven ions intercalation. This process stands in contrast to simpler chalcogenide compounds , such as TiS_2 which experience slabs shifting at high ion concentration, but no intra-lattice rearrangement. The reorganization of the MoS_2 the lattice is known as the transition from the 2H to 1T crystal structure and it places significant strain on the lattice structure. Continued galvanic cycling leads to irreversible changes such as the delamination of single MoS_2 layers, the complete disorganization of the lattice, and the formation of alkali sulfide species.[25, 31] Each of these phases can be electrochemically active. Single layers can continue to absorb and desorb ions and the amorphous phase can undergo pseudo-intercalation or pseudo-staging.[30, 32] Finally, in an environment of high ion content (low voltage window <0.1 V) the MoS_2 electrode can undergo dissolution releasing sulfur.[14] The formation a sulfur product creates an additional set of redox reactions that occur over the same voltage range as MoS_2 allowing for the possibility of sulfur shuttling, side reactions between polysulfides and the electrolyte, and coupled reactions between MoS_2 lattice planes and polysulfides.[28] These possible reactions have led to a continued debate over the peaks that occur on cyclic voltammetry curves.[33-34]

1.5 General Review of Battery Concepts

Now that we have discussed advancements in battery materials, it is important to review the fundamental components and process of batteries. Batteries are devices that allow the flow of electrons through a connection of electrodes of differing reduction potentials. The difference between the two potentials is known as the cell potential. The flow of electrons is initiated and sustained due to electrochemical reactions occurring at the electrodes' surfaces, with reduction at the cathode and oxidation at the anode. These electrochemical reactions distinguish a battery from a capacitor and are evident by the peaks in a cyclic voltammetry (CV) curve, figure1.3.

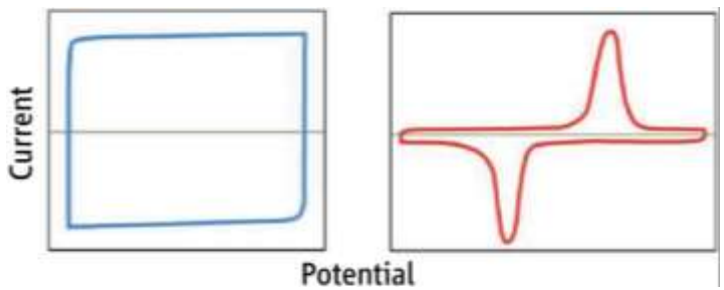

Figure 1.3. Taken from [35]. The schematic illustrates the difference between the profiles a capacitor (left) and a battery (right) through cyclic voltammetry**.**

In a simple one-electron transfer battery, the peak on the reduction side is equal in magnitude to the peak on the oxidation side. However, the constructed research coin cell, half-cell, shows more complicated curves. For clarity, this proposal defines charging as the process by which sodium ions are intercalated into the structure of the anode and discharging as de-intercalated or removal of the sodium ions, figures 1.4 and 1.5.

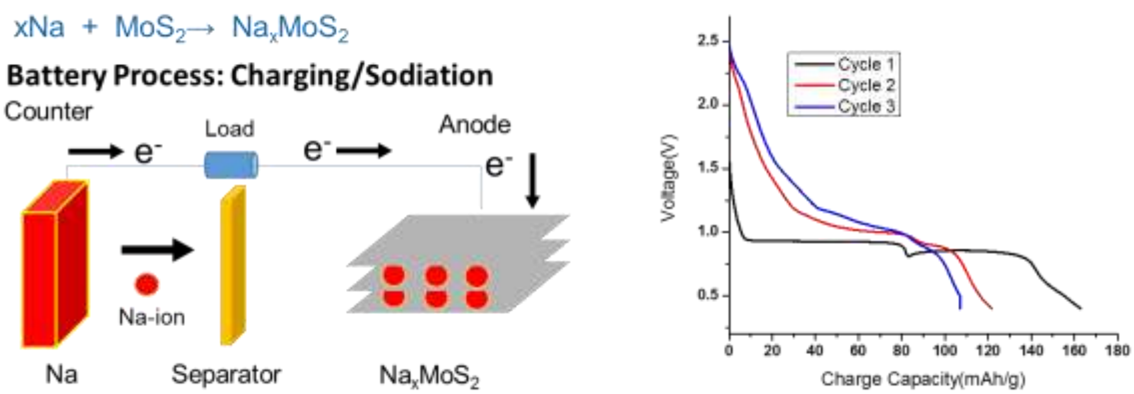

Figure 1.4. Schematic showing the flow of sodium ions into the stacked flakes of MoS_2 and as the ions are cycled, the battery profile resembles declining curve with two prominent plateaus.

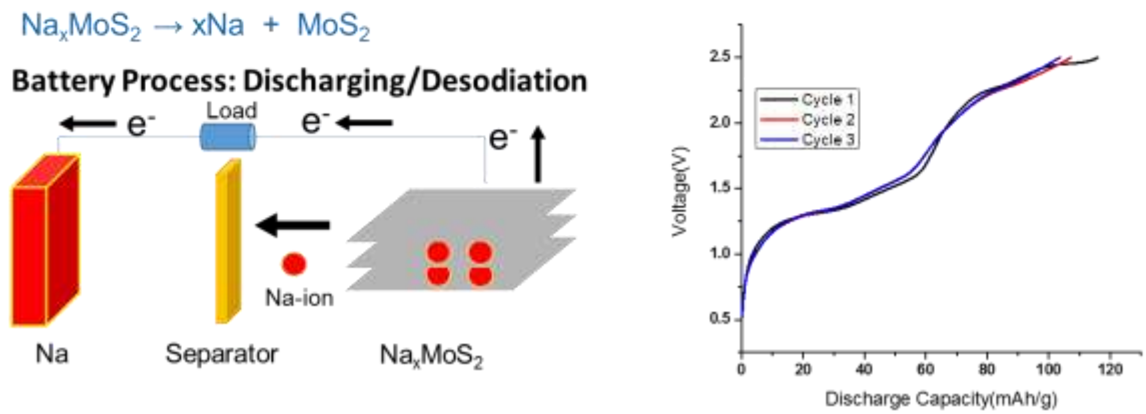

Figure 1.5. Schematic showing the flow of sodium ions out of the MoS_2 lattice (desodiation) and as the ions are cycled, the battery profile resembles inclining curve with plateaus that mimic that of the charging profile.

This movement of ions and the formation of the solid-electrolyte interphase (SEI) can be sensed as peaks on the CV curve. The SEI is the formation of an ionically conductive, and electronically insulating film on the surface of primarily the anode. The film is formed as a result of chemical reactions with the electrolyte. A favorable SEI is beneficial because it prevents further reaction of the electrolyte. However, unfavorable SEI or too thick SEI leads to continued electrolyte decomposition and increase irreversible capacity loss or slower ion diffusion, respectively.

The specific type of battery this research aims to construct is a secondary (rechargeable) insertion battery. Insertion batteries are a category of batteries in which the ions are embedded in the structure of the electrode. The most famous insertion battery is the lithium ion battery, first composed in the 1970's.[26]

1.6 Garnet and Garnet Composites Nanostructures as Electrolyte Material

Garnet is Garnet is a promising solid-state substitute for liquid electrolytes in next generation lithium batteries and a required component to construct high voltage batteries. High voltage batteries are incompatible with liquid electrolytes as the voltage will cause the combustion of the organic electrolytes. Garnet, an oxide composed of lithium, lanthanum, zirconium, and oxygen (LLZO) has a three dimensional lattice structure. The general formula is $Li_7La_3Zr_2O_{12}$ and sometimes includes a dopant such as alumina or niobium. Garnet has advantages over other solid-state systems as it has a large lattice constant, which allows the structure to accommodate higher lithium ion concentration. Additionally, the structure has a lower degree of chemical interaction between the Li^+ ions and the other lattice constituents, and higher densification.[36]

Similar to many other battery components, solid-state electrolytes can be nanostructured. Nanoscale garnet suffers from a variety of problems. Some of the problems occur in response to the solution-based approach while other problems are inherent to the nature and physical properties of the material. Like the assembly process of MoS_2, garnet fabrication lacks a systematic approach or machinery to actualize the assembly of crystalline building blocks. The nature of garnet imposes a set of unique constraints on the fabrication process. The distinction in this fabrication process compared to that of MoS_2 (above) is the calcination or required heating step to convert the precursor in the garnet structure. The fact that the material is being transformed places significance on the starting composition/ starting precursors.

The inherent challenges of garnet that are the focus of current research are low conductivity, high interfacial resistance, and high density, which lowers the overall energy density of emerging battery systems. Garnet has a general conductivity range of 10^{-3} to 10^{-6} S/cm with the highest conductivity in the range of 10^{-3} to 10^{-4} S/cm, which is still orders of magnitude lower than liquid electrolytes at ~10^{-2} S cm^{-1}.[37]

1.7 **Polymer Assisted Assembly**

An understanding of the fundamental principles of homopolymers and block co-polymers assisted self-assembly is the foundation for studying and designing more complex nanostructured batteries. Self-assembly is the spontaneous aggregation of molecules or building blocks into stable, three-dimensional structures, using inherent or induced molecular interactions such as electrostatic, van der Waals attractions, hydrophobic/hydrophilic interactions, hydrogen bonding, and π–π donor–acceptor interactions. In addition to processing cost, the implementation of self-assembly of nanostructure batteries provides versatility as a key advantage over nanopatterning.

The packing parameter refers to the fundamental principle of the formation of various structures and morphologies. The packing parameter is a semi-quantitative understanding of the volume and length of the hydrophobic segment in amphiphilic polymer to determine the morphology of the assembly. The packing parameter is a ratio given by the equation $\rho = v/(a_o)(l_c)$, where v is the volume of the hydrophobic segment, a_o is the cross-sectional area of the head group, and l_c is the length of the hydrophobic segment. Figure 1.6 represents the possible micelle morphologies including spheres, cylinders, and vesicles. Spheres are favored when ρ is less than

1/3, cylinders when 1/3 < ρ < 1/2, vesicles (flexible lamellae) when 1/2 < ρ < 1, and planar lamella when ρ =1. Additional, inverted structures are formed when ρ >1.[38-40]

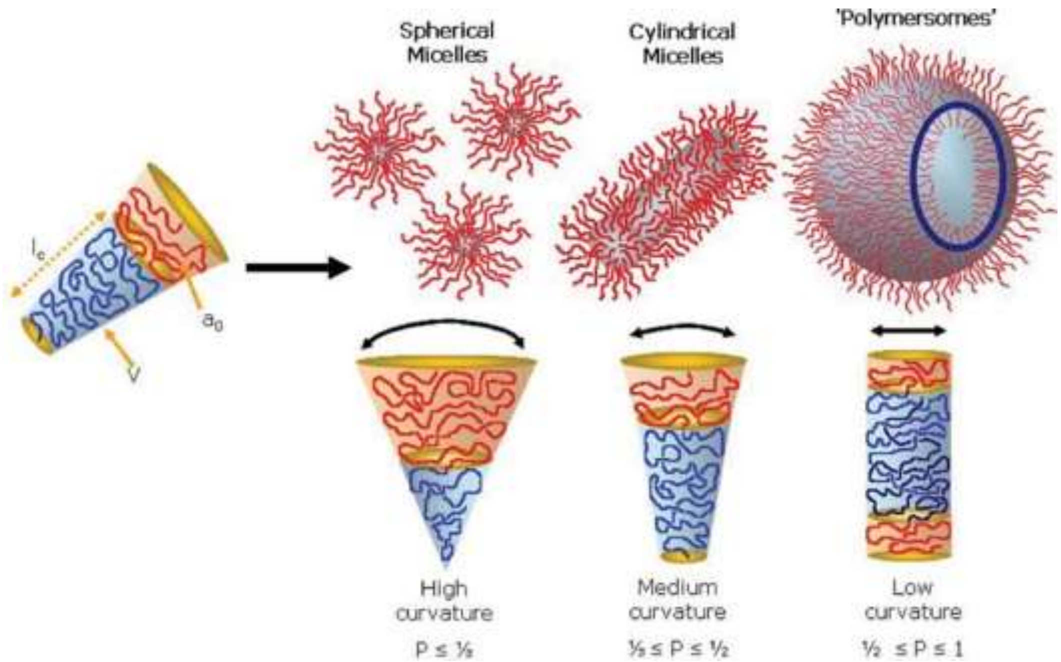

Figure 1.6. Self-assembled structures formed by amphiphilic block co-polymers[38]

1.8 Scope of the Dissertation

While the cycling lifetime, capacity, discharge and charge rate of NsBs show better performance compared to traditionally prepared (bulk) batteries, more improvement is needed to advance nanoscale batteries. This dissertation will discuss the rationale and fabrication of a MoS_2-PANI composite electrode to understand the reaction mechanism and synthesis of a garnet $Li_7La_3Zr_2O_{12}$ electrolyte using polymer assisted self-assembly. With both systems, the polymer has a multi-functionality to help in the assembly of material. Additionally the polymer functions as a sensor on the surface of MoS_2, while the polymer for the garnet system sequesters and acts as a micro reactor/template in order to control the grain growth. Using a simple-stacked assembly structure, we employ PANI to monitor the surface of MoS_2 strategies to gain insights on nano-scale MoS_2 chemistries. We utilize block co-polymer micelles to maintain the grain-size of a $Li_7La_3Zr_2O_{12}$ solid-state electrolyte as a way to preserve morphology and constrain grain size during the sintering process.

Chapter 2: Experimental Techniques

2.1 **Introduction**

The overall theme of this thesis and the field of nanomaterials is to design materials where the properties are increasingly directed by a sublevel of organization that resides in a range of ten to hundreds of nanometers. To study the resultant properties and structures of nanostructured materials and their differences from the bulk, techniques with the capability to monitor on micrometer and nanometer scale are required. Currently, few established techniques exist to provide *in situ* studies of the chemistry of these structures during cycling.[41] Therefore, traditional characterization methods must be enhanced with combinations of distinctly different, but complementary techniques. For our work, this combined approach is needed to understand the extent of the disorder and the relationship between the morphological disorder (lack of coherent stacking) and the reaction mechanism of MoS_2 battery material. Traditionally, MoS_2 and Transition metal dichalcogenides (TMD) bulk solids were investigated by x-ray diffraction (XRD).

Many bulk compounds in their natural state are crystalline, having repeating arrays of atoms or molecules. Perfectly aligned arrays created bulk crystals, which can range from a few hundred nanometers to a few centimeters. The spacing (internal organization) of the crystal is on the order of a couple of angstroms (Å) to hundreds of picometers (pm) for atoms and molecules, respectively. This fundamental understanding indicates that the arrays are composed even smaller repeating clusters of atoms or molecules. The smallest repeat element is called the unit cell. The unit cell is defined by the dimensions a, b, and c and the angles α, β, and γ in real space.

There are seven possible independent unit cell types and 14 unique arrangements (Bravais lattices) for three-dimensional crystals. The symmetries and dimensions of the Bravais lattices, given by their parameters and angles, are primarily responsible for the diffraction patterns found empirically.

2.2 **Diffraction**

Diffraction is a technique to study the crystal structure (and/or the unit cell) of a compound by probing the structure with an incident beam of electromagnetic radiation. This technique utilizes the wave nature of electromagnetic radiation. Diffraction of a wave occurs when the incident wavelength of light is around the same length of the subunit spacing. For instance with ionic solids, the incident x-ray beam ejects a core electron from an atom causing vacancy, which is filled by a higher energy valence electron. In the process of filling the vacancy, the electron emits a photon with an energy in the x-ray region. The x-rays detect from the sample that meet a special condition are said to be reflected. The x-ray is said to be reflected when it strikes a detector position at the same angle (Bragg's angle) of the sample as the incident beam. In order for the wave to be detected, it must be undergo constructive interference. Figure 2.1 shows a schematic illustrating the diffraction process.

In the figure 2.1, the lattice planes of atoms are position at some interval a part, d. When rays of radiation with wavelengths, λ, and angles of incidence, θ, meets the criteria of Bragg's law, equation 1, they constructively interfere.

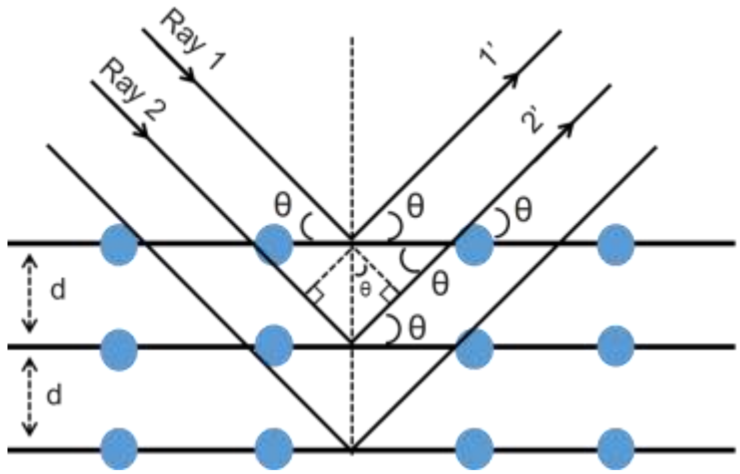

Figure 2.1. Illustration of a sample being probe by incident radiation.

Equation 1. Bragg's law is $n\lambda = 2d\sin\theta$.

The constructive inference leads to pattern of bright and dark spots that can be transcribe into a histogram. The histogram called a diffraction spectrum plots the intensity of the reflected wavelength versus degrees as peaks (diffraction peaks). The intensities are labeled with arbitrary units, while the position are denoted by 2θ angle. The data organized into a this form (spectrum) is most often used for the XRD technique.

Each material has a unique arrangement of atoms, which produces a characteristic spectrum. In the field of material science, the collection of peaks in a spectrum are used as a diagnostic tool. It is important to mention that one or two peaks alone is not a positive identification of a compound. Multiple peaks are needed for conclusive identification.

The shape, intensity, and position of the peaks indicate important parameters of the material. The presence and sharpness of the peak demonstrates the relative amount of stacked layers or lattice planes present. Additionally, the peak intensity (or ratio of peak intensity) provides information about the orientation of the stacking layers and the size of the crystals or crystallites under investigation. Shifts or comparisons of designated peak's angle between a sample and a known standard or diffraction peak of a control determine the difference of the lattice spacing between the sample and the unknown.[42] Reciprocal space (2θ) is inversely proportional to real space. Therefore, a peak's position would shift to a lower angle with an increase in average interlayer spacing. Conversely, a peak's position would increase to a higher 2θ degrees when there is a decrease in the average interlayer spacing of a compound in real space. Decreases in the intensity of a peak and broadening of a peak's shape could also occur indicating the partial or complete removal of stacked lattices.

Both X-ray and electron diffraction techniques were utilized in this study primarily to confirm the presence of the polymer coating and fabricated structure, and to detect phase transformations of the electrode material. Changes in an XRD peak's shape, intensity, and position are directly linked to structural changes during battery cycling.[42-44] The detailed theory and relation to reciprocal space can be obtain by examining the following references.

There are two types of x-ray diffraction, single crystal diffraction and powder diffraction. Only powder is used in this study, however, single crystal diffraction, will be mentioned in this section for thoroughness, but will not be discussed in depth.

2.2.1 Powder Diffraction

Many of the fabricated nanostructures are evaluated with the powder diffraction method. Generally, the samples investigated by this diffraction method are composed of crystallites in all possible orientations. When the incident beam hits the sample, multiple reflections occur. If the reflections meet the Bragg's criterion, they constructively interfere to create a signal. This unique composition allows the sample to remain stationary while the incident beam scans over a range of angles unit all possible reflections are probed and the diffraction spectrum is recorded. The powder diffraction in this dissertation was collected on a Bruker D8 X-ray diffractometer with Cu Kα radiation source with a wavelength of 1.5418 Å.

2.2.2 Single Crystal X-ray Diffraction (SCXD)

In contrast to the sample above, a single crystal has only two reflections when hit with the incident beam. Therefore, to record an entire spectrum, the sample requires rotation. The sample is placed on a rotating mounted perpendicular to the incident radiation. This method is typically used unknown or newly discovered materials, as the technique provides additional phase information for the sample, which results in precise calculations of the unit cell and bonding structure. This technique typically uses a Mo radiation source.

2.2.3 Small Area Electron Diffraction (SAED)

Electron diffraction is governed by the same (diffraction) principles as x-ray diffraction. However, the major difference is the length scale of the sample. The periodicity of a common x-ray sample is a few lattices (hundreds of picometers) while the periodicity of small area electron diffraction (SAED) sample is a few atoms (several pico meters).[45] These dimensions place constraints on the radiation source and required shorter wavelength. The incident beam is generated by electrons accelerated at voltages of 300 -1000 kV, which has a conical beam ~$\alpha > 10^{-3}$ rad.[46] Similar to the single crystal XRD method, irradiation of the sample produces only a few reflections. Therefore, to record an entire spectrum, the sample is required to be rotated. However, the electron microscope configuration does not allow free rotation. The sample can only experience tilting, which limits the reflections that can be captured.

2.2 Cyclic voltammetry

Cyclic voltammetry (CV) is a powerful electrochemical technique to understand electron transfer processes at the center of an electrochemical reaction. CV is an important and widely used electrochemical technique because of the versatility information that can be gained through its application. For example, a strength of this technique is obtaining valuable information from novel systems and systems with fairly complicated electrode reactions.[47]

The CV technique is used to acquire qualitative and quantitative information about the reaction. Qualitative information such as the presence of intermediates and the reversibility of possible electron transfer processes can be determined. Under particular conditions, Nernstian conditions, CV can be used to produce more quantitative information such as diffusion coefficients, formal reduction potentials, electron stoichiometry, and concentrations of unknown species. We use CV to determine a consistent number of reaction peaks and redox couples, which can be used as characteristic identifiers (fingerprint) to elucidate and propose a redox mechanism for nanostructured MoS_2 in a sodium ion system.

A general set-up requires a potentiostat and three electrodes, a working, counter, and reference electrode. The technique operates by applying a voltage across the working electrode, in which the chemical reaction is being investigated, and a counter electrode. The reference electrode is used as an internal voltage standard. To maintain a stable and constant potential, the potential of reference electrode is measured against the potential of the working electrode. The resultant potential produces an excitation signal which initiates the chemical reaction.[48] After reaching a predetermined voltage the potential is applied in opposite direction. As the potential changes, the corresponding changes of the current is monitored and recorded. The recorded data is plotted and generates a profile called a voltammogram. In general, the primary features of the voltammogram are peaks that are distributed between anodic (oxidation) region and cathodic reduction region. Over a particular applied voltage range, peaks occur as current begins to increase up to a maximum value indicating redox reaction on or around the working electrode's surface, which is followed by a sharp decrease. This maximum current is called the peak current. The peak current indicate as position where the concentration of the active species has been full oxidized or reduced. The anodic (oxidation) process the peak current is denoted by (i_{pA}) and the cathodic (reduction) process by (i_{pC}) .[49] The maximum current occurs specific voltage that is characteristic to that species. Therefore, the voltage potential of peak can be used as a diagnostic to identify the presence of a species on or around the working electrode. However, the peaks can become complex due the presence of intermediates and interactions between reaction kinetics and the scan rate of the CV experiment.

In the simplest electrochemical case, such as a reversible one electron transfer process, the voltammogram displays a redox couple two peaks of equal magnitude and area, divide between the anodic and cathodic regions (figure 2.2). If the reaction is not reversible a peak could appear in one region without a corresponding peak in the order region. Additionally a couple is determined to be quasi-reversible if corresponding peaks could be observed in reach region, but the area and height would not be proportional.

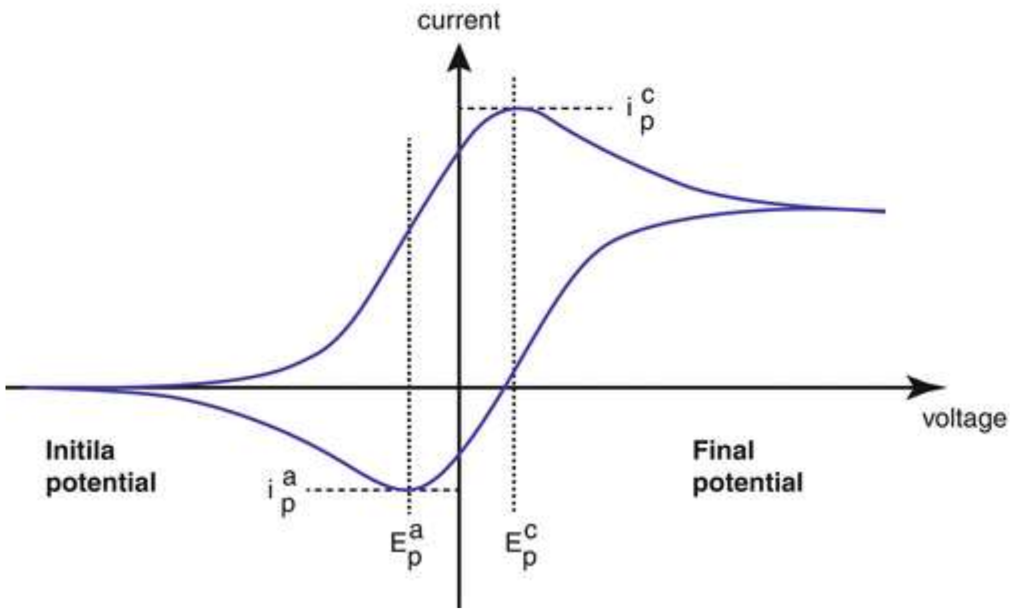

Figure 2.2. A typical cyclic voltammogram recorded for a solution contains only a single electrochemical reactant, Fe^{2+}/Fe^{3+}. The iron redox couple in aqueous solution presenting a reversible single electron transfer reaction. Taken from ref [48].

Reversibility is one of the most important pieces information that the CV technique can provide. Reversibility indicates the domain governing the working electrode, which can either be an ideal regime or a regime dominated by mass-transfer conditions. The regime limits the types of information can be extracted to identify and understand this system.

An ideal reversible process, Nernstian conditions or Nernstian equilibrium, is characterize by set of parameters:

1. The peak potential difference (separation) is equal to a proportionality constant, ΔE, $\Delta E = E_{pC} - E_{pA}$ = ~58 mV/ n at all scan rates at 25 C.

2. The ratio of peak current for a particular redox couple is 1; $i_{pAC} / i_{pC} = 1$.

3. The peak current function is independent of the scan rate, where the peak current function is $i_p/(mV/s)^{1/2}$.

Most experimental cases are not ideal; therefore, reaction being investigated will have mixed mass-transfer conditions.[49] Under these conditions, the peaks profiles or redox couples can be classified as a quasi-reversible or non-reversible process.[50] Quasi-reversible conditions meet some of the reversible criteria, but not all. Figure 2.3 display several representative quasi systems.

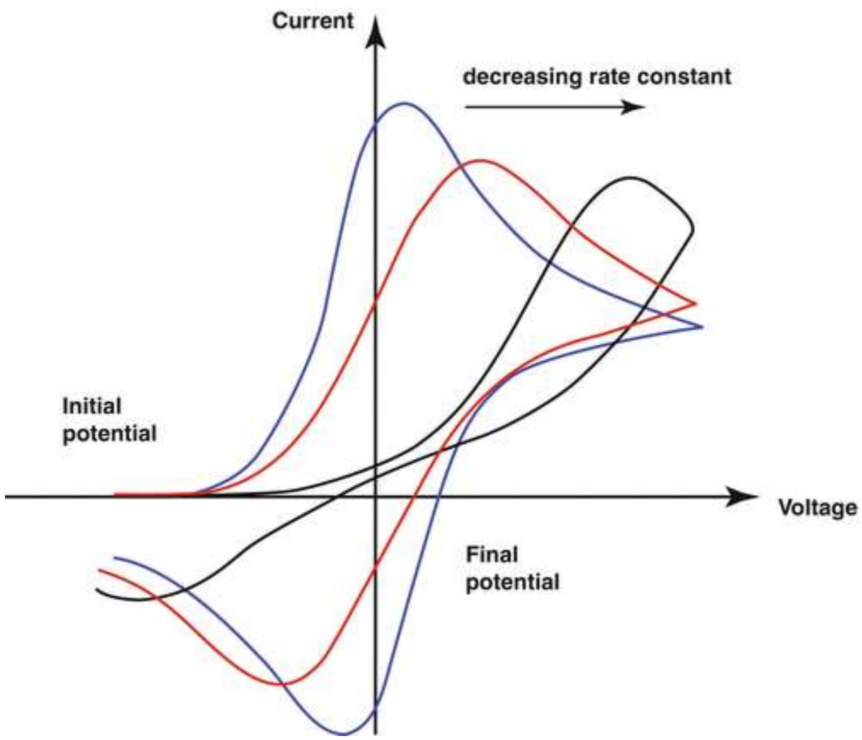

Figure 2.3. Cyclic voltammogram of a quasi-reversible system for evaluated at varying scan rates. Taken from ref [48]

2.3 **X-ray Photoelectron Spectroscopy**

The creation of disorder on small lengths scales can also result from the transformation of a compound into a new species. X-ray Photoelectron Spectroscopy (XPS) is compositional analysis technique used on samples with ultra-thin layers to probe the bonding environment. The technique has a penetration depth of 5nm, which means a sample, such as those from an electrode must remove unwanted layers (SEI) to find the desired surface area for analysis. The outside layers can be removed by ion milling to reach the surface of interest underneath. In the XPS technique, a collimated beam of Al kα is absorbed by the sample causing photoelectrons to be emitted from the sample. An electron energy analyzer is used to measure the energy of the emitted electrons to produce a survey spectra of a wide energy range. From the binding energy and intensity of a photoelectron peak, the elemental identity, chemical state, and quantity of a detected element can be determined. Further analysis can be conducted over a limited binding energy range. In this range, the types of bonds involving a particular atom can be observed. The ratio of the number of atomic bonds with specific binding energy.

2.4 **Polyaniline Polymerization**

Polyaniline (PANI) is one of the oldest and well-studied intrinsically conductive polymers. Aniline monomers are conjugation of in a chain using two primary methods anodic oxidative polymerization and oxidative polymerization. Anodic oxidative polymerization occurs within an electrochemical cell to induce the polymerization of aniline monomers. According to most experts, the first step in both the chemical and electrochemical oxidative polymerization of aniline, regardless of pH, is the formation of cation radicals.

Oxidative polymerization is the standard polymerization method and can be seen in equation 2.1. In this equation, aniline initially reacts with ammonium persulfate, the oxidant to produce the radical cation $[(C_6H_4NH)^{\bullet +}]$ (not shown), which in the propagation step, can react with other aniline molecules aligned mostly in a *para* position to produce the conjugated chain, polyaniline (PANI). While reactions with aniline molecules in the *meta* and *ortho* positions can occur they will react with a lower frequency. As the chain forms, it will precipitation out of aqueous solutions due to its increased insolubility. The precipitated product is shown in equation 2.1 is the emeraldine base ($[C_6H_4NH]_2[C_6H_4N]_2$) form. Figure 2.4 show a conventional depiction of the PANI polymer chain, where four repeat units are shown. This structure is consist of benzenoid amine and quinone imine repeat units, which are linked through nitrogen atoms.

$$C_6H_4NH + (NH_4)_2S_2O_8 \rightarrow [C_6H_4NH]_2[C_6H_4N]_2 + HCl + H_2SO_4 + (NH_4)_2SO_4 \quad \text{Equation (2.1)}$$

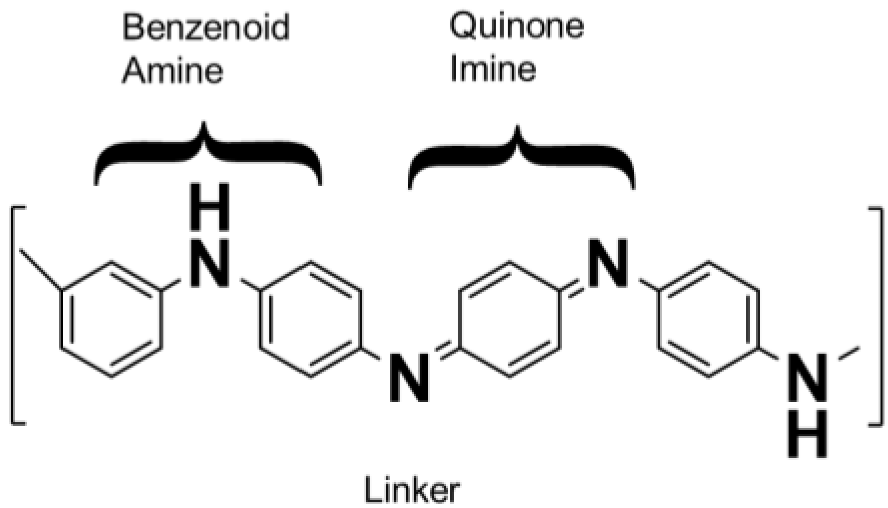

Figure 2.4. Chemical structure of undoped emeraldine (base) PANI chain.

PANI has three oxidation states, leucoemeraldine, emeraldine, and pernigraniline, which are the fully reduced, partial reduced, and full oxidized forms of PANI, respectively. The form that is most important to this research is the acid doped emeraldine (conductive) structure. The conductivity of the doped emeraldine structure varies from 10^{-2} to 100 $S.cm^{-1}$.[51] The acid dopant and polymerization conditions determine the magnitude of the compound's conductivity and the nanostructure formation. PANI nanostructured can take many difference forms e.g. fibers, particles, nanorods.

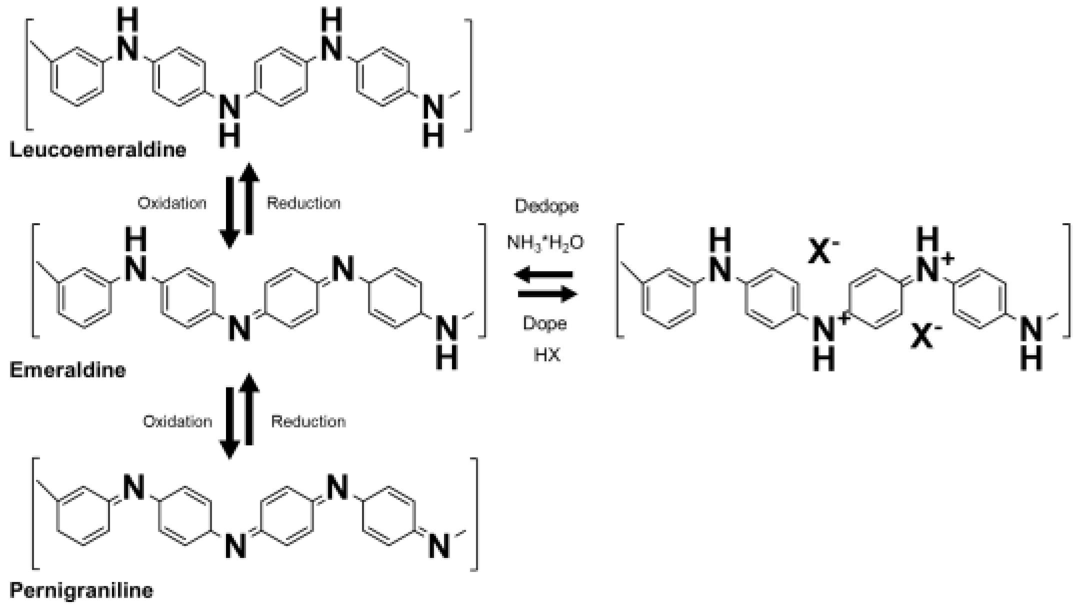

Figure 2.5. Chemical structures of the three oxidation states of PANI

A more extensive explanation of the polymerization process and parameter can be found in these references.[52-54] Our explanation of the synthesis of PANI will sole focus on oxidative polymerization under specific conditions similar to our studied system. The polymerization occurs without stirring in acidic media ≤ pH = 4 with elevated temperatures around 60 °C in order to coat the surface of a nanostructure. Li found that the absence of stirring PANI nanoparticles formed well-controlled sizes and shapes on the surface of silica nanomaterials and avoided induced aggregation.[55] Li concluded that stirring has a major influence in aggregation of polyaniline as it forms nanostructures.

Under increasing acidic conditions, the nature and the reactive species participating in the oxidation will change. The changes are due to high concentration of that radical anilinium cations and anilinium cations and low population of aniline molecules. This high population will slow down the polymerization resulting in an induction time, instead of aniline molecules being oxidized, oligomers will initiate the growth of PAIN chains during the polymerization.[54] The result is well defined and uniform nanostructures as no new nucleates will be produced during the polymerization growth can only occur at initiation centers.

Although MoS_2 will be formally define in the next chapter, this compound can be used as a support surface in which polyaniline can absorb to and polymerize on. As the polymerization proceeds, the increasing acid conditions can enhance the interaction between positive charged anilinium ions and negatively charged regions on the nanosize MoS_2 structures. Further, these conditions are optimal to be used to restack the MoS_2 nanostructures assembling them into a composite material with a layer-by-layer arrangement.

Chapter 3: Classical MoS_2 Insertion Studies

3.1 **Introduction**

To understand the debate surrounding the MoS_2 electrode, redox mechanism, and the potential byproducts and possible reactions, we will discuss the fundamental chemistry of MoS_2. Though MoS_2 is a prominent member of TMDs, its chemical behavior is atypical compared to most of the other compounds within this group. The complex nature of MoS_2 is a central theme to the discussion of this material. Various factors influence the intercalation reaction of MoS_2; one of the most important and impactful is the crystallinity of this compound. The amount of intercalation seems to increase with increasing disorder. The importance this parameter has been recognized over many years as the research into MoS_2 seems to become static and re-emerges in subsequent years.[29]

In this dissertation, I build upon the principal reactions of bulk MoS_2 to propose a new tool to investigate the surface interactions and expose a new role of single layer MoS_2 formed during the charge and discharge processes. As background for this research, this chapter presents the known intercalation and redox reactions of bulk MoS_2. Chapter 4 follows with my study of the complex chemistries and surface interactions of the nanostructured Na-MoS_2 electrode. The bulk MoS_2 electrode has two major electrochemical redox behaviors intercalation and, under specific conditions, sulfide or sulfur formation. We use this general term instead of conversion reactions because we believe more study is needed before proposing the MoS_2 and FeS_2 (pyrite) redox reactions, which is classically known as a conversion reaction, are the same.[56]

While the study of crystalline, bulk MoS_2 intercalation products have been around since the 1970s, studies of nanostructured MoS_2 electrodes are currently under investigation. Nanostructured electrodes with polycrystalline composition and high surface area are more akin to amorphous MoS_2, first intercalated and publicized by Whittingham.[29] Amorphous samples of TMDs have been reported to behave in manners distinctly different from single-crystal intercalation products, under specific reaction conditions. It is important to understand how intercalation reactions depend on MoS_2 crystallinity.

The current reemergence of MoS_2 research is due to a confluence of factors: parallel interest of MoS_2 as a transistor, which may give a processing advantage over other dichalcogenide systems, the discovery of its high tensile strength properties, unique optical properties, chemical inertness, cheap and abundance, similarity but distinct differences from graphene.[57-63] MoS_2 has shown the ability to accommodate large alkaline ions other than lithium, unlike graphene.

The re-emergence has spurn parallel research into sodium MoS_2. Sodium intercalations comes with unique challenges not seen in lithium intercalation.

Before addressing common assembly strategies and categorizing structures types, the lack of fundamental understanding of NSMoS for sodium ion battery must be discussed. Renewed interests in and accelerated growth of the MoS_2-Na electrode have been spurred by novel nanostructured MoS_2 (NSMoS) designs. Studies of novel NSMoS have mainly focused on performance values, such as increased capacity, coulombic efficiency, and cycling stability. However, these studies with their focus on strategy of designing novel experimental electrodes has not proposed clear design principles for electrode morphology, nor clarified poor understanding of fundamental chemical reaction mechanism. Similar nanostructured electrodes have shown vastly different performances values. Currently, the lack of consistent performance has been attributed to factors related to the electrode fabrication and half-cell construction, such as an increase of lattice edges and surface areas of MoS_2 components, complex effects of hybrid materials, compatibility issues and complex interactions of non-electrode components, and poor (solid electrolyte interphase) SEI control.[21-22, 27] By comparison, the NSB MoS_2 for lithium system shows better consistent in performance and trends, such as decreased capacity with increasing current rate, than nano-structured systems for sodium systems.

Additionally, the failure to gain insights from galvanic testing is compounded by the absence of well-established *in situ* analytical platforms, which can study NSMoS surface interactions and reaction mechanisms that can lead to either sulfur formation, polysulfide formation or both.[64 5, 27, 41]

Although the intercalation reactions happens on a smaller scale, the underlying redox chemistry of insertion (intercalation) has not changed. The process that is of increasing interest to researchers occurs when the limit of intercalation is exceeded. This redox process which follows the traditional intercalation process is defined as conversion. In this dissertation, I build upon the principle reactions of bulk MoS_2 to propose new tool to investigate the surface interactions and new role of single layer MoS_2 formed during the charge and discharge processes. To understand these conclusions, an understanding of the known intercalation and redox reactions of bulk MoS_2 is principle to study the complex chemistries and surface interactions of the nanostructured Na-MoS_2 electrode. These principle reactions were established through studies of intercalation of TMDs, parallels from the lithium-MoS_2 (Li-MoS_2) electrode, and the culmination of recent articles on Na-MoS_2 electrode. MoS_2 electrode has two major electrochemical redox behaviors intercalation and, under specific conditions, conversion reactions.

3.2 **Intercalation Reactions**

3.2.1 Introduction of Materials for Intercalation

Intercalation of bulk, crystalline solids has been well-established since the early 1970s. Intercalation reactions are classically defined as reactions in which ions or molecules are inserted into solid material without the destruction of the crystalline structure and extensive disruption of bonds.[65-66] The bonds within the crystalline solid determine the possibility for and the amount of intercalation. The bonds create an atomic framework composed of channels or vacancies that allows for the diffusion of molecules and ions, called guests, into the solid. The structural requirements of the framework are strong bonding and stable networks (lattices) with fixed atomic positions and vacancies. Strong bonding creates a lattice in which atomic positions are unaffected by insertion and vacancies allow for ion diffusion and storage. Solids that undergo intercalation fall in the following categories: chain structures, stacked 2D lattices (layered compounds), and 3D connected frameworks. A number of these solids are composed of transition metals and chalcogenides in different ratios. This discussion will not attempt to exhaustively explore the redox reactions of all the above structures. Henceforth, the discussion will focus on the intercalation of layered compounds.

Layered compounds are of great interest because they have a unique structure that allows chemicals to be stored inside or can be separated into atomically thin sheets. The potential for ions to be stored inside the materials allows the compounds to be used as a battery electrode. Additionally, these sheets are proposed to advance electronics in the future. In most cases, the structure can be described as composed of rigid layers separated at regular intervals.

The intercalation of layered compounds is especially unique compared to the intercalation of other solids because layered compounds can incorporate larger ions or molecules than other classes of intercalation solids (mentioned above). While there are a few types of layered materials that undergo intercalation reactions, all layered structures are composed of two types of bonds of varying strength. The weaker type of bonds can be weak electrostatic interactions or van der Waals forces. The stronger bonds are formed using covalent bonds or ionic bonds. The most well-known example of a layered compound is graphene, which has strong, covalent bonds in-plane and weak van der Waals bonds out-of-plane.

The second most notable compound, and the focus of chapter 3, are a class of materials known as the transition metal dichalcogenides (TMDs). TMDs are also known as graphene analogues. Similar to graphene, TMDs have van der Waals bonds out-of-plane. The van der Waals bonds allow for the displacement of the lattice planes in the z-direction. The expansion of TMD structures is hypothesized to allow almost unlimited expansion, perpendicular to the van der Waals bonds.[29] However, TMDs differ from graphite in the in-plane bonds. The in-plane bonds are ionic bonds. Together, the in-plane and out-of-plane bonding creates the layered or laminar structure, where lattices are stacked with alternating vacant channels where guests can reside. The advantage of using TMDs is that lattices provide larger space for the storage of larger ions and, in general, show less expansions when guests are inserted into their structure.[63]

3.2.2 Description and Classification of Intercalation Reactions

There are two classical types of intercalation reactions, topotatic and redox reactions. A third approach, exfoliation and restacking, uses molecular interactions to insert guests into the layered structures. In the classical reactions, temporary changes can occur in the crystalline solid. As guests enter the vacant channel, the lattices can deflect apart, due to repulsive interactions between the guests and lattice planes.

3.2.3 Topotatic Intercalation Reactions

The simplest form of intercalation reaction is called topotatic intercalation. In this case, although some layers are displaced as guests diffuse into the solid. TMDs meet the structural requirement for intercalation reactions. The requirement is satisfied because the atomic positions are locked into place in the x and y direction on the lattice plane. Additionally, the location of the vacancies do not change position, instead the vacant channels increase in length. As the guests are removed, the lattice planes return to their original z-position.

In topotatic intercalation, guests can also reversibly diffuse into and out of the host solid, such that when the guests are removed the final crystal structure remains identical to its original state. Although the initial and final states for topotatic reactions remain the same, slight and temporary changes in the structure can occur with insertion. For layered structures, often the interlayer spacing (in the z-direction or c-space) will expand or decrease as guest move in or out of the compound, respectively. This reaction is limited to low concentration of molecules and ions and is only observed for small guests, generally of neutral species. The chemical equation for topotatic intercalation is written in Schollhorn's notation below, which emphasizes the importance of vacancies. [64] The equation demonstrates that the maximum amount of guests is limited by the maximum number vacancies in the crystalline solid.

$$xG + [\ \_\ ]_x[H] \leftrightarrow G_x[H] \qquad \text{Equation (3.1)}$$

In equation 1, the variables G, [_], and H represent the guest species, vacant lattice sites, and host material (laminar structure), respectively. As the equation indicates, the reversible diffusion of the guest is governed by equilibrium. The insertion of guests into to the laminar structure creates the intercalation product, which is metastable. Therefore, the host can be restored to its original state by heating or aging. Classic examples of topotatic intercalation involve ammonia gas or ammonia liquid into host material at 1 atm and room temperature. In these cases, the insertion is entropically driven. [66] [18]

3.2.4 Redox Intercalation Reactions

Redox intercalation is a class of reactions in which electron transfer to or from the host is balanced by the flow of ions into or out of the structure. Cation intercalation, the focus of this dissertation, is driven by the induced negative charge placed on the laminar structure. In this case, electrons are added to the valance band of the crystalline solid. In general, the shape of the conduction band determines the ease of charge transfer and the stability of the intercalation product.

The reversible ion-electron transfer is described by equation 1.2, which is extended from equation 1.1 to include charges. Although the equation only illustrates cations, anions can be intercalated in a few positively charged layered materials with a removal of electrons from the structure. There are only a small number of positively charged matrices known.

$$xG^{+} + xe^{-} + [\ \_\ ]_x[H] \leftrightarrow G_x[H] \qquad \text{Equation (3.2)}$$

Similar to equation 1.1, equation 1.2 implies that the vacancies dictate the amount of guests that can be inserted. As previously mentioned, structural constraints are key to intercalation reactions. With the introduction of charge, the structure alone no longer governs the intercalation process and the reversibility of intercalation in most cases is lost. New constraints are imposed as the structure itself must screen the guest species in order to form a stable insertion product. Furthermore, with the addition of charge, the importance of charge transfer and amount of charge, in addition to size and concentration, limitations of the redox intercalation reaction are revealed.[64] Additionally, charge provides a driving force to achieve an intercalation product with higher concentrations of guests than the topotatic reactions above. These conditions can even be used to exceed the capacity of the structure, leading the host to decompose.

Redox intercalation can be split into two subgroups: topotatic redox interaction and redox intercalation. Specific hosts can undergo reversible redox (topotatic redox) over a range of molar amount $0< x \leq 1$, if intercalated with smaller guests with weak charges. For most crystalline TMDs, topotatic intercalation may be only possible with alkali metal insertion, such as lithium, if at all. Most intercalation reactions of TMDs fall within the category of non-reversible redox intercalation, even for lithium. When guests are removed, the final crystal structure will have changed from its original state. The changes can be slight such as increases in the length of the vacant channels or, more drastic, with changes in the position of the lattices or the coordination of the atoms.

The factors that have influence over intercalation are: Layered structures have optimal range for their formation. unit cell (coordination those with octahedral coordination have more iconicity or ionic behavior), (The unit cell is influence by the nature of host bonding). Like unit cell, the shape of band structure is correlated to the coordination. The electronic bands and density of states determine intercalation parameters the ease of intercalation and stability. The interaction between the bonding and the polarizability of the guest determine stability.

3.2.5 Intercalation by Exfoliation and Restacking

The third method of intercalation consists of a two-step process in which a crystalline solid is broken into small layers or sheets then reassembled, called exfoliation and restacking. This method is particularly useful for inserting large guests, tuning interlayer spacing, and generating unique structures and composites. In particular, various polymers, large anionic/cationic molecules, and organic molecules have been intercalated through the exfoliation and restacking technique such as PEO, polypyrrole, and polyaniline.[67-68]

3.3 **Intercalation Chemistry of Transition Metal Dichalcogenides (TMDs)**

3.3.1 Introduction

Now that we have addressed classes of general intercalation and redox intercalation above, we focus the discussion on TMD hosts. The contribution each factor plays and the limitations governing intercalation can vary between hosts. Most of these factors are related by the concept of charge distribution. We define charge distribution within the TMD host with the traditional definition of delocalization electron density. For instance, in a classic example, the intercalation of graphite can be modeled by a rigid lattice to screen the charged guest. The lattice is composed of rigid, planar sp^2 hybridized, π bonds. Although when an electron is added to the structure, the network of the π bonds allow a high level of electron mobility. Researchers proposed that the charge is held by π bonds so that the negative charge can be in close proximity to the positively charged guest in order to stabilize the intercalation product.

In contrast, TMD lattices are composed of flexible sigma bonds which have free rotation and can deflect to screen the charged guest. Considering bulk TMD crystals, however, when an electron is added to the structure the charge is proposed to be even more diffused (delocalized) than graphite. In the TMDs, electrons are more delocalized, behaving more as electron cloud instead of a point charge. As a result, the stability of the intercalation product is heavily dependent on the polarizability of the guest and the metal chalcogenide bonds. In summary, stability of TMDs are more complex than graphite because they are governed by a culmination of repulsive and attractive forces, which dictates the guest position.

Due to the complexity of the host, a more specific discussion of the intercalation of TMDs and MoS_2 is needed as the distinct differences in the TMD hosts lead to characteristic deviations in the parameters governing the intercalation process and the stability of the intercalation product. More than 40 combinations of transition metals and chalcogenides (S, Se, or Te,) exist.[66, 69] However, only about half of the combinations form layered compounds. The stability of the electronic structure is a major contributing factor to the formation of a stable layered structure, instead of the pyrite or marcassites structures. Initially, layered transition metal dichalogenides (TMDs) in their bulk form were investigated because they could transition to superconductors after intercalation.[29] Later, TMDs were investigated as intercalation electrodes in the 1.0 V- 2.5 V range, which offered low capacity of 100-200 mAh/g and short cycling lifetimes due to lattice constraints.[29]

3.3.2 Crystal Properties of TMDs: Crystal system, Coordination, Stacking

The choice of transition metal and chalcogenide affects the structural and electronic properties. Though the vacancies were mentioned as structural constraints for layered materials, the hole size has much less influence on the intercalation of TMDs. TiS_2 which possess the smallest spacing can incorporate more types ions and larger amounts of guess than other TMD compounds.[30] Instead, the bond polarity, coordination, and electronic structure of TMDs are the largest contributors to the intercalation behavior. We will begin with the crystal structure. Although d-block metals are relatively close in size, the choice of metal has a significant effect on the crystal properties (*i.e.* crystal system, coordination, stacking) and the electronic structure. The crystal structure and the band (electronic) structures are strongly linked.

The crystal structures and unit cells determine the number of vacancies and shape the band structures. TMD lattices contain two types of vacancies: octahedral and tetrahedral vacancies. The tetrahedral vacancies are comparatively much smaller than the octahedral. The exact, numerical size of the vacancies are achieved by combining the metal and chalcogenide atoms with the largest diameters. The total number of octahedral and tetrahedral vacancies is given by a ratio. The octahedral vacancies are equal to amount of metals atoms, whereas, the number of tetrahedral vacancies are equal to twice the number of metal atoms present in the unit cell.[70] Unlike the number of vacancies, which is static, the positions of the vacancies depend on the crystal's symmetry and coordination.

TMDs are very versatile in their atomic organization. TMDs can vary in crystal structure, coordination, and stacking. They have three types of crystal structures, trigonal, hexagonal, and rhombohedral, and two types of coordination, octahedral and trigonal prismatic coordination. The last form of variability, stacking, comes from amount of unique layers in the unit cell or atomic geometry in the z-dimension of the unit cell, figure 1.

In general, TMDs with trigonal and hexagonal crystal structures have octahedral and trigonal prismatic coordination, respectively. The octahedral coordination is correlated with TMDs with high metal character and trigonal prismatic coordination is preferred for TMDs with low metal character. The character of the transition metal increases from right to left across a period and down a group.

Therefore, metals in group IV and transition metals in the 1st row, such as Ti, V, Cr, tend to have octahedral coordination. TMDs with metals in groups V-VI are often found to have trigonal coordination. Additionally, there are crystals such as $TaSe_2$ with mixed coordination.[66]

Even more complex, some compounds, such as MoS_2, can have more than one type of crystal structure. When a compound has multiple possible crystal structures, the compound is called a polymorph. Additionally, in a crystal structure with a specific coordination, multiple stacking arrangements can exist, which are called polytypes. To keep track of the complex organization a notation system was created, the Ramsdell notation.

Ramsdell notation emphasizes crystal structure and coordination, which are closely tied to the intercalation stability and the intercalation parameters. Figure 1 shows a few structures of reported TMDs with the Ramsdell notation at the bottom of each structure type. The unit cell is represented by the rectangle with dotted lines. The van der Waals gap follows each unit cell. The letters to the left of each unit cell compose the stacking sequence, which represents inequivalent positions for each close-packed stacking, where the lower case letters denoted the metal positions and the capital letters represent the chalcogenide positions.

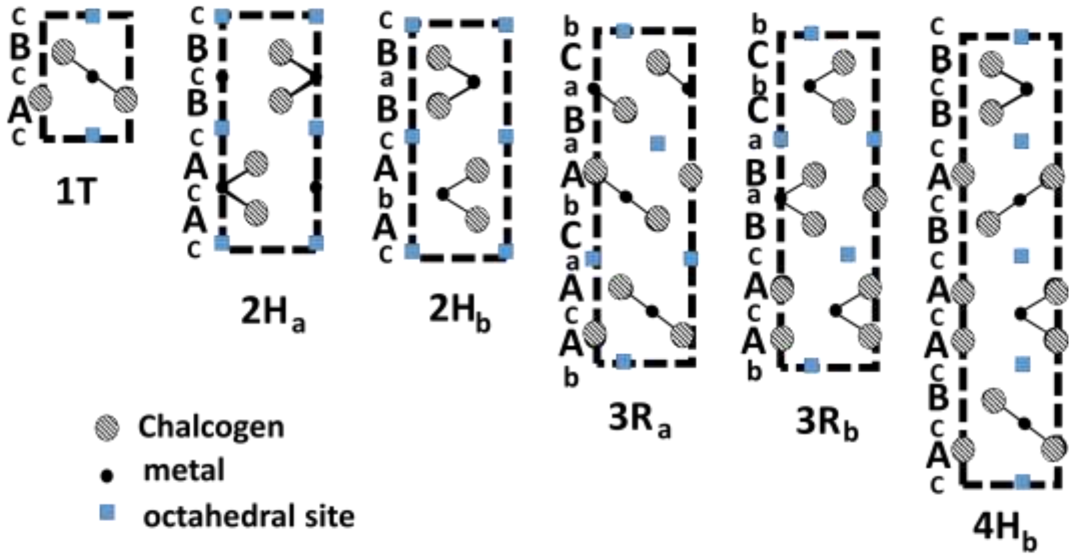

Figure 3.1. Diagram of the unit cell of known structures of transitional metal dichalcogenide in the 1120 projection.

The Ramsdell notation for the simplest structure is 1T. The 1 stands for number of slabs (atomic repeat units) and the T is the first letter of the crystal system, trigonal. In this case, the unit cell is equal to the slab. However, this is not always the case. Consider the $2H_b$ notation, which denotes the most prevalent form of MoS_2 found in nature, and $2H_a$. $2H_a$ and $2H_b$ are polytypes, which differ in the position of atoms within the unit cell, but have the same number of slabs (atomic repeat units) within the unit cell. Again, the 2 stands for number of unique slabs and the H is first letter of the crystal system, hexagonal. For the $2H_b$ structure, both slabs consist of one metal and two chalcognides. However, the slabs are distinct as the position of the metal and chalcogenides are in different locations. In contrast, $2H_a$ has two slabs consisting of one metal and two chalcognides, where half of each metal atom sits inside of the unit cell.

3.3.3 Electronic Bands and Density of States of TMDs

The relationship and interplay between the crystal structure and the band structure govern the properties of TMD compounds. More importantly and more specifically, the d-orbital filling, which is a component of the band structure, can be used to understand both the stability of the host and the stability of the intercalation product as guests are inserted into the host. The band structure contributes to the intercalation process and determines the parameters of the intercalation process. Therefore, it is important to understand how the band structure is affected by a compound's atomic coordination, atomic composition, and orbital filling.

In a brief introduction of band theory, electrons contained a solid are divided between two bands called the conduction and the valence band. For nonmetals, the bands are separated by a gap, region where no electrons can be held or no electron orbitals exist. The top band is the conduction band. It is the highest energy band where electrons can be mobile. The conduction band can be empty or partial filled. Below the gap is the valence bands, which is generally completely occupied by electrons. For semiconductors with small gaps, electrons from the top of the valence band can be promoted without a large energy penalty. Additionally, the gap may not be symmetric, but can have an irregular shape, where minimum points of the conduction band and maximum points of the valence band can be in close proximity, which will facilitate the transition of electrons. This situation is called overlap.

Figure 3.2 illustrates the electronic bands and density of states with differences in transition metal composition. In band theory, the structures are classified as broadband semi-conductors (semi-metal for Ti compounds), metals, and semi-conductors for figures 2a, 2b, 2c, respectively. TiS_2 (element 22) has a band structure similar to figure 3.2a. However, it is classified as a semimetal not a semiconductor because of a small overlap between conduction band and valence band.

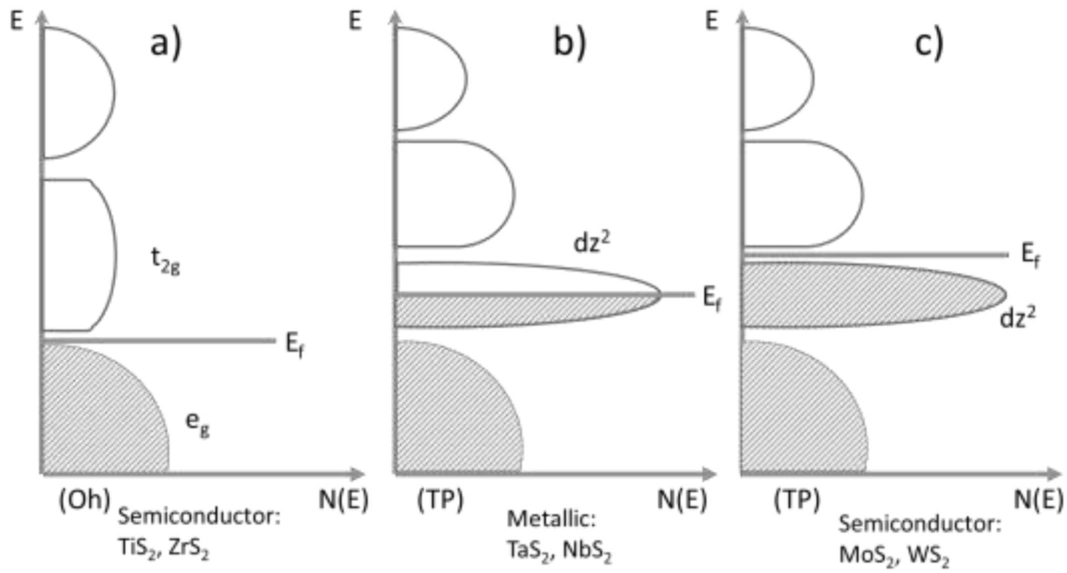

Figure 3.2 Density of electronic states for the electronic band

For TMDs, the cationic d-orbitals are the major contributors to the conduction band and the anionic (chalcogen) and the antibonding cationic (transition metal) sp hybridized orbitals are contributors to the valence.[64] Since the d-orbitals are involved in the conduction band, there are band structure changes corresponding to metal substitution across a period from left to right. As mentioned above elements numbers 22-24 (1^{st} row transition metals) have octahedral coordination when paired with sulfur. Starting from TiS_2 (element 22), which has a d^0 cation configuration, and moving to the right, the broadband structure similar to figure 3.2a begins to fill in electrons in the t_{2g} conduction band for d^1 and d^2 configurations, for VS_2 and CrS_2

respectively. The filling trend for the first row ends before forming the d^3 configuration.

Although adding a third electron to form a d^3 configuration is theoretically predicted, MnS_2 does not exist as a layered structure (with octahedral coordination). Ligand theory predicts three degenerate orbitals (dxy, dxz, dyz), which have the potential to accommodate a third electron to the conduction band. Instead, MnS_2 forms a pyrite or marcasites structure. The absence of a layered structure for MnS_2 provides proof that structure may have a maximum limit on charge. If the charge limit is exceeded then the crystal structure of a host can be destabilized.[64] The destabilization of the octahedrally coordinated layered structure can be explained by the formation of anionic dichalcogenide pairs $(S_2)^{2-}$, which can compete to accept charge. Brec *et al.* defined this interaction as the sp-d redox competition.[64] The competition becomes more pronounced with increased overlap between d-levels of the conduction and sp anionic level of the valence band. Increased overlap and higher probabilities of forming anionic pairs occurs when pairing weakly polarizable metals with highly polarizable dichalcogenide (*i.e.* $TiTe_2$, VTe_2). The overlap occurs because electrons occupy higher energy orbitals proceeding down a group.

Generally, charge is accepted by the conduction band associated with the d-orbitals of the cation, as the d-orbitals have the lowest occupied energy levels. When a large overlap occurs, the d-levels enter the sp anionic valence band. In this situation, any unfilled d-orbitals will fill up at the expense of the valence band. This will cause holes to appear in the top of valence band. When there is a small number of holes, the semiconductor behavior is maintained. However, in the event of a high concentration of holes, the holes may coalesce into anionic pairs forming $(X\text{-}X)^{2-}$ from X- species.[64] This phenomenon explains the absence of a layered structure for MnS_2 and the formation of $(S_2)^{x-}$ pairs. This reaction maybe critical in understanding decomposition of the MoS_2 crystal structure and the formation of polysulfide species on the MoS_2 nanostructured electrode.

The d^3 configuration has been reached with a few TMD compounds, and has not been exceeded. The intercalation product $LiMoS_2$ has a d3 configuration explained by d-sp redox competition.

The configuration of natural occurring TMDs illustrate the predicted stability and offer potential limits to TMD intercalation products. ZrS_2 like TiS_2 has a d^0 cation configuration. Moving down the 4B group increase the d-orbital energies opening a large band and forming a broad brand semiconductor. Moving across the period to NbS_2, a d^1 cation configuration, results in a narrow half-filled conduction band characteristic of a poor metal.

Band changes can also be correlated with the crystal properties changes. The switch from broad bands to narrow bands coincides with a switch from octahedral coordination to trigonal prismatic coordination. The switching of band structure occurs as the polarization from a more ionic nature to an increasingly covalent nature.

The switch in coordination allows the stabilization of the band structure. If during the transition from ZrS_2 to NbS_2, the octahedral coordination is maintained an octahedral coordination, then an electron would be placed in one of the three degenerate positions resulting in a high energy state. According to ligand field theory, the d-orbital splitting for trigonal prismatic coordination lowers the degeneracy and leads to an electron configuration where the electron can sit at a lower energy state. Changes in the atomic coordination are a central theme when discussing intercalation especially for the MoS_2 intercalation product.

To the right in the period, MoS_2 is formed with a d^2 cation configuration, which has a narrow band structure. The addition of another electron creates a diamagnetic semiconductor with a filled conduction band. The filled band structure is extremely stable and together with the covalent-like Mo-S bonds accounts for the characteristic chemical inertness and intercalation resistance of bulk MoS_2. Moving to TcS_2 create a d^3 configuration is predicted to change the trigonal prismatic to octahedral coordination. However, there is a lack of information on the layered structure of TcS_2. Currently it is known that one form of TcS_2 is not layered, but instead it has P1 space group. Significantly, the intercalation of MoS_2 ($2H_b$) creates a d^3 configuration with octahedral coordination, which is structurally isoelectronic to the predicted structure of TcS_2.

3.3.4 Bond Polarizability and Guest Interactions

Although band structure changes across a period were discussed, the largest changes in the electronic band structure are seen when substituting metal and/or chalcogenide for the atom below it. The effect of the changes down the periodic table increase or decrease the overlap and the iconicity of the bonds for the chalcogenide group and metal cation groups, respectively. While filling across a period minimizes the change in the ionic nature of the bonds, moving down a group changes both the sp-overlap and nature of the bonding (ionicity) by similar magnitudes. Changing the chalcogenide composition down the group leads to increased covalency and an increased overlap as the height of the valence (sp-bonding) is extended into the conduction band. This means that the d-sp competition and formation of holes occurs at a lower d^x configuration and fewer guests. The substitution of metal with the preceding elements increases the metallic nature of the TMD, but decreases the overlap. Restated, for clarity, going down a metal group increases the ionic nature of bonding while decreasing d-sp competition. In contrast, going down chalcogenide group decreases the ionic nature of bonding while increasing d-sp competition. In both cases, the increased in polarizability of the bond (ionicity) imposes major constraints on the intercalation product. The polarizability limits continuous intercalation and lowers the stability of the intercalation product. For instance, intercalation with ditelluride (XTe_2) compounds can lead to the reduction of the host and the formation of alkali telluride species.[66]

While the degree of the ionic character, also called bond ionicity, in a TMD bond is tied to coordination and band structure, its individual contribution to intercalation is hard to decouple from the band structure. There is no generalizable trend between bond ionicity and intercalation. However, a trend emerges when monitoring the guest interactions and the polarizability of the bond.

The nature of the guest interactions can be divided into two categories: polarizability and concentration of the guests. The increasing polarizability of both the host and guest leads to decreased stability. The decrease in stability arises from the requirement of the host to screen charged guests and manage the coulombic forces and distribute of the charges within the host. The polarization of ionic guests affects host due to their proximity to the transition metals within the lattice. Traditionally, graphite intercalation literature describes ions in terms of size; however, we discuss the ions in terms of polarizability because the TMD systems have a more diffused charge distribution than the graphite. Furthermore, Rouxel *et al.* demonstrated the difference in polarizability by comparing the intercalation of similarly sized Na^+ and Ca^{+2} ions into TiS_2.[66] In the study, the maximum molar Na^+ content was ≤ 0.81 while the maximum molar content of Ca^{+2} was ≤ 0.5.

During the redox process, cations enter the structure and reside in vacancies that have close proximity to the transition metals. Cations are inserted to maintain charge balance and aid in neutralizing the excess charge of the transferred electrons. The reaction starts at the lattice edges and moves through the crystal until the final intercalation product is obtained. In the same way, the counter ions simultaneously move through the crystal as the reaction proceeds. The quantity of ions entering the host is not always stoichiometric. The maximum allowed guest could be 1 molar or less. The filling of the van der Waals gap is not always continuous over the entirety of this range; instead, only discrete intervals are allowed to fill. The proximity of the counter ion to the metal causes a strong polarization, which creates a positive potential around the transition metal site and induces a negative charge fault around the ligands.[64] The positive potential causes the electrons to be pulled to this site instead of to the ligands, which in effect creates a large polarizability within the entire hosts. The change in the polarity of host is similar to the pattern seen when substituting a more polarizable metal, as mentioned above. The changes in the bonding leads to increased instability and a possible reduction of the host, forming sulfides.

As mentioned above, the coordination and stability of the intercalation product, especially involving guest ions, are conceptually analogous to the pattern that was seen with naturally occurring TMD hosts. This concept can be clearly seen with sodium insertion into a TiS_2 host; lithium insertion does relatively little to polarize most TMD hosts. For instance, when sodium insertion reaches about 0.4 molar ($Na_{0.4}TiS_2$), a change occurs in the stacking so that the ions can be stored in trigonal prismatic sites and the corresponding (transferred) electrons are stored in orbitals with d^2z orbital contribution.[71] The coordination and the associated band structure changes are similar to that of the transition from ZrS_2 to NbS_2. Another transition that occurs within one compound and follows this pattern is the transition from MoS_2 to $LiMoS_2$, which changes from 2H stacking with a trigonal prismatic coordination and d^2 configuration to 1T crystal stacking with an octahedral coordination and a d^3 configuration. The $LiMoS_2$ is structurally similar to and isoelectronic with the binary sulfides of the Group VIIB like ReS_2.[72] These shifts in crystal and electronic structure constitute phase changes, a topic that will be elaborated on in the next section.

As shown above, the cationic guests act both as a stabilizing force, counter ion, which neutralizes excess charge, and also as a destabilizing force, perturbator, which destabilizes the bonding and strains arrangement of the original crystal structure. Therefore, it is important for all coulombic and charged interactions (*i.e.* repulsion between negatively charged layers, repulsion between cationic guests, attraction between layers, and attraction between guest and layers) to find equilibrium within the host structure. These interactions reach equilibrium through spatial arrangement (staging) within the crystal and morphology changes (phase changes) of the crystal. The largest effect for staging is at low guest concentrations and for phase changes is at higher guest concentrations. While some changes in the crystal structure can be determined through x-ray diffraction and electrochemical cells, these techniques lack the ability to detect all interactions, especially phase transitions.

3.3.5 Staging

Staging is a process in which ions are only allowed to enter the crystal structure at specific intervals, forming an intercalation product with alternating sequences and empty van der Waals gaps. The ions enter the lattice at specific laminar intervals then travel through the tetrahedral vacancies until the minimum energy of competing coulombic interactions is achieved.[66] The optimal balance of these interactions occurs when ions are in the octahedral vacancies for TMDs with octahedral coordination or in trigonal prismatic vacancies for TMDs with trigonal prismatic coordination. As the ion concentration is increased, new optimal positions are needed.

In staging, the frequency of the sequences is denoted by the stage number, where the lower numbers indicate increased amounts of guests. For example, Stage II indicates that guests are present at every 2nd layer. This phenomenon is observed at low guest concentrations. The occurrence of staging suggests that the energy of the system is lower when guests are localized at particular intervals rather than the homogenous filled throughout the layered structure.[65] For specific hosts, additional guests can be inserted into the host, which transitions the structure to Stage I, where guests can be found in every layer. This staging process was classically observed by XRD and NMR using isotopic guest ions.

3.3.6 Phase Changes

General molar content studies involve insertion and detection guest species starting from $x \approx 0.1$ and completing at $x \approx 1.0$.[73] As mentioned above depending on the interaction between the host and guest, the insertion within this interval can have a lowered maximum content, can be discontinuous, and/or can change the structure of the host. A phase change or phase transition is any structural reorganization of the lattice. The structural changes can be induced by the guest content and/or by the strain of the battery cycling process. Structural changes and the amount of guests can result in changes to the properties of the material, particularly the (electronic) band structure. Asai reported changes in the diffusion coefficient with changes in composition.[74]

Phase changes can become even more complex during the process of battery cycling. Repeated cycles can generate multiple distinct phases within the nanostructured electrode simultaneously, called a multiphase system, or lead to the inhomogeneity and complete disorganization of a crystal structure.[30, 64] The latter situation was first shown in a study of titanium disulfide and can be used to understand the lack or removal of characteristic lattice peaks in XRD spectra for MoS_2 and other TMDs. We will refer to the loss of stacking while maintaining crystal structure as incoherent stacking or lack of coherent stacking. We define the formation of non-uniform species as amorphous.

At the extremes, repeated lattice movements, as a result of continuous insertion and removal of guests (cycling), can lead to the complete destruction of the crystal stacking which can occur for systems such as TiS_2.[30, 64] Additionally, in the case of MoS_2, a phase change also encompasses changes in the coordination of the atoms within a lattice as well as the shifting of the lattices.

The site changes from octahedral to trigonal prismatic or from trigonal prismatic to octahedral.[75] This change originates from a buildup of negative charge, which increases the repulsive interactions between layers.[72] A more fundamental explanation of the charge interaction will be discussed in section 3.3.5. A shift in the coordination of the hole requires a shift in the lattice plane. Continuous shifts in the lattice plane such as during charging and discharging of a secondary cell can lead to the complete disorganization of a crystal structure.[30, 64] This instance was first shown in a study of titanium disulfide and can be used to understand the lack or removal of characteristic lattice peaks in XRD spectra for MoS_2 and other TMDs.

Returning to the classic examples discussed above of the TiS_2 and MoS_2 host, these examples were predicted to have only two phases. However, further investigation indicated the presences of more phases.

Hibma *et al.* reported that Na_xTiS_2 exhibited a non-stoichiometric behavior, which means that it deviates from the two-phase system described by the Gibbs phase rule.[73] This behavior was also found by incremental capacity analysis for the $LiMoS_2$ system, which had been shown by x-ray diffraction and electrochemical cell data to be a continuous phase.[29, 73] Therefore, this non-stoichiometric reaction may be present in many of the TMD systems during intercalation. The incremental capacity technique became a useful tool to detect these non-linear phase transitions.

Not all phase transitions are linear transformations from one phase to another. Instead, some conditions can induce multiple phases before returning to a single homogeneous phase material. The presence of multi-phases complicates some analytical measurements, as there is an implicit assumption that the host transitions through a single phase. One example is in the case of cyclic voltammetry measurements and galvanostatic plots, which are governed by Fick's law and require single-phase transitions.[29] Particularly in the battery, more phases can simultaneously exist due to strain. Strain conditions have been identified within the battery and specific phases have been resolved after electrochemical intercalation using special techniques and corroborated independently by complimentary analysis.[76]

The incremental capacity technique shows that TMD electrode materials exhibit a complex intermediate behavior.[30, 77] Although we will not discuss the derivation of the technique, we will discuss the interpretation of the data to reveal the phase information. The technique analyzes the voltage curve shape, slopes and plateaus, and attributes the capacity fading to specific electrochemical processes instead of a direct voltage analysis technique, which attribute voltage drop (an absolute value) to the sum of all processes occurring at a particular potential.

A simple way of understanding the complex behavior and need for an analysis technique that utilizes the slope is by first thinking of the phase transitions as classical conformation changes that describe molecules. Molecules are dynamic and can assume various positions by twisting and bending around single bonds that have free rotation. In this thought experiment various lattice sites can twist, which causes similar concerted movement from neighboring sites that share sulfur atoms. The situation becomes more complex when considering that the composition of the host lattice is changing with the additions of guest ions. This perspective emphasizes that multiple variables are changing at once. At a minimum two variables (*i.e* the structure and the composition) will be changing, which means mathematically the behavior of phase transitions can be represented by a surface and that multiple solution phases are possible.

The incremental capacity analysis technique was devised to evaluate the total number of observable phases and the approximate guest content where each phase might appear during the battery process or an intercalation process. This technique uses the changes in the inverse derivative voltage (*i.e.* incremental capacity) and the cell voltage, to determine a new phase as a function of guest composition. The technique allows for comparisons of plot features such as breaks in the slope of the curve, continuous curves, and flat incremental capacity to indicate multiphase, single phase, and amorphous behavior, respectively. For systems without atomic re-organization, such as TiS_2, the system was found to have a single phase when intercalating lithium, but three distinct phases when intercalating sodium ions. MoS_2, which goes through atomic reorganization, showed four distinct phases when intercalated up to 1 molar lithium content.

At times, the analysis of features can become difficult, especially for systems with limited information and/or exceptions to Gibb's phase rule (*e.g.* compounds with special symmetries and systems experiencing chemical reactions). For specific TMDs phases, little is known about the distribution of cations within the host. TMD hosts Particularly with, as ICA does not determine the type of phase due to the exemption from the Gibb's phase rule removal of Fick's law. Nevertheless, the knowledge of the beginning of a phase coupled with inspection by complimentary techniques can resolve the possible crystal structure of a specific phase. The resolved structure of the intercalation product then provides insights to calculate or propose an electronic structure, as a TMD crystal structure is precisely linked with a specific electronic structure.

Researchers have reported correlations between charge transfer from chalcogenide p-orbitals into d-orbitals and coordination changes and/or drastic changes in lattice parameter (*e.g.* c/a ratios, bond distances). [71, 77] The electron transfer is most critical for cases involving binary tellurides as the tellurides contribute p-orbitals of much higher energy levels than that of selenides or sulfides. Therefore, the overlap occurs at earlier d^x configurations and transitional metal combinations. Band structure analysis, Mulliken population analysis, for metallic systems were confirmed for systems such as $TiSe_2$ and $TiTe_2$. The amount of charge transfer from the chalcogenides to the transition metal were approximated to be 0.02 electrons/$Å^3$ and 0.38 electrons/$Å^3$ for Se and Te, respectively.[64] Calculation have shown an electron transfer of 0.25 electrons/$Å^3$ for VTe_2, which has d^2 configuration and zigzag chain formation.[64]

Though band structure analysis of TMDs have focused on binary Te compounds with low d^0 – d^2 configurations, which has the largest probabilities for electron transfer, metallic $LiMoS_2$ should have considerable transfer values since electrochemically exfoliated was found to have a zigzag chains of WTe_2 crystal type.[76] As the guest polarizes neighboring bonds in the lattice, transferred electrons can be added to the d-band. The additions to d band can lower the bands or "pull states out of the band" causing moderate changes such as changes within the crystal structure the semi-conductor material becomes metallic and drastic changes in the crystal.[78] Drastic changes can be associated with large changes in the c/a ratio and bond distances resulting in abrupt changes in the electronic band and the possible destabilization of the host lattice. Recent literature has shown significant delamination of a MoS_2 electrode during sodium insertion within an electrochemical cell.[25, 31] These observations provide further evidence to a published intercalation study that found no intercalation product after reactions of MoS_2 with a sodium electride solution.[79]

3.4. **Development of MoS_2 Insertion Chemistry and Mechanism**

3.4.1 Introduction

Recently, focus has shifted from the TiS_2 to molybdenum disulfide (MoS_2) as the model TMD. MoS_2 has garnered large interest because its unique behavior and wide interests in electronics. While traditionally, MoS_2 was consider only as an insertion cathode for lithium ion batteries. Molybdenum disulfide (MoS_2) is now being explored low-cost candidate for both LIBs and SIBs and both as a cathode and anode. The versatility of the MoS_2 electrode is derived from its good mechanical stability (an effective Young's modulus of 270 GPa) due to a robust lattice structure and its cell discharge-charge voltage in the 0-2.5 V range. MoS_2 possesses a naturally occurring hexagonally packed structure with a molybdenum trigonal prismatic coordination and van der Waals interlayer spacing of 0.615 nm. The lattice space exceeds the spacing of graphene (0.34 nm).

MoS_2 possesses both a higher theoretical capacity (372-670 mAh/g) and lower volume increase during ion insertion than a graphite anode. MoS_2 also has distinct advantages over graphene such as a direct band gap (1.8eV for monolayer MoS_2 compared to 0 for graphene) and a larger interlayer spacing (0.615nm for 2H-MoS_2 compared to 0.35nm for graphite), which are useful for transistors and batteries, respectively.

The development of MoS_2 as a sodium electrode has followed similar intercalation studies of other TMDs materials. Studies of x-ray diffraction patterns taken for various amounts of lithium content was the first approach to understanding the mechanisms the reactions of alkali metals with crystalline materials TMDs.

This chapter will discussion of findings of solid-state intercalation and MoS_2 electrodes studies in the context of similar systems in order to see distinct characteristics and gain fundamental understanding of the reaction mechanism and chemistries of the MoS_2-Na system.

3.5 Chemistry and Structures of MoS_2

3.5.1 Chemical Properties and Crystal Structure Link

In order to understand MoS_2 nanostructured electrochemical behavior, it is important to understand naturally occuringMoS_2. Crystalline MoS_2 is found in a mineral called molybdenite. The inertness and durability of the MoS_2 lattice originates from the strong Mo-S ionic bonds in-plane and redox resistant band (diamagnetic) structure. The electronic and crystal structure are strongly linked, changes in the band structure lead to changes in crystal structure. Physical changes to crystal such as decrease in thickness lead to slight increase in band gap until a monolayer is formed. The largest change occurring when a single layer is formed. The transition from bulk to a monolayer transforms the indirect band gap of MoS_2 into a direct band gap. Even the wrinkling or folding of the monolayer has also been shown to shift the band structure.[80]

Molybdenite is chemically inert. Unlike other TMDs, crystalline MoS_2 can only be directly intercalated by lithium metal and ammonia.[72] MoS_2 is able to withstand the reduction by solutions of hydrochloric acid, nitric acid, or sulfuric acid. No incidence of defects were reported on the surface after the etching time, indicative of high stability. MoS_2 has found uses as a high temperature solid-state lubricant and even as a physical absorption barrier for sulfur battery, which maintained its structure for the duration of the testing.[29]

3.5.2 MoS_2 Crystal Structures

MoS_2 (molybdenite) is a hexagonal layered material with ionic bonds in-plane and van der Waals interactions out-of-plane. Within a single layer, 6 sulfide ions surround a Mo (IV) ion. The sulfides, which form the vertices are shared with three neighboring Mo (IV) ions. The sulfides enclose the Mo ion on either side forming S-Mo-S layer that are stacked. The MoS_2 lattice is held together by sulfur-sulfur van der Waals interactions, forming the van der Waals gap (lamella) where ions of molecules can be stored. The major structures are illustrate in figure 1-6 and the generalized stacking sequences are also listed. MoS_2 has three major polymorphs: having three major crystal structures given the notations, 2H and 3R, have the trigonal prismatic coordination, and 1T, has octahedral coordination.[58, 63, 81] These 3 polymers are shown in figure 3.2 In addition the metastable polymorphs include 3R (rhombohedral) and 1T (trigonal) forms.

The 1T structure is synthetic and highly important to the battery and solid-state materials. The greatest change in the crystal and band structure of 2H MoS_2 occurs when ions are inserted into the van der Waals gap irreversibly forming the 1T phase. The irreversibility of transition from 2H to 1T can be understood with a carefully re-examination of 2H and its stacking. A closer look at the 2H in figure 3.2, reveal the second layer in 2H structure is slightly staggered while the layers of the 1T structure are directly aligned. A more specific stacking for 2H is given as AbA/BaB in the c direction, in which the capitalized letter indicate anions and lower case the cations. The coordinates for the ions are S-positions in ($\pm 1/3$ $\pm 2/3$ $\pm 3/4-z$) (Site A) and ($\pm 2/3$ $\pm 1/3$ $\pm 5/4-z$) (Site B) and Mo in ($\pm 1/3$ $\pm 2/3$ $\pm 1/4$) (Site b) and ($2/3$ $1/3$ z''')

(Site a) with z=0.121.[29, 64, 66, 72] Therefore, the phase transformation is not only constitutes a coordinate change by a change in the crystal packing, but layer realignment, as well. While shifts in coordination can occur with removal of ions (oxidation), the realignment of layers and repositioning of each atom is difficult to achieve.

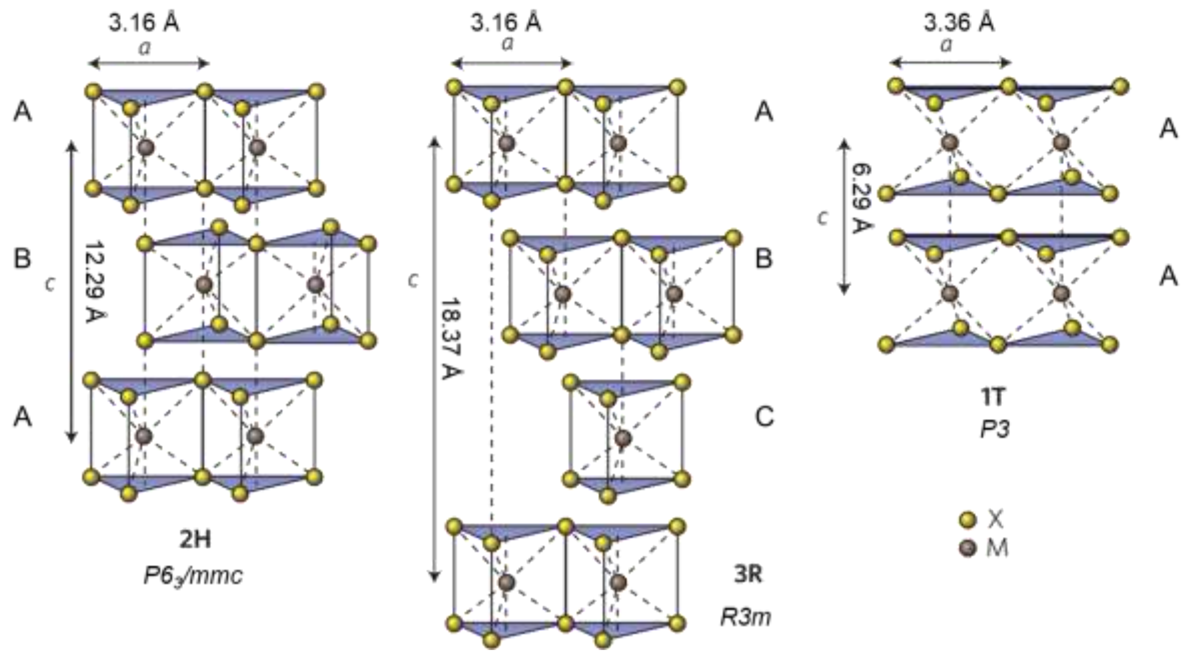

Figure 3.2. A diagram distinguishing the three polytypes of MoS_2 crystal structure. The first two lattices have trigonal prismatic geometry with the last structure shows octahedral coordination. In this constructions the length a = b. Modified from [58]

3.5.3 Phase Transitions

In 1990,Whittingham first demonstrated that lithium insertion into MoS_2 had a complex phase behavior consisting of approximately four phases, at room temperature.[29] Figure 3.3 show an incremental capacity analysis curve displaying four different slopes indicating that four phase occur up to 1 molar lithium content. The octahedral transformation is said to occur over the entire detection range x ≈ 0.1 to x

≈ 1.0. Currently, three phases are largely agreed upon with the first phase and second phase being the original 2H phase and a supercell structure. Li_xMoS_2 supercells were first verified by insertion using n-butyl-lithium over the 2.3 V - 1.7 V range and XRD analysis at the appearance of the first slope change 0.25, showing the presence of superimposed diffraction spots corresponding to ion insertion. One of the remaining phase is assigned to the 1T phase though the actual structure type remains under debate.[76]

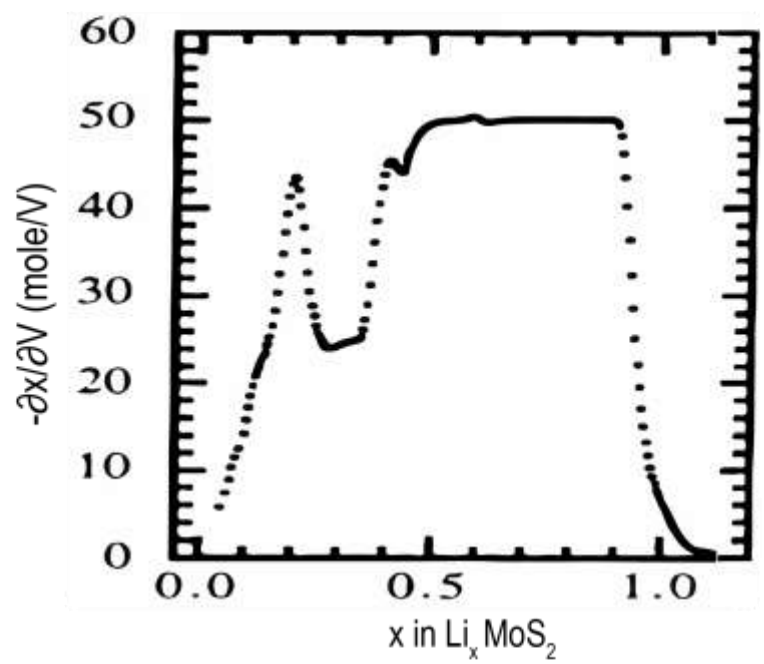

Figure 3.3. Incremental capacity monitored as a function of lithium insertion. Modified from ref [77]

The last phase has gone through many iterations of refinement and analysis using TEM and STM for electrochemically exfoliated flakes. Heising observed that the actual structure was not that of 1T, but that of WTe_2 structure.[76] This structure has significance for our experiment, as the structure is highly correlated to the electronic band structure. In a case where a WTe_2 lattice is obtained, the structure provides the optimal conditions, predicted theoretically, to form the anti-bonding pairs. The formation of these pairs addresses the seemingly contradictory nature of detected sulfide fragments, while much of the lattice structure is maintained, thus indicating that the fragmentation does not occur through deionization. This mechanism corroborates the conversion voltage and possible release of sulfide species around the 0.7 V position, though the decomposition voltage was predicted to occur below 0.1 V.

3.5.4 Classical Crystal Structure Transitions

Traditionally, solid-state intercalation studies focused on avoiding decomposition and monitoring the host structural change as guests were inserted into crystalline hosts. Original MoS_2 investigations focused on characterizing the structure of intercalation product and its effect on the material's properties such as conductivity or magnetism. These bulk experiments were evaluated by XRD as shown in figure 3.4. In early TMDs experiments, stoichiometric amounts of liquid reducing agent (*i.e.* alkali metal in ammonia, butyl lithium) and TMDs were placed in a sealed container and stirred for multiple days.

An example of the structural transition of the MoS_2 lattice can be seen by *ex situ* XRD studies of lithium intercalation via butyl-lithium reduction. As mentioned in Chapter 2, peak position and intensity changes occur only when the interlayer distance (height) is varied.[42-44] In a classic intercalation example, the XRD peak indicating 002 or 001 can be shifted with increasing ion insertion by employing methods of alkali metal in ammonia, organolithium, or galvanic cells. Figure 3.4

demonstrates a slight decrease in the 14.6 2θ degrees and decreases in peak intensity with increased lithium incorporation.

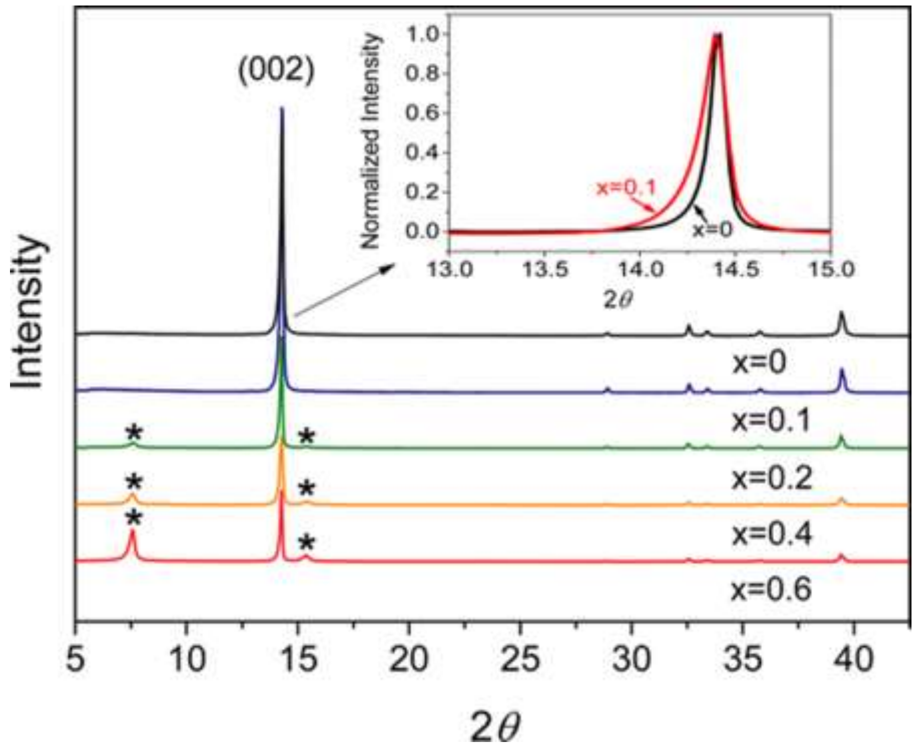

Figure 3.4. XRD characterization of structural transformations in MoS_2 with varied lithium content.[44]

With the emergence of more amorphous materials and electrochemically insertion for battery studies the importance of monitoring with XRD has become less effective at characterizing and monitoring phase transitions. Instead, XRD techniques have been used to compare the structural changes of the electrode before and after ion insertion. Although, electrochemical insertion is a precise method to finely control ion content into TMDs, discharge and charge capacity curves do not accurately determine phase information.

MoS_2 compounds are highly sensitive even in the lithium case. Figure 3.5 show characteristics first discharge curves of MoS_2 for lithium and sodium insertion.

As mentioned above, the number of displayed plateaus does not accurately represent the four phase of MoS_2 intercalation products. The first curve shows a plateau that began at 0.1 molar and ended 1.0 molar ratio of lithium.[72, 77] The second curve possess two plateaus. Whittingham proposed that the discharge of MoS_2 in the sodium case does not show a two-phase transition, but a pseudo two-phase system. In the pseudo-phase interpretation the supercell is formed then is intercalated with ions. Further complications to this understanding in the discharge curve can be seen with synthetic or highly amorphous MoS_2 systems, which present longer capacity curves with increase plateaus. Sodium capacity can vary drastically with synthesis conditions.[82]

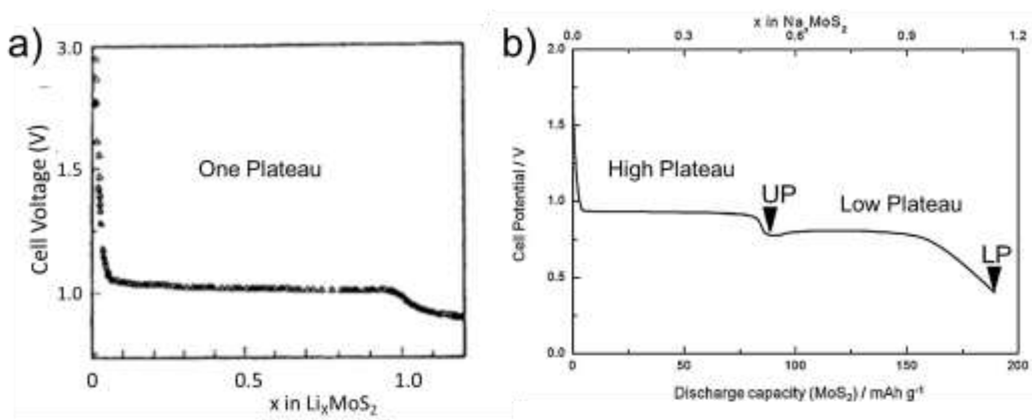

Figure 3.5. Comparison of the cell discharge (ion insertion) of lithium (left) and sodium (right) into MoS_2. [30, 82]

While the type of phases represented by the capacity transition are debated, the transitions that are agreed upon, removal of stacking and the formation of polysulfides, can be confirmed by diffraction studies. Traditional TMDs systems generally show a two-step formation of polysulfides, in which intercalation proceeds first until 1molar concentration is reached and is followed by polysulfide formation, as concentration of ions exceeds the structures capacity.[43, 77]

3.5.5 Electronic Transitions

To understand the differences of MoS_2 reaction, we must examine the electronic structure. Brec insists that the electron transfer is the true driving force. He writes that the lattice distortion energy penalty can only be compensated by changes in electronic structure.[64] We must begin by addressing the misconception held by many in the battery field that intercalation induces the structural changes and major cause of poor capacity is interlayer spacing. Some of the confusion may arise from earliest experiments that used pure lithium or sodium metal in ammonia to insert ions into the lattice. Here the charge separation, electron transfer and ion insertion, were described as simultaneous or driven by ions insertion. However, later experiments that employed highly reducing organolithium or galvanic insertion have highlighted the significance of initial change transfer as driving force of ion intercalation and structural change. A new description has emerged proposing that the lattice behaves as partially reduced polyanion $[(MoS_2)^{-x}]$ matrix.[32, 72]

Band changes can be seen with the phase transformation. Changes in the coordination symmetry dictates the position of dz^2 bonding orbital. The electronic changes are driven by increased stability. Stability can be understood by consider crystal field splitting and strain reduction. Consider the MoS_2 primitive cell, where Mo^{+4} is trigonal prismatically coordinated by 6 shared sulfides, and its splitting diagram (figure 3.6). The cell has 2 d-orbital electrons that can be placed in the dz^2 orbital. If the cell remained in TP coordination when the cell is reduced effectively forming Mo^{+3}, 1 electron would be placed in a higher energy orbital. Instead, as the cell undergoes the 1T transformation each of the 3 d-orbital electrons can be placed into 3 equally degenerate orbitals shown in figure 3.6.[75, 77, 83] Additionally, influence of transformation can be explained with alleviation of torsional caused by coulombic repulsion on one or more reduced sulfur ligands. Nevertheless, phase transformation changes the diamagnetic 2H semiconductor form into a paramagnetic metallic 1T form. A further consequence is the lowering of the d-orbitals is the possible overlap with sp anionic valence bands. This creates opportunities during oxidation of the electrode to oxidize the metal or sulfide ligands forming $S_x{}^{2-}$.[64]

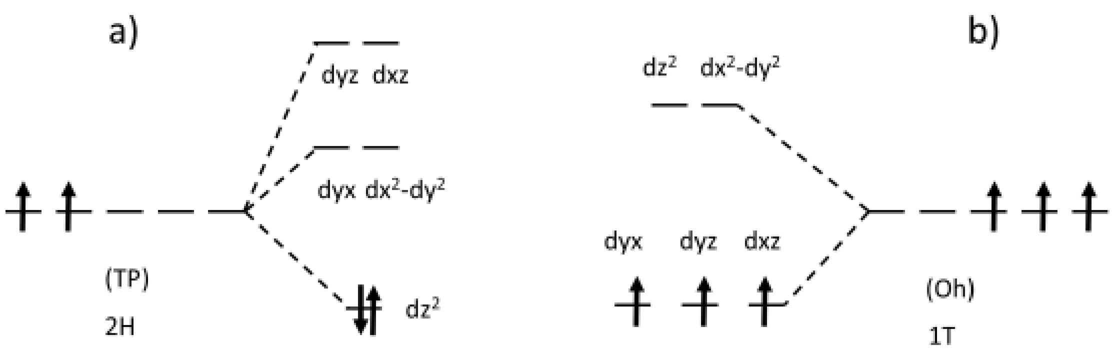

Figure 3.6. Crystal field splitting diagram for 2H and1T forms

The major feature to observe is the nature of band gap. The fermi level of trigonal prismatic (2H form) lies between valence (dz^2) and conduction band confirming natural MoS_2 as semi-conductor. The density of states of 1T octahedral show a fermi level within middle of the valence band indicating the structure is metallic. The difference between 2H and 1T is approximately 1eV.[21] The approximate energy require to generate phase transitions and polymorphs (alternate stacking) be easily overcome through adequate external conditions (*i.e.* heating, pressure).

3.5.6 Density of States Evaluation

The explanation of phase transformation by crystal field splitting and ligand repulsion couple with experimental findings emphasis the important of charge transfer reactions or redox reaction as the driving force for intercalation reactions.[29, 64, 75, 77]

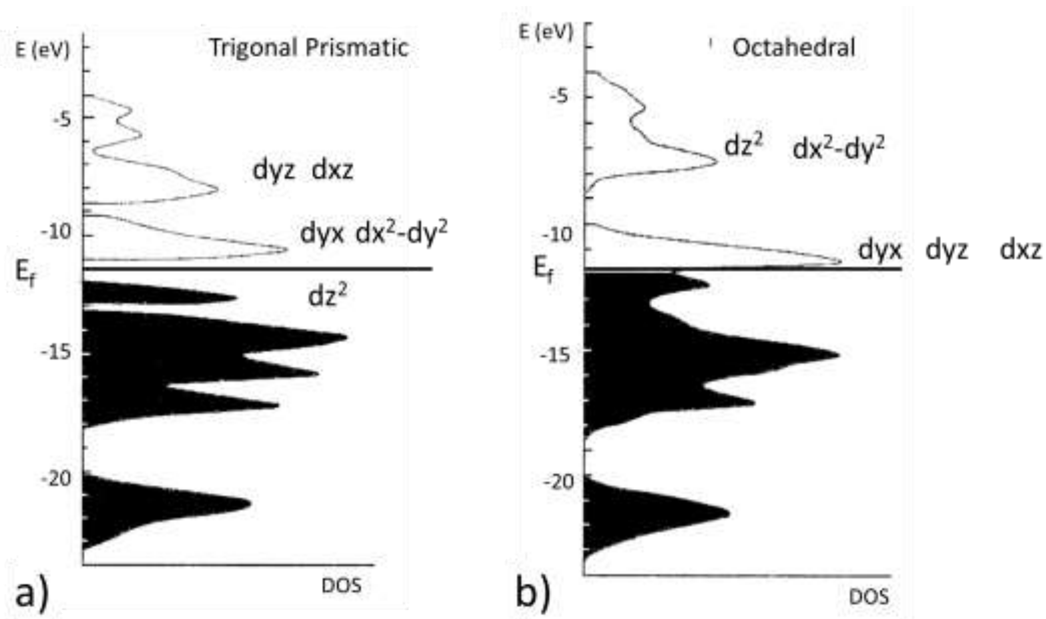

Figure 3.7. Schematic shows the density of states for 2H and1T forms calculated by extended Huckle theory. Shaded region represents occupied electronic states.[72]

3.6 **Nano-structured MoS_2 Fabrication Methodology**

3.6.1 Assembly using Building blocks for electrode material

In a bottom-up assembly approach, building blocks are fabricated before the assembly process. With the NsB MoS_2 electrodes, the building blocks can be synthesized through synthetic methods or exfoliated from bulk MoS_2. The representative morphologies can be generalized to stacked, spherical/hemispherical, and fibers structures. The morphologies are shown in figure1.2. The exfoliation and restack method was first employed to demonstrate potential to create sodium electrode and to understand phase transition of MoS_2 electrodes. Recent articles have switched the synthetic strategy to solvothermal and hydrothermal fabrication methods from previously used exfoliation and restack method. Transmission electron microscopy (TEM) and scanning electron microscopy (SEM) images of a composite MoS_2 and polyethylene (PEO) electrode are shown in figure 1a and 1b.

3.6.2 Thermodynamic Assembly Method via Hydrothermal and Sovlothermal Routes

Hydrothermal and solvothermal routes have gained popularity as they can be used to obtain various novel morphologies and have recently have been correlated with increased capacity. Hydrothermal and solvothermal methods use an autoclave to synthesize and assemble material at high pressure in aqueous and non-aqueous solvent, respectively. These methods can be employed as a one-pot synthesis techniques that often incorporate additional reagents to form composite electrodes.

While synthesis strategy offers advantages such as nanopatterning and novel nanostructure, the strategy has major disadvantages. Impurities such as unreacted starting material can be difficult to remove. Synthetic strategies have not shown scalability and reproducibility to be used for mass production and synthetic parameters can easily form polymorphs and influence stability. TMDS materials as these compounds suffers from inherent sensitivity of synthetic conditions. TMDs, especially MoS_2, have naturally occurring polymorphs. Therefore, products can exhibit various stacking and atomic organization of TMDs, which directly influences intercalation capacity. Jacobson *et al.* showed that sodium capacity can vary drastically with temperature changes, although the same synthesis condition and similar amounts of reagent were used.[82] Alternatively, the synthesis of a polymorph of MoS_2 or MoS_2 electrode with defects may offer explanations for changes in cycling behavior.

The exfoliation and restack method is one of the oldest and simplest assembly strategies, which create an alternating layer structure. This method is highly scalable solution-based method that is safer than the synthetic procedures mentioned above. During the exfoliation, bulk materials are separated into sheets (monolayers) or compounds consisting of multiple sheets. The type of exfoliation process influences the presence of lack of surface charges that drive the restacking process. The restacking process can be triggered by heating, acid or base addition to destabilize the dispersion of sheets causing them to aggregate and precipitate (flocculated) from the solution.[84] The drawbacks of this method are a limited range of structures can be fabricated and, at times, poor precision of the alternating layers. Alternating layers stacking is depended on the quality of the exfoliation. For instance, in the same batch, one alternating structure could consist of monolayer-polymer-monolayer-polymer while and another structure contains polymer –monolayer-monolayer-polymer.

In order to build nanostructured electrodes, uniformed building blocks are preferred. Most exfoliation techniques employ centrifugation to physically separate the desired MoS_2 sheets. The uniformity in materials leads to improve and consistent electrochemical performance. The preference is to creating electrode material through hydrothermal and solvothermal methods. While synthesis of MoS_2 through hydrothermal and solvothermal methods have lately been correlated with high capacity values, their use impedes thorough understand of the surface interactions.

The exfoliation and restacking was adapted to nanostructure unique electrode materials. 2H properties could be restored through oxidation and heat treatment. reported that monolayer 1T could be restored to 2H form has clear advantages over 1T.

Although substantial 2H properties were residue charges remained, to reduce 1T formation three approaches were developed to limit lithium insertion: 1) controlled lithium concentrate into pulverized MoS_2 powder before exfoliation 2) avoided lithium through insertion of small molecules or 3) used solvent and surfactant based exfoliation techniques.

To avoid lithium insertion, small molecules or solvent and surfactant methods were developed to exfoliate layer structure. Since MoS_2 is resistant to most small molecule insertion. We will focus on solvent and surfactant exfoliation method. Solvent and surfactant exfoliation employ molecules of the solvents to lattice match and external forces such as sonication and centrifugal force to physically disrupt the weak van de Waals bonds.

Each of the method above is limited by poor solubility of bulk MoS_2, generally only a few hundred mg can be prepared simultaneously and often exfoliation is time consuming. Colemon demonstrated a highly efficient method increase dispersion and decrease exfoliation time.[85-86] The use of a rotor to drive fluid dynamics leading to the shearing of 2-D materials such as graphite, boronitride, MoS_2

While synthesis offer major advantages such as nanopatterning and well as nanostructure, synthesis lacks control, impurities difficult to remove unreacted starting material, parameters can easily form polymorphs and influence stacking. Jacobson showed that ion capacity can vary drastically with temperature changes, although the same synthesis condition and similar amounts of reagent were used.[82]
A complicated formation influence chemical understanding, though many synthesis show similar shapes there are great differences in performance behaviors.

These complex factors might not increase cost of production, but dense packing of small flakes obscure searches for a fundamental mechanism.
These methods themselves are quite dangerous using high pressures and boiling temperatures.

3.6.3 Exfoliation of bulk to Generate Building blocks

As previously mentioned, the properties and performance of an assembled material or hierarchical structures are heavily dependent on the building block quality and morphology. Therefore, high quality and uniformed building blocks are needed. In addition, a process must meet the requirements to be scalable and have the capability to handle large quantities initial starting material and efficiently fabricate building blocks.

Exfoliation strategies of MoS_2 faces several significant challenges such as low solubility in solvents, non-uniform starting material, use of dangerous reagents, damage or changing molecular structure of the starting material, and long exfoliation times.

Currently the cheapest and most reliable methods for exfoliation are still the traditional methods what is a tape method and intercalation and hydration strategy using butyl lithium. The tape method provides the most efficient way to obtain high quality monolayer MoS_2, however, it suffers from a lack of scalability. The use of butyl lithium in the insertion and hydration strategy is highly scalable method to create monolayer MoS_2, however it creates a distribution of monolayer and few layer sheets, it changes the crystal structure of starting material, creates defects on the sheets. Various other strategies such as electrochemical insertion and hydration have address safety concerns and have precise control over the amount of inserted ions. However, the process, like the one above, fundamentally changes the lattice structure and the conductive additives are difficult to remove from generated sheets. SEM and optical images of an electrochemical exfoliated monolayer flake is shown in figure A.1.

To solve the challenge of transforming the 2H structure to the 1T, surfactant base and solvent-based exfoliation methods were devised. These methods involve interrupting the van der Waals forces between adjacent MoS_2 layers with surfactant, ions, or solvent molecules.[87] These methods can be coupled with physical separation techniques such as sonication, shearing by centrifugal force, and the use of microwaves.

Both techniques have inherent advantages and drawbacks. For instance, surfactant based exfoliation allows for greater dispersion of starting, but the surfactant used can be difficult to remove and residue of the surfactant can interfere with the testing or performance of the assembled structure. The solvent-based method requires little post-processing after exfoliation. The sheets can be easily dried or removed with vacuum filtration. However, the solvent is limited in the capacity of bulk MoS_2 starting material that can be dispersed.

We employ the mechanical exfoliation technique to avoid the chemical transformation into 1T phase. If the converted to the 1T-type annealing can only partially restore some of the bonding within material back to its original 2H-phase. Though Eda *et al.* used XPS to showed the restoration of the bonds, the study did not provide information about the restoration of defects occurring with the 2H-1T phase transformation.[88]

3.7 Use of Redox Mediators

A redox mediator in essence behaves as an electro-catalysis which is capable of enhancing electron transfer from the active material to the electrode. [89-91] The only requirement is that the mediator must have a reversible potential that is higher in comparison with the oxidation potential of active material. Polysulfides have a general oxidation potential around 2.27 V Na^+/Na while PANI has a reversible potential above 3.0 V .[92] Direct contact of the mediator and active material is not a requirement for charge transfer. Aurbach *et al* employed dissolve (non-contact) mediators such as ferrocene, cobaltocene, and dibenzenechromium within the polysulfide half-cell. The authors reported enhancements in voltage profile, prolonged cycling and higher capacity.

Currently, the major method to quantify the effect of mediator employed in the battery is by a comparison of the performance values with and without the compound to determine if an enhancement is achieved. More recently, researchers have preferred solid redox-mediator instead of dissolve species. Following the published work of Nazar, they have use of a surface particularly ‘sulfiphilic’ surface can enhance utilization of insoluble polysulfides while also reducing or inhibiting the shuttle effect of soluble polysulfides (M_2S_2 - M_2S_4) on the surface. Nazar demonstrate the strategy with MgO_2, which chemically transformed LiS_2 into sulfates. Nazar Recent works have begun to employ dichalcogenides, which have history to be used as desulfurization agents such as TiS_2, MoS_2, and CoS_2 as mediators.[89-91]

The principle challenges of this approach is lack of fundamental understanding of the chemical oxidation and reduction chemistries and prohibitive production cost. While many of the performance improvements and fundamental understanding of redox reactions can be understood through use of well-definite nanostructures often the conclusion of nanostructured batteries are convoluted as there is no standardized testing condition for nanostructured batteries. Often nanostructured batteries are composite materials that include additional non-electrode additives such as electrolyte, binder, and additives.

Understanding, especially in batteries, is further complicated as essential non-electrode materials such as binder, graphene based materials (GMs), electrolytes have considerable influence over key characteristic measurements meant to compare and identify the most promising battery systems and designs, such as battery performance and coulombic efficiency.[17, 22]

Chapter 4: Assembly of MoS_2-PANI Surface Sensor for *In situ* Monitoring

4.1 Introduction

MoS_2 nanostructured electrodes are of great interest due to their increasing ion storage capacity and improved performance for rechargeable (secondary) battery applications, but these systems require further study. Researcher have sought the redox mechanism for the MoS_2 system, however, it is particularly difficult to resolve. The difficulties exist due to the complex chemistry of the MoS_2 system, insulation nature of poylsulfide species (complex nature of polysulfide species), lack of characterization techniques for nanostructured materials and use of specific battery additives that obscure the study of the reactions. Two commonly used strategies to resolve the redox chemistry of unknown reactions are: (1) identify the products by their known reduction or oxidation potentials or (2) use the known chemistry of the material, here MoS_2 or Na_2S, to rationalize the reaction steps and assign them sequentially to the various emerging or disappearing peaks.

Lack of agreement between these two approaches has led to a debate on MoS_2 redox chemistry, specifically its CV peaks. Both approaches rely on idealized models such as the voltage potentials of idealized products and intermediates or idealized reactions without consideration for unexpected products and intermediate species or intermediate reactions and rate determining steps such as adsorption-based steps. The debate is further complicated because peaks are shifted from their expected positions and the combination disappearing and emerging peaks conflict with proposed electrochemical reactions. Additional problems are created when expected battery reaction are assigned peaks such as SEI, without corroboration of complimentary techniques. As distinct phases disappear, as is the case with amorphous samples, it becomes imperative that as phases disappears, Whittingham suggested that XRD studies should be performed in conjunction with other characterization techniques.[30]

Many nanostructured electrodes with their polycrystalline composition, high surface area, and distinct saw tooth XRD spectra are more akin to amorphous MoS_2 notably publicize by Whittingham.[42, 93-94] Therefore, to resolve CV peaks and answer important questions, it is critical to build an understanding of the reaction products, battery phenomena, parameter changes/ *in situ* conditions specific to the nanostructured MoS_2 from complementary techniques. This understanding when combined with revised sulfide voltage potentials from constrained polysulfide systems and surface sensitive nanostructured MoS_2-PANI platform can further study on nanostructured systems and propose a general redox mechanism for the nanostructured MoS_2 electrode.

To build a knowledge base, we started with the consensus reaction of the nanostructured MoS_2 electrode. When the electrode is cycled from 0.05 to 2.6, consensus agrees that the reaction couple is sulfides.[3, 34] Next we address the consequences of the active sulfide redox chemistry such as the synthesis of soluble, long polysulfides (sulfur species), which is a missing step required in the proposed chemical mechanism of MoS_2.[26] Ryu *et al*. demonstrated strong, but indirect evidence of a passivating sulfur film on the sodium metal (anode) in a half-cell using XANES and FTIR techniques.[19] The film's formation is only plausible through the formation of soluble polysulfides reaction intermediates. However, the soluble polysulfides remain undetected during the electrochemical transformation of MoS_2 into sulfur. Additionally, Hu discovered that the nanostructured MoS_2 do not simply decompose (dissociate) during the battery process, but can continuously delaminate into the sodium case into single layer sheets using TEM.[31] Lacey's work established where SEI occurs and reported some electrolyte interactions. Park's pioneering work provides an established CV profile to start from and shows the impact of conformal polymer coatings.[94] Xiao *et al.* corroborate the influence of polymer coating boasting a CV profile with high clarity.[27] Hongli *et al.* assigns the peak of ~ 0.8 V (Na^+/Na) to be associated with the 2H form. Some researchers presents that the peaks are assigned to an intercalation and a conversion reaction or alternatively interpreted as classical structural transition from the 2H to 1T.[14, 31] The transition to sulfur redox chemistry widely viewed as irreversible process.[95]

To resolve these issues and learn more about the fundamental behavior, the phase chang[27]es, and the redox mechanisms, we designed a PANI/MoS_2 system devoid of graphene. Herein, we systematically explore the electrochemical nature of PANI/MoS_2 hybrid in SIBs by creating a thin conformal layer of PANI polymer on few-layer MoS_2 flakes to probe the surface.

4.2 Results

The fabrication processes of the alternating MoS_2 (3-5 sheets) and PANI layers composite electrode is shown in figure 3.7. PANI surface modification was confirmed by cyclic voltammetry, XRD, TEM, and SAED, (Appendix A.2-A.3).

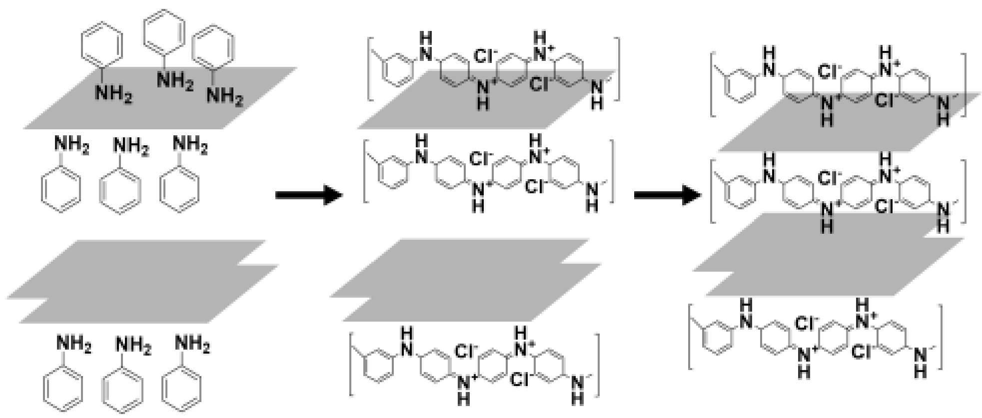

Figure 4.1. Schematic of the MoS_2-PANI synthesis process. a) *In situ* solution based synthesis process in which MoS_2 few layer flakes were coated with polyaniline.

4.2.1 Electrochemical Testing

The overall reaction mechanism of the MoS_2 was investigated by cyclic voltammetry (CV) with a scan rate of 0.1 mA/s using an alternating MoS_2-PANI platform, shown in figure 4.2. We focuses on the 0.4 V- 2.6 V window range for our study as this range represents the largest debate of the redox mechanism due to the heterogeneous composition of the electrode. The composition was determine to include the four distinct phases, which could potentially include the 2H, 1T, supercells and possibly polysulfides.[29, 77] The above discussion and image of large flake that has undergone intercalation using a galvanic cell provides visually illustration of the high strained nature of the MoS_2 within the battery (Appendix A.1).

Two types of CV comparisons were devised to elucidate which peaks were correlated to MoS_2 and polysulfide redox chemistry. Each comparison, a continuous run that used multiple voltage windows and fresh electrodes run in the specified window as controls, in vital to gain insight into the redox mechanism. For the continuous cycle experiment, we will focus on establishing support for our proposed mechanism using the first two windows then compare the results to electrodes run in the 0.4 - 2.6 V. In the continuous run experiment, an electrode was evaluated at three voltage windows of 0.8 - 2.6 V, 0.7 - 2.6 V, and 0.4 - 2.6 V. Additionally controls are required as the battery behavior can deviated based on the cycling ranges (voltage window); however, the mechanism remains unclear.[94] Next the above results from the first windows were contrasted against voltammograms of an exfoliated MoS_2 electrode and MoS_2-PANI electrode in a deep discharge window (0.05 -2.6 V) to confirm the CV profiles of MoS_2 and polysulfides, respectively. Additionally, possible electrolyte decomposition and interactions are evaluated using sodium perchlorate ($NaClO_4$) as the electrolyte salt (figure 4.3). Finally, by vary the scan rate and using the definition of reversibility, we examine the redox pairs for the most prominent and consistently recurring peaks.

For the continuous cycling, the electrode was first cycled between 0.8 V - 2.6 V. In figure 2a, curves for 1st, 2nd, 5th, and 8th cycles are plotted and compared. The first cycle, initiated in the negative direction toward the cut-off voltage, exhibited a small cathodic peak at ~0.80 V and an anodic peak at 1.0 V. In subsequent cycles, both peaks become more pronounce, increasing in intensity and slightly shifting in the positive voltage direction. We assign the increasing cathodic peak to the increase concentration of 1T lattice sites within the electrode. The anodic peak (1.0 V) has been rarely reported, but both authors agree that this interaction is more complex than simple intercalation and does not completely correspond to the cathodic 0.8 V peak.[7, 96] We argue that this peak should be assigned to an intermediate of sulfide (S_2^{2-}) species. For the first time, an additional reduction feature at ~1.5 V attributed to SEI formation can be observed during the first scan by comparing the width of the initial cycle with the preceding cycles. The overall CV profiles and trend were confirmed by continuous CV run conducted of a MoS_2-PANI electrode fabricated with 40% molar amount of PANI (Appendix). The CV profile displaced a similar peak position and cycling trend with increasing cycles in 0.8 - 2.6 V window.

To further investigate the redox mechanism, the second window was selected, where the cutoff voltage was lowered to 0.7 V (figure 2b). The cycles evaluated under the second window are shown in figure 2b for cycles 9, 10, 13 and 18. In the 9th cycle, two reduction peaks at 0.7 and 0.8 V, and four oxidation features at 1.09 V, 1.34 V, 1.58 and 2.34 V. In subsequent cycles, the moderate oxidation peaks became more pronounced in the 1.2 V – 1.6 V range and weak shoulders in the 2.2 V - 2.4 V as the oxidation peak at 1.09 V decrease proportionally. The small reduction features also emerge and gradually increase at 0.94 V, 2.3 V, and in the 1.2 V – 1.5 V range, as the peak at 0.86 V decreased after the initial cycle. The change from a sharp 0.86 V in the initial cycle to a broad peak at 0.9 V in the preceding cycle is a characteristic peak shift of the MoS_2 system and an indicator of a more conductive MoS_2 compound.

To address possible cycling dependency and to verify that the peaks are independent of an aged electrode, a fresh electrode was evaluated at 0.7 V cut-off (Appendix A.5). Every peak position and trend reported in figure 4.2b was observed in the profile of this control overall. However, the cycle number in which the peaks emerged are an important difference. One such difference can be seen when comparing the initial cycles of each electrode. The control has only two pronounced peaks, one reduction peak at 0.7 V and one at oxidation peak at 1.14 V. The absence of a peak at 0.8 V and shoulders in 1.2 V – 1.6 V and in the 2.2 V - 2.4 V ranges are notable. The control's CV profile also shows clear difference in the decline of oxidation peak (1.14 V). The peak at 1.14 V (Appendix A.5) decreases sharply as compared to gradual decline in the continuous cycled electrode in figure 4.2b.

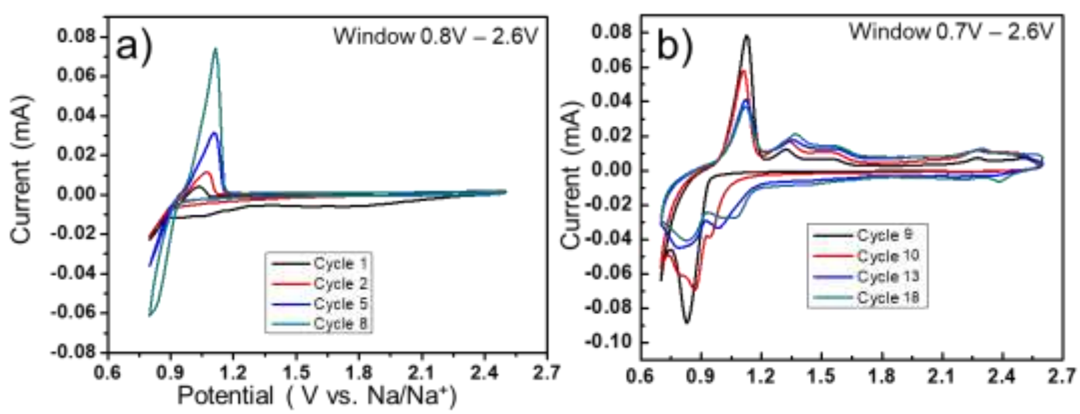

Figure 4.2. Cyclic voltammetry of MoS_2-PANI (20% wt.) Na-ion half-cells where a, and b are testing conducted on the same battery. a) Cyclic voltammetry test from 0.8-2.6 V vs. Na/Na^+ at a scan rate of 0.1 mA/s b) from 0.7-2.6 V vs. Na/Na^+ at a scan rate of 0.1 mA/s

The third window, 0.4 -2.6 V, was employed to confirm the peaks in the 0.7 - 2.6 V window and assess a possible mechanism in this new range. The cycles evaluated under the final 0.4 - 2.6 V window are shown in Appendix A.6 for cycles

19 and 29. In the 19th cycle, moderate oxidation peaks emerged in the 1.2 V – 1.5 V range, at 2.3 V, and weak shoulders at 2.4 V as the oxidation peak at 1.0 V decrease proportionally.

Figure 4.3a-b shows voltammograms of fabricated MoS_2 and MoS_2-PANI electrodes evaluated under different cycling conditions. As shown in figure 4.3, anodic and cathodic peaks appear consistent with the cell run in the 0.7 - 2.6 V window (figure 4.2b) providing support that the same redox reaction occurs regardless of the varied cut-off voltage. Each voltammogram shares characteristic and pronounced peaks, such as the reduction peaks at 0.7 V and 0.8 V, and the anodic peaks at ~1.30 V and 2.3 V in the initial cycle (figures 4.3a-d). However, the electrodes with PANI coatings show an increased number of reduction and oxidation peaks, which produce identifiable redox couples (figure 3b-d). Each of the curve shares a typical initial anodic scan composed of four oxidative features at 1.34 V, 1.55 V, 2.34 V and 2.5 V. In second and subsequent cycles, the CV curves of MoS_2-PANI show three similar reductive features at 1.14 V, 1.34 V, and 2.24 V and three corresponding oxidation peaks/shoulders at 1.34, 1.55 V, and 2.34 V. With the exception of figure 4.3c, each MoS_2-PANI electrode shares the same trend in which the peaks/shoulders of the redox couples 1.14 V & 1.34 V (cathodic, anodic), and 2.24 & 2.34 V continue to increase with each consecutive cycle.

Though the above-mentioned similarities describe the consistent reactions of the electrode, the differences in the CV profile aid in the elucidation of the redox mechanism. The voltammogram of exfoliated MoS_2 flakes was used as a control (figure 4.3a) to determine the appropriate peak positions. The peak positions are slightly lower due to less conductive nature of the electrode.[21, 28, 97] As seen in figure 3a, the CV curves shows oxidation features and their decreases in subsequent cycles that are in close agreement with Park's MoS_2-PEO electrode.[94] The initial cycle display an oxidative peak at ~1.34V and two shoulders at ~1.50 V and ~2.34 V, corresponding to Na_2S, longer polysulfides (i.e. Na_2S_{4-6}) and sulfur, which gradually decreases in 2nd and 5th cycles. The loss of peaks in proceeding cycles demonstrates a lack of reversibility of electrode due to the insulating nature of the sulfur species. The two large reduction peaks at ~0.7 V and ~0.80 V are typical of the first scan of expanded restacked MoS_2.

After the 2nd cycle the reduction peaks at ~0.8 V or 0.9-1.0 V are not present, which indicates the previous stacked crystal structure no longer exists. Removal of the coherent stacking after two cycles was confirmed by XRD and the continued crystallinity was visualized by SAED (figure 4). This absence of the peaks at 0.7 V and 0.8 V using the 0.4-2.6 V is unlike the profile generated in 0.7 -2.6V window, in which the peaks at those positions still appear beyond the 2nd cycle. During the 5th cycle the anodic peak 1.35 V and cathodic peak at 1.14 V continue to increased following the general MoS_2-PANI electrode trend.

MoS_2-PANI in the deep discharge (0.05 V- 2.6 V) has a first cycle that is not well-defined similar to the MoS_2 electrode with the exception of the peak at 0.05 V (figure 4.3c). However, in the 2nd cycle and subsequent cycles particular peaks such as 1.14 V & 1.34 V (cathodic, anodic), and 2.24 & 2.34 V, maintain high clarity with each increasing cycle. The peak at 0.05 V is attributed to sodium plating as voltage approaches the reduction potential of sodium ions. Figure 4.3c also displays no shift to ~1.0 V in its 2nd cycle. Furthermore, the absence of peaks at 0.7 V and 0.8 V in the 2nd cycle and large profile in the 1st cycle suggest that the structure was destroyed. Additionally, the overall lack of feature clarity in the CV curves suggests the available species is quite insulating.[9] CV shape In contrast to the trend of the other MoS_2-PANI electrodes, the peak intensity decreases with increased number of cycles.

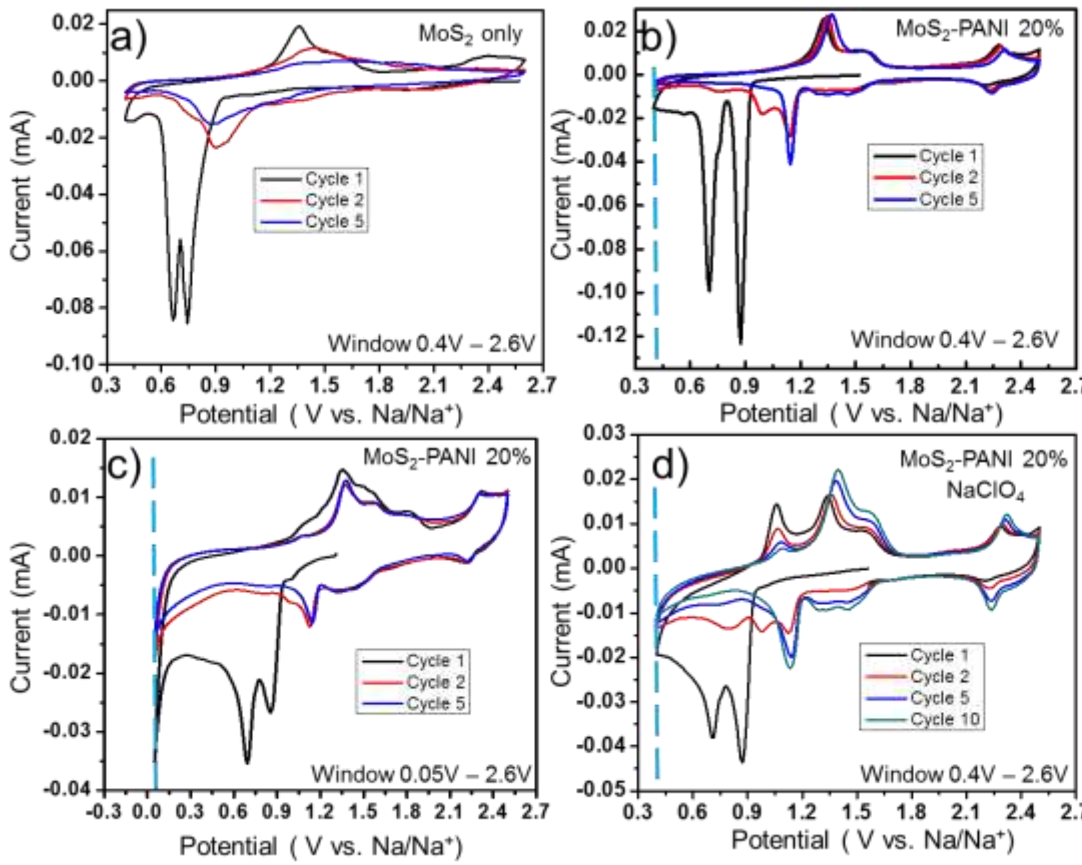

Figure 4.3. Cyclic voltammetry of MoS_2-PANI and MoS_2 Na-ion batteries. a) Cyclic voltammetry of few layer MoS_2 without PANI. b) Cyclic voltammetry of few layer MoS_2-PANI (20% wt) in the voltage window 0.4-2.6 V vs. Na/Na^+. c) Cyclic voltammetry of few layer MoS_2-PANI (20% wt) in the voltage window 0.05-2.6 V vs. Na/Na^+ which shows the intentional formation of Na_2S. d) Cyclic voltammetry test from 0.4-2.6V vs. Na/Na^+ which demonstrates the sulfur shuttling and absorption extends to $NaClO_4$ as well.

Sodium perchlorate ($NaClO_4$) is a commonly used salt for the MoS_2 electrodes. Lacey reported softer thinner SEI film resulting from a combination of the MoS_2 electrode and $NaClO_4$ electrolyte than an analogous graphite system.[98] He proposed that the film texture was due to the less reducing nature of $NaClO_4$ electrolyte. To investigate the potential less reducing nature the electrolyte on the reaction mechanism, $NaClO_4$ electrolyte was evaluated over the 0.4 V-2.6 V window. The CV profile has similar redox couples as other CV with cut-off voltages of 0.4 V (figure 4.3d). More importantly, figure 4.3d shows a CV curves with a distinct anodic peak at 1.0 V. As previously mentioned, this peak was assigned to be an intermediated species (figure 4.2). The decline of anodic peak's intensity and correlated increase of peak intensity at 1.40 and 1.50 V is consistent with figure 2b. The overall peak behavior was confirmed the behavior seen in cycles of the other electrode evaluated in the 0.4 -2.6 V window. The behavior was quite stable and repeatable as the peak increase at was seen for 100 cycles, without any signs of stopping (Appendix A.7). Table 4.1 summarizes all the CV peaks and set up comparisons between the 0.4-2.6 V window, 0.05 -2.6 V window, and Park's CV data.

Table 4.1. Summary of the Cyclic Voltammetry Features seen during MoS_2 Cycling

Electrode Range Electrolyte	MoS_2-PANI Window 0.4 -2.6 $NaPF_6$ in Ethylene Carbonate / Dimethyl Carbonate			MoS_2-PEO Window 0.4 -2.6 $NaCF_3SO_3$ in ethylene glycol dimethyl ether *Electrochimica Acta.*, **2013**, 92, 427–432			MoS_2-PANI Window 0.05 -2.6 $NaPF_6$ in Ethylene Carbonate / Dimethyl Carbonate		
Cycle 1	# of Peaks	Anodic (V)	Cathodic (V)	# of Peaks	Anodic (V)	Cathodic (V)	# of Peaks	Anodic (V)	Cathodic (V)
	1	1.33	0.7	1	1.31	0.7	1	1.36	0.05
	2	1.52	0.87	2	1.51	0.87	2	1.5	0.69
	3	2.28	2.21	3	2.28		3	1.79	0.86
	4	2.5		4	2.46		4	2.31	2.20
							5	2.5	
Cycle 2	# of Peaks	Anodic (V)	Cathodic (V)	# of Peaks	Anodic (V)	Cathodic (V)	# of Peaks	Anodic (V)	Cathodic (V)
	1	1.34	0.76	1	1.33	0.77	1	1.37	0.05
	2	1.52	0.99	2	1.52	0.93	2	1.51	0.77
	3	2.29	1.13				3	1.78	0.93
	4	2.5	1.33				4	2.32	1.13
	5		1.44				5	2.50	1.38
	6		2.23				6		2.21
Cycle 5	# of Peaks	Anodic (V)	Cathodic (V)	# of Peaks	Anodic (V)	Cathodic (V)	# of Peaks	Anodic (V)	Cathodic (V)
	1	1.37	1.14				1	1.38	0.05
	2	1.54	1.34				2	1.51	1.14
	3	2.31	1.45				3	2.32	1.34
	4	2.49	2.24				4	2.50	1.45
							5		2.22

To confirm the quasi-reversibility of the redox couples and provide additional evidence that the proposed reaction is driven by surface bound redox mechanism an electrode was tested at varying scan rates of 0.05 mV/s, 0.1 mV/s, and 0.3 mV/s (Appendix A.8). The peaks position shifted slightly as a function of the scan rate and peak current changed proportionally to the rate. However, the ratio of peak current of each redox couple was ~1 at higher scan rates. This data offers clear indication of quasi-reversibility and diffusion controlled and surface bound nature of the reaction mechanism.

4.2.2 Structural Evolution of Nanostructured Electrode

We used a collection of techniques, XRD, TEM, and SAED, to examine structural evolution of nanostructured electrode before and after cycling, confirming modification by the PANI, and investigating the lack of coherency in the stacking direction and crystallinity of in situ-generated single layer MoS_2, respectively. The structural evolution of the hybrid electrode cycled between 0.40 V and 2.60 V was characterized by *ex situ* XRD (figure 4.4). Figure 4.4 shows three spectra for the electrode, before cycling, after 2 cycles, and after 50 charge and discharge cycles (100 total cycles). Each spectra contains peaks associated with MoS_2, carbon black (a battery additive), and alumina (the current collector).

The spectra of the new fabricated electrode is in close agreement with bulk MoS_2.[42-43, 99] The largest peak is indexed by 002 plane, which indicates the stacking of 2H-MoS_2 layers.[42] The peak is slightly shifted to a lower 2θ position when compared to that of the bulk MoS_2. After one sodiation and one desodiation cycle (two cycles), the XRD spectra displays 1T-MoS_2 peaks with dramatically reduced intensities. This spectra only contains one MoS_2 peak, which is denoted as 001 peak. When the MoS_2 is inserted with high ion concentrations, the multiplicity of the host is split when the host is reversibility changed from its 2H form to the 1T form. Upon 100 total cycles, the prominent characterization peaks were not detected. The removal of these peaks demonstrate a loss of stacking, but does not provide evidence that the lattices have lost their respective crystallinity. The detection of 103 peak at 40 degrees suggest that crystalline or semi-crystalline single layer MoS_2 persist in the electrode, which is consistent with the findings of in literature.[6, 25, 31] Similar to the work of Park, the battery still generated a small capacity of ~50mAh/g.

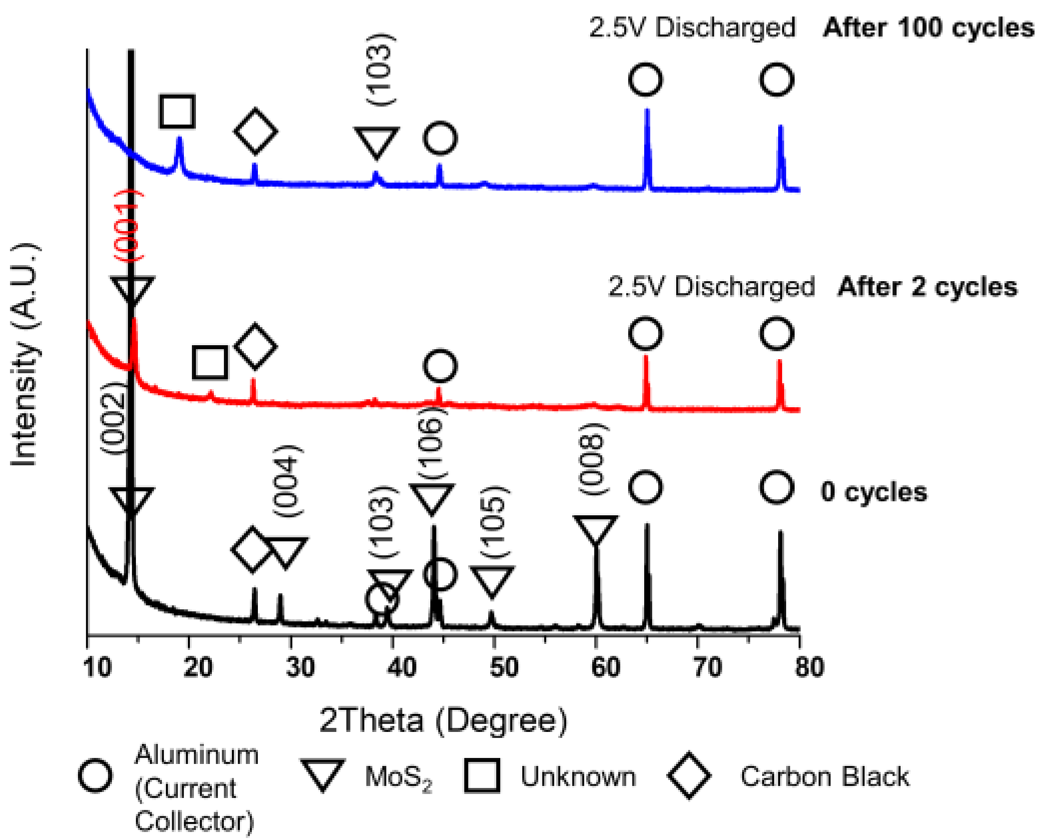

Figure 4.4. XRD characterization of structural transformations of the MoS_2-PANI electrode. XRD diffractograms of MoS_2-PANI hybrid material. The planes are index either to bulk 2H-MoS_2 or 1T-MoS_2 according to literature. [42-43, 99]

While other works have indirect proof of the persistent lattice planes through electrochemical measurements, no work has verified the crystallinity through, SAED method, which would provide conclusive visual evidence. We confirm the evolution of the nanostructured electrode and crystallinity through characterization by SEM, TEM, and SAED. Figure 5a shows the initial state of the assembled MoS_2-PANI electrode, revealing a consistent mixture of PANI attached to MoS_2 flakes (figure 4.5a). The morphology and lattice structure of the uncycled MoS_2-PANI composite were further investigated by transmission electron microscopy (TEM) and SAED (figure 4.5b and 4.5c). TEM images show few-layer flakes coated with PANI and SAED diffratogram displays the presence of MoS_2 crystalline hexagonal lattice and polymer intercalated between layers (faint circle around atom) before cycling. After cycling, TEM and SAED images confirm the presence of lattices structures support the explanation of intercalation induced shearing of lattice planes (figure 4.5d and 4.5e).

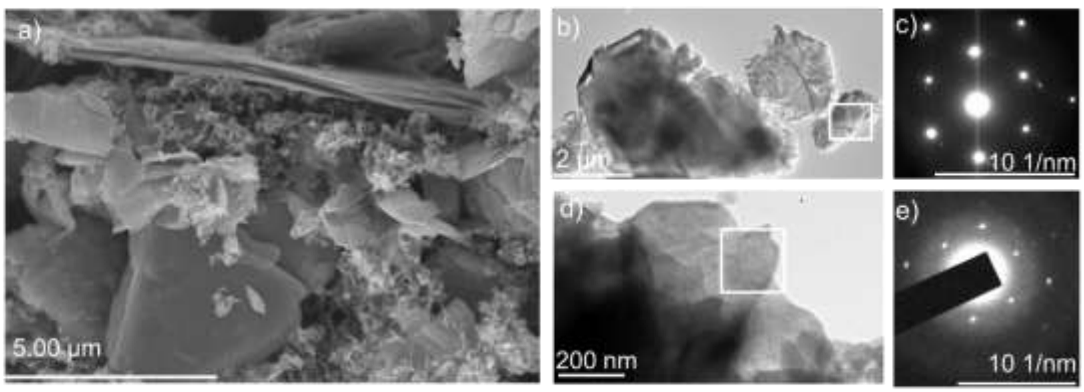

Figure 4.5 SEM displays the cross section of the 20% PANI a) zoomed-in before TEM and SAED examine morphological changes. TEM and SAED of hybrid MoS_2-PANI flakes. b) TEM image of few layer MoS_2-PANI (20% wt.) before cycling c) SAED of few layer MoS_2-PANI (20% wt.) reveals hexagonal structure. d) TEM image of few layer MoS_2-PANI (40% wt.) after cycling the surface of the flake is amorphous however the edge contains the same lattice structure e) SAED of few layer MoS_2-PANI reveals a similar lattice structure possibly an indication of the stability of certain MoSx flakes.

4.2.3 Compositional Analysis

The composition of an electrode cycled in the 0.4 V-2.6 V window was inspected using X-ray Photoelectron Spectroscopy (XPS). The deconvolution yields the two sulfide oxidation states around the binding energy around 162.25 eV and 160.46 eV (figure 4.6). The majority of sulfur species with the binding energy of 162.25 eV has an oxidation state of -2, which characteristic of bonding to the MoS_2 lattice. The lower bind energy, 160.46 eV, describes sulfur species with oxidation state of -1 for molecules such as Na_2S_2.

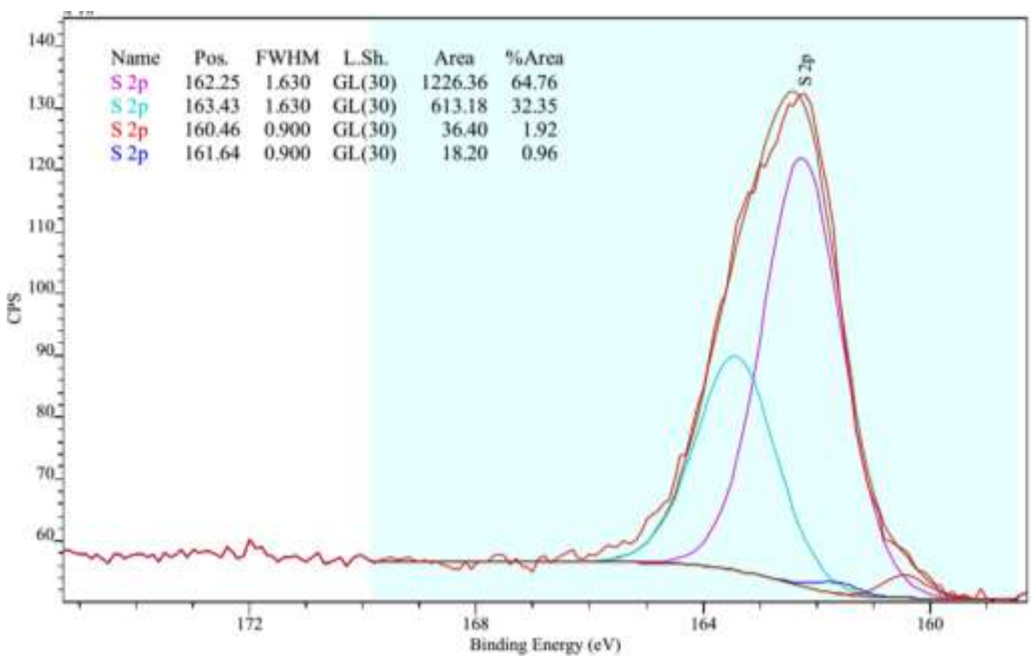

Figure 4.6. XPS spectra of cycled electrode MoS_2-PANI 20% electrode. The peak at 162 eV reflects the contribution of both MoS_2 and Na_2S sulfur bonding. As expected a small peak in the 160 eV shows that sulfur with an oxidation state (-1) as in the molecule Na_2S_2 is present. The calibration point is 284.8 eV from adventitious carbon.

4.3 **Discussion**

4.3.1 Structural Evolution of Nanostructured Electrode

The shape, intensity, and position of the 002 XRD peak reveal important parameters of the nanostructured electrode. The presence and sharpness of the peak demonstrates an increasing number stacked layers. Additionally, the first large peak intensity shows stacking layers to be orientated perpendicular to the incident beam. This confirms the assembly of the 2D building blocks. The slight shift of the peak's position to lower 2θ degrees than the bulk MoS_2 and the control indicate an expanded interlayer spacing; likely due to PANI molecules reside between the stacked layers.[5] The control electrode was fabricated by building blocks, which were exfoliation using solvent and restacked using acid. The interspatial distance was calculated to be 0.61 nm which agrees with the interlayer distance of bulk MoS_2. Using the peak and the Scherrer formula, the average size of the crystallites was estimated to be ~130nm.

After 2 electrode cycles, the decrease in intensities for the only remaining MoS_2 peak and its position at 15 degrees, close to 2θ position of the bulk is explained by removal of coherent stacking and low abundance MoS_2 layers with partial or no PANI conformal coating. After 50 full cycles (100 total cycles), in the 0.4 V – 2.6 V range only one peak remained around 40 degrees, which suggests that some lattice planes may remain intact, while the coherency in the stacking direction was destroyed. The persistence of a few MoS_2 lattice planes is in good agreement with previous reports.[20, 94]

By combining conclusions from CV curves combined with the XRD data suggest that after the first cycle, intercalation reactions are not likely responsible for the performance of the battery.[3, 27] Therefore non-intercalative processes become the dominant mechanisms.[25] The removal of the coherent stacking seen in the XRD after few cycles is correlated to CV curves in the 0.4 V – 2.6 V and 0.05 V- 2.6 V windows, where removal of peaks at 0.7 V and 0.8 is observed after two cycles.

Many papers suggestion that conversion starts in at 0.7 range, however, what has yet to be explained is why does lattice planes persist until 0.4 V. Furthermore, in the absence of stacking many researchers have suggested adsorption becomes the dominate process, yet clarity has not been given to what species is being adsorbed, the cause of the peaks on cyclic voltammetry curve, and the diffusion effects seen when varying the scan rate. Each of these observations can be clarified with the formation of a polysulfide species that can grow in length and become soluble in solution. More clearly, we suggest that a deep discharge is not required before polysulfides become the active species within the battery.[22, 27] Furthermore, we proposed that single monolayers have an additional role, as surfaces that promote polysulfide binding and growth, which goes beyond the ion adsorption described in literature.[6, 25, 31]

4.3.2 Determination of MoS_2 Redox Reactions

We believe the platform's clear cyclic voltammetry peaks allow the CV potentials to be used as fingerprints to elucidate the reaction mechanism of the nanostructured MoS_2 electrode. Each voltage window was created by choosing an upper voltage limit and a lower voltage (cut-off or terminal voltage). The upper voltage of 2.6 V was selected to minimize electrolyte decomposition and because the voltage is traditionally associated with the MoS_2 electrode. The cut-off voltages (0.8

V, 0.7 V, 0.4 V, 0.05 V) were selected because of Lacey *et al.*'s observations and similar CV values were reported in literature for their possible significance to MoS_2's redox reactions. Though many of the peaks are under dispute, we choose values that are corroborated by known solid-state intercalations studies and works conducted by founding established scientists of this field.[27, 94] Table 4.2 shows a summary of features at key voltages that occur at potentials reported on MoS_2 CV curves.

Lacey's work established an upper voltage limit to investigate MoS_2 electrodes. Lacey, using atomic force microscopy (AFM), observed no sodiation occurring at or above 1.0 V. A few articles have suggested intercalation for sodium begins at 0.9 V. However, according to our data a cut-off voltage of 0.9 would have resulted in no peaks and a box-like CV curve. The box-like curve of MoS_2 is characteristic of pseudo-capacitive behavior and has been reported before in the works of Fang and Gigot.[3, 100] Furthermore, Sha fabricated a MoS_2/PANI capacitor, which showed pseudo-capacitive behavior using a scan rate of 20mV/s between −0.7 and −0.2 V (versus SCE), which corresponds to an approximate range of 1.8 V- 2.5 V (v. Na^+/Na).[4] Therefore, our cut-off voltages are set to examine the prediction that the terminal voltages of 0.8 V and 0.7 V, which are described phases dominated by semi-reversible ion insertion into lattice and by the presence of 1T coordination. Additionally, a cut-off of 0.8 V was predicted to minimize structural damage and indicate a potential in which sodium intercalation is semi-reversible.[94] The cut-off voltage of ~0.4 has been correlated with the appearance of wrinkling, suggested to be destruction of the laminar structure and the onset of polysulfide formation.[19, 25, 79, 98]

Cut-off voltages below 0.1 V have been reported to be dominated by short polysulfide and has even been claimed to generate sulfur by decomposing the MoS_2 lattice.[27, 31]

Table 4.2. Comparison of Significant Voltage Potentials and CV Peaks

Window	Features (V)	Explanation	Reference
0.4-2.6 V 0.1 mV/s	Anode (4): (1.34, 1.5, 2.34, 2.5) [1.34, 1.5, 2.34, 2.5] Cathode (2): (0.7 V and 0.86 V) [1.0, 1.2, 1.3, 1.4, and 2.24] Cathode: 0.8-0.7 0.7 0.4 (SAED) Anode: 1.0	A number of cathode and anode peaks increased with each cycle (~100) All peaks in continuing cycles are related to sulfur	**This work**
0.4-3.0 V AFM study	Cathode Discharge: 1.5< 1.0> 0.4	SEI formation Sodiation Wrinkling	Ref:[5] Nano Lett.**2015**, 15, 2, 1018-1024
0.4-2.6 V 0.1 mV/s	Anode (4): (1.33, 1.53, 2.28, 2.5) Cathode (2): (0.7 V and 0.88 V) Cathode: 0.85< 0.80	Peaks declined with each cycle Reversible insertion Distortion of structure (microstrains)	Ref: [94] Electrochimica Acta., **2013**, 92, 427–432
0.005-2.6 0.1 mV/ s	Anode (3): (2.24, 1.80 and 0.45) Cathode (3):(0.79, 0.61, 0.005) [0.7 and 1.4] Cathode: 1.4 0.7 0.4	Intercalation of Na-ions into host Conversion Loss of crystallinity	Ref: [25] Scientific Reports **2015**, 5, 12571
0.4-3.0 V XRD study	Cathode Discharge: 0.9 0.75	Intercalation (shift towards lower angle) Peaks indexed according to $NaMoS_2$	Ref: [6] Chem. Eur. J. **2014**, 20, 9607 – 9612
0.01 - 3.0 TEM /XRF study	Cathode Discharge: 0.7 0.5	Conversion Blurry TEM (sulfide dissolution)	Ref:[19] Nanoscale , **2014**, 6, 10975-10981
0.5-2.7 V 0.05 mV/s RTNa_2S_x Study	Anode (3): (~0.9, 1.7, 2.5 V) [0.9, 1.7] Cathode (2): (0.9 V and 1.5 V) [0.9 V and 1.55 V] anode: 1.7 cathode: 0.9 1.7	Peaks decrease dramatically in 2nd cycle Oxidation forming Na_2S_4 Reduction forming Na_2S Reduction forming Na_2S_4	Ref: [101] Nano Lett. **2017**, 17, 1863−1869
0.8-2.7 V 0.05 mV/s RTNa_2S_x Study	Anode (1): (1.75 V) Cathode (2): (1.1 V and 1.45 V) [1.1 V and 1.55 V] cathode: 1.1 1.45	Peaks decrease gradually w/ exception of reduction peak 1.1 V (grad. increase) Reduction forming Na_2S Reduction forming Na_2S_2	Ref: [102] Adv. Mater. **2014**, 26, 1261–1265

Anode/Cathode (initial number of cycles): (voltage potentials)
[Cycles that appeared after initial (1st) cycle]; RT (room temperature)

In the 0.8 -2.6 window, our platform demonstrated a high sensitivity to surface reactions and a critical step of the MoS_2 mechanism. The shoulder in the first cycle in 1.5 V range is associated with the formation of the SEI.[98] This is the first time this feature has been reported from CV curves. Our CV curves do not indicate any additional SEI formation after the 1st cycle. Nevertheless, SEI for sodium system are reported to be more complex than those of the lithium system.[103] If an SEI layer formed beyond the first cycle in other voltage windows, the film formation would be difficult to detect because of abundance of sulfide species presence. The SEI formation overlaps the voltage range of some prominent sulfide reduction peaks.

To the best of our knowledge, the anodic 1.0 V has only been published once for potassium insertion into MoS_2 and report in the Appendix material for a sodium system. However, both articles agree that this interaction is more complex than simple intercalation and does not correspond to the cathodic 0.8 V peak.[7, 96] The peak continues to increase with each subsequent cycle, but we expected that the reach a maximum at a certain point and possibly decrease or disappear completely. Due to this behavior, we propose that this peak is attributed to sulfide formation at the surface (adsorption). The sulfide adsorption is confirmed by continuous run of 40% PANI system (Appendix A.9-10). During the scan of 0.8 -2.6 V window of this electrode, the peak at ~1.0 V reaches a saturation point at 1.20 V. The saturation point occurs in this system because the increased concentration of PANI monomers during the fabrication process promotes the formation of PANI fibers instead of a conformal coating. As a result, the formation of a fiber reduces the exposed surface area, which determines the amount of sulfides that can react.

Researchers have proposed that 0.8 V and 0.71 V represent a two-step phase transformation to types of the product and active species are under debate. We agree that first step constitutes (1) Na is inserted into the lattice structure forming (1T) Na_xMoS_2. However, we are not convince that the 2nd reduction peak describes (2) the formation of metallic Mo and $2Na_2S$.[14, 22] We argue that the presence of an adsorption phenomena or unstable intermediate (S_2^{2-} sulfide formation at the surface) reveals that reduction feature (~0.8 V) describe more than intercalation or transformation from 2H to 1T, but a possibility for a multi (~1-2) electron transfer process (saturation or reduction 1T phase) that begins at 0.85 V range. As discussed above, multiple phase transition can correspond to single analytical feature. Authors have cited that the creation of defects in the lattice could precede the onset of polysulfide formation.[104] Wu explained that the sulfur vacancies would inject charge into the lattice accelerating transformation into the 1T phase.[105-106] This process has a fundamental basis in the overlap of the conduction and valence bands such that during oxidation, electrons are removed from valence band causing anti-bonding hole pairs to form. Upon lowering the cut-off (to 0.7 V), the S_2^{2-} species can be further oxidized to form polysulfides.

In the 0.7 - 2.6 V window, CV profiles begin to show standard anodic and cathodic features characteristic to MoS_2 electrodes. In addition to the peak position peaks shifts especial for the prominent reduction peaks are seen starting from the 2nd cycle. A shift in the peak position from the second cycle is attributed to the increased in conductivity that comes from the transition form the semi-conducting 2H phase to the metallic 1T phase. To further investigate the onset of polysulfide formation, the second window was selected, where the cutoff voltage was lowered to 0.7 V (figure 2b).

It is important to make the distinction that upon reaching the 0.7 V describes presence the large quantities of 1T phase, but does not indicate that every lattice has transformed into 1T. In the classical definition of sample of MoS_2 is considered 1T, when it possess metallic behavior, which were determine by magnetization or superconductivity measurements.[29] This definition does not require each interstitial site in the lattice to be octehedrally coordinated. Therefore, 1T phase has been determined by XRD and superconductivity measurements to begin at 0.1- 0.2 molar concentration of the guest ion.[29-30] This definition is further supported by the concept of staging. The requirement of staging stipulates that is only possible for ions to be accommodated into particular intervals of the host structure, which is stage II for sodium ions. This fundamental understanding predicts that one sodium atom can be store per one unit cell of 2H-MoS_2, which contains 2 two layers of MoS_2. Whittingham reported the maximum capacity of sodium to be around 0.7 molar amount, which matches well with capacity value and theoretical molar content of sodium (Appendix A.11).[30, 79]

The CV data of an fresh electrode evaluated in window 0.4 - 2.6 V (figure 4.3b) was compared to additional controls such as a MoS_2 electrode, MoS_2-PANI electrode in a deep discharge window (0.05 - 2.6 V), and a MoS_2-PANI electrode with a commonly used electrolyte salt (figure 4.3c). Comparisons between the CV curves of our MoS_2-PANI electrodes with literature (Park), conducted in tetraethylene glycol dimethyl ether (TEGDME) confirm similar oxidation peak potentials and intensities. These similarities suggest that peaks are associated with the redox mechanism of MoS_2 and excludes potential electrolyte decomposition as the primary cause of particular peaks in our EC/DMC electrolyte system.[94]

The appearance of weak shoulders at 2.4 V and elongated shape (hysteresis) between peaks is characteristic the slow oxidation kinetics of sulfide to polysulfides reaction.

The peak's behavior, the continued increase, is consistent with ion insertion into an anode.[92] The peaks at 1.0 V and 0.86 are assign to reversible sodium redox reactions in the 2H-MoS_2 structure. We believe this is the first reported observation of the reversible Na oxidation peak, driving intercalation, for the MoS_2 electrode system.

A broad shoulder appear in the 0.9 V – 1.8 cathodic (sodaition) region during the initial cycle. The following cycles 2 and 5 showed an increasing cathodic (sodaition) peak at ~0.86 V, which suggests increasing quantities of sodium insertion with increasing cycles, as larger amount of the current in each proceeding cycle promote ion movement instead of SEI formation. The confirmation of known MoS_2 features with the addition of the new 1.0 V peak validate the surface sensitivity of our MoS_2-PANI platform. Although we assign the peak increase at 0.86 V to sodiation into the lamella, it has been proposed that some of the inorganic SEI could form in this potential region. Our CV curves do not indicate any additional SEI formation after the 1st cycle.

The potentials at ~2.34 V are associated with longer chain polysulfide formation, which are consistent with the room temperature sodium sulfur battery.[107] The 9th cycle shows one broad cathodic peak at 0.86 corresponding to a similar sized anodic peak, indicating a reversible redox mechanism for sodium and small tail at 0.7 V, denoting that some of MoS_2 was transformed into the 1T structure. The 0.7 V cathodic peak is associated with irreversible structural changes from the semiconductor 2H phase to the metallic 1T phase.[21] As the structure changes to 1T so does band structure, which increase the possibility that electrons can be added to sulfur anti-bonding orbitals. Therefore, the opportunity to form of Na_2S increases. The emergence of the oxidative peaks of 1.34 V and 1.5 V confirm this fundamental understanding. In the 2ndcycle, the same peaks from the initial scan reappear at 0.86 V and 0.7 V, on the cathodic side a shallow cathodic peak at 0.86 could suggest that more electrical energy is driving other reactions. On the anodic side, the peak 1.0 V mirrored the same decline as 0.86 V, but the peaks/shoulders at 1.34 V, 1.5 V and 2.4 showed increases. Additional a reductive peak at 2.24 V emerges in the 10th cycle suggesting a reversible reduction of sulfur and an increase in the overall reversibility of the electrode.

The consistent number of peaks and peak position for both electrodes (continuous cycling and fresh) evaluated at 0.7- 2.6 V confirms that the mechanism remains unaffected if the electrode is aged or uncycled. The dramatic decreases in the anodic peak at 0.94 V between 1st and 2nd cycle can be interpreted as the conventional low-efficiency of the first cycle. With each subsequent cycle, the decline of the 0.94 V peak mirrored in the gradual increase of the other anodic peaks (1.34 – 1.50 V).

The third window provides a critical link to compare CV curves we evaluated under different cycling conditions and CV profiles reported in literature. This window captures most of the reported MoS_2 phenomena with the exception of MoS_2 decomposition at 0.1 V.[20, 22] This window provides the most reliable evidence for redox mechanism as the peaks in the 0.4-2.6 window are consistent for all electrodes we evaluated in this range. Furthermore, our work can be reasonable compared to the pioneering work of Park due similar galvanic battery performance (Appendix A.11-12) and detection of its prominent peaks, despite the use of different electrolytes. Our data shows no unique peaks due to electrolyte decomposition. On the contrary, the CV profiles have shown all peaks can to be consistent the redox mechanism of MoS_2 transformation into sulfides during the first cycle.

Comparisons between the CV profile for ranges 0.4-2.6 V and 0.05-2.6 V show that both regions are dominated by sulfur redox chemistry. If the deep discharge is universally accepted to decompose MoS_2 into sulfides and promote sulfur redox chemistry after the first discharge (reduction of the electrode), then it would be expect that all peaks shown after the reduction would belong to sulfide redox chemistry.[3, 14, 27] Since the CV profile conducted in the 0.4-2.6 and 0.7-2.6 V range, have the same peaks, the data suggest that those peaks must be also attributed to sulfide oxidation and reduction.

Peaks in the 0.4-2.6 window are consistent for all electrode evaluated in this range. Figure 4.9b shows a representative profile at 0.4 -2.6 V. Similar peaks seen in 0.7 V and 0.4 cut-off window for the continuous run clearly emerge in the this window.[3, 14, 27] The biggest difference between this profile and the curves generated in

0.7 window is the loss of the reduction peaks at 0.7 V and ~0.8-0.9 V after the 2nd cycle. This absence of peaks is consistent with CV profile of 0.05 -2.6 V window and confirmed independently by XRD. We agree with Zhu *et al.* that the redox reaction to transform the 2H state into 1T or 1T' state contributes to this peak.[21] Since the trigonal prismatic 2H lattices are initially stacked, we cannot decouple the reaction at the ~0.8-0.9 V peak. For our system, in the 0.4-2.6 window the structural transformation and the removal of coherent stacking occur simultaneously.

Comparisons between voltammograms of 0.4 V cut-off and that of the exfoliated MoS_2 electrode shows clear evidence of increased reversibility for the MoS_2-PANI electrode with a two fold increase in the number of reduction peaks. With an increased number of peaks primarily on the reduction side, oxidation peaks can be paired to form redox couples of 1.35 V & 1.14 V, 1.50 V & 1.38 V, 2.31 V & 2.21 V, and 2.5 & 2.21 V. The reason two oxidation peaks are paired with one reduction peak is due to higher polysulfides chains ability to fragment differently depending where the initial bond is broken. We agree with the conclusions of Fang that the redox couples are associated with sulfur species and not the oxidation and reduction of Mo metal or MoS_2.[3, 33] Mo metal peaks are generally found in the ~1.87 (or 2.1) V region.[108]

4.3.3 The Role of Polyaniline (PANI) in the MoS_2-PANI Composite Electrode

A comparison of the CV profile of exfoliated MoS_2 electrode to those of the MoS_2-PANI composite electrodes show a stark contrast for the absence versus the presence of the PANI conformal coating. In the absence of the conformal coating, there is lack of redox couples of the MoS_2 electrode, which is an indication of irreversible redox reactions. The irreversibility can be contributed to low conductivity of semiconducting 2H phase, formation of an insulating sulfide by-product, and lack of adequate conductivity networks to aid in the transport of ions to the edges of the MoS_2 flakes.[25] When our data is compared to literature where routinely double the amount of carbon black is used (20% vs. our 10%), those electrodes do not show the amount of redox couples indicated in the works, which suggest that the coating does not work simply to increase the "percolation networks".

Additional evidence for the unique (mediator-like) interaction of PANI can be seen when operating under the 0.05-2.6 V window. In this window, the MoS_2 lattice is de-ionized, which would disrupt the conformal coating. Though the coating is disturbed and the environment is high insolating similar to the exfoliated MoS_2 electrode, the PANI that is presence continues to generate more redox couples than electrode without PANI. Therefore, as long as a few molecules of PANI remain active then the redox couples should be present. Sharp peaks of similar magnitudes can be detected in the anodic and cathodic scans supporting the presence of a continuous redox mechanism. A TEM image of the section of the electrode shows the removal of lattice and growing amorphous region in the center of the sheet (Appendix A.13), which is consistent with observations of Xiao.[27] Comparison to between figures 4b & 4d to 4c, which operates under 0.05-2.6, shows consistent peak positions. The redox couple of 1.33 & 1.14 V does not show a continuous increase seen in other PANI electrodes, which can be explained by the loss of lattice that would stabilize the PANI.

Additional proof for sensitivity and potential power of this technique can be seen with the examination of the electrolyte salt $NaClO_4$. Lacey reported less reducing. Here you clearly see the oxidation peak of the intermediated, which provides further proof of surface based interaction. Possible explanations could be that the surface polarity and solubility. Goto reported that $NaPF_6$ salt required more solvent than $NaClO_4$ to be stabilized.[109] Surface polarity can be supported by comparisons between figures 2b and 3b, which 1.0 anodic peak is not seen with 0.4 cut-off. Lacey also suggested that solubility of $NaClO_4$ is a key role in a stable SEI formation in sodium ion battery mechanism.

Our findings suggest that persistent lattices with a PANI coating, which are sufficiently conductive, can act as complexation (non-specific chemical binding) and growth sites for sulfide chains. The shift in peak position with decreasing CV scan rate demonstrates a diffusion controlled process. The lower voltage potentials for the sodium sulfide oxidation and reduction reveal the confinement of the small polysulfide. Once sequestered the species can undergo sustained oxidation and reduction (Appendix A.7). The prolonged redox reaction suggests that this composite material can behave as a redox mediator. This understanding is illustrate in figure 4.7.

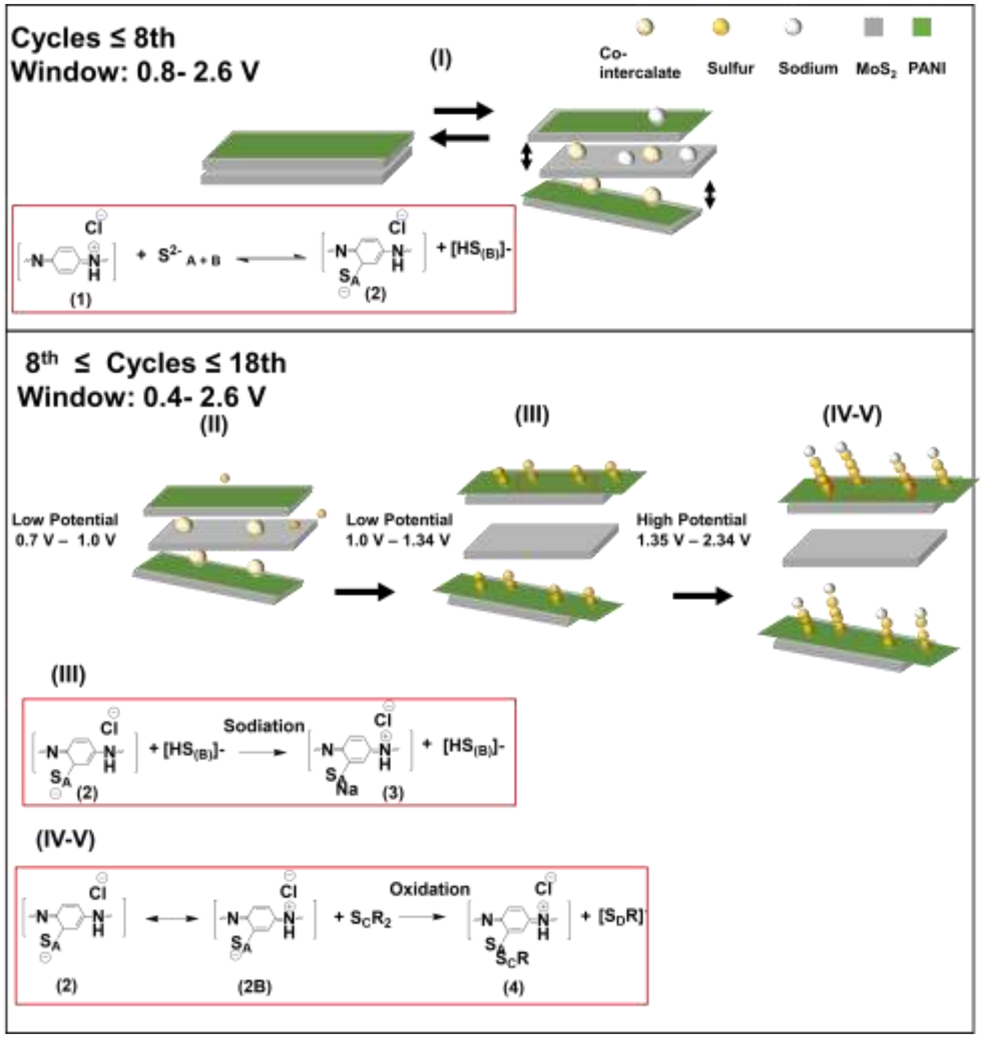

Figure 4.7 Schematic of surface interactions shown with reaction pathway of thiol complexation and/ or attachment to, polymerization, and sodiation around PANI coating. The illustration indicates that initial the insoluble short chain polysulfides remain at the surface on nanostructures within the electrode. However, by lowering the cut voltage or with continued cycling the chain grow becoming soluble and extending of the surface of the structures. For clarity, the quinone imine structure is represented without the other Cl- counter ion and positive charge are not shown.

4.4 Conclusion

In summary, we fabricated a composite sodium-ion anode composed of alternating MoS_2-PANI layers by restacking few-layer MoS_2 with conformal PANI coatings. Additionally, due to the surface sensitive of the composite material, we investigated the role of residual monolayers MoS_2 as possible polysulfide mediators and confirmed the presence of polysulfides in the MoS_2 redox chemistries. Our data suggests that control over cut-off voltages does not eliminated competing conversion reactions. The CV curves of MoS_2-PANI electrode show peaks at the same voltage potentials, although the cut-off voltage is varied from 0.7 V, 0.4 V and 0.05 V. Furthermore, polysulfide peaks indicated that sulfide formation can be initiated at 0.7 V, a region where intercalation was proposed to dominate. We expect that these findings will lead to improve designs for MoS_2 electrodes and better understanding of the redox chemistry at the surface of the electrode.

4.5 Experimental Methods

4.5.1 Materials

Commercial molybdenum disulfide stock powder was purchase from Rose Mill. The powder size was specified as ranging from 3-10 µm. All other materials such as, aniline hydrochloride ⩾ 99%, ammonium persulfate (APS), ethanol, polyvinylfloride (PVDF), sodium hydroxide, hydrochloric acid, N-Methyl-2-pyrrolidone (NMP), and carbon black were purchased and used as-received. Deionized water (Millipore Milli-Q grade) with resistivity of 18.0 MΩ was used for all the experiments.

4.4.2 Stock Powder

To decrease the variability of MoS_2 powder, a more uniform stock of powder of was created by centrifugation. Molybdenum disulfide (3-10µm) raw, as purchased, powder were placed into 50 mL centrifuge tubes with the solvent 45% ethanol/water solution and vortexed for dispersion. The solution could be centrifuge first at 200 rpm for 2-4 minutes. The supernatant could be taken and centrifuge second time at 1500 rpm for 2-4 minutes. The precipitate powder could be vacuum filter or allowed to air-dry. This process was repeated several times to generate enough stock powder.

4.5.3 Exfoliation and Assembly Process

Molybdenum disulfide stock powder was exfoliated in 0.5 mM NaOH 45% ethanol/water (v/v) solution using a Blendtec Blender (speed 5) for one hour.[86] The solution was dialysis against pure water to return to a neutral pH.

The contents of the dialysis bag was emptied into a graduate bottle and ethanol was added to create to approximate a 45% ethanol solution. Aniline hydrochloride was added and the MoS_2 flakes were incubated in 45% ethanol aniline hydrochloride for one hour. Upon incubation, the aniline monomer was polymerized using ammonium persulfate as the oxidant overnight.[110] The MoS_2-PANI hybrid material was collected by centrifugation and washed by ~ 80mL of ethanol. The composite is air dried in a plastic weigh boat to approximate the mass.

4.5.4 Slurry Coating

The MoS_2-PANI was transferred to a mortar to create a slurry. Electrodes were prepared using a doctor-blade to coat the slurry onto alumina foil. The battery slurry was constructed by mixing the MoS_2-PANI composite, polyvinylfloride (PVDF), and carbon black (80:10:10 by weight) by hand in a mortar and pestle. NMP was added dropwise to create a viscous slurry. Finally, with the addition of heat and acid the hybrid material was restacked by the electrostatic interactions, which decreased the interfacial instability.[18] The hybrid material was restacked with HCl (30µL, 12 M) and heated in the oven 90 ºC for 20 minutes. The addition of acid helps at aligning flakes.[84] The slurry was spread on to alumina using the blade method, dried at 105 ºC overnight in a vacuum oven. Electrodes were prepared by punching MoS_2-PANI anode using a ¼ inch hole punch.

4.5.5 Characterization

Galvanostatic measurements were carried out on the Arbin tester and the cyclic voltammery (CV) tests were conducted on the Bio-logic system. The cycled and uncycled MoS_2-PANI anode was imaged using a Hitachi SU-70 Schottky field emission gun Scanning Electron Microscope (FEG-SEM) and a JEOL FEG Transmission Electron Microscope (TEM). TEM samples were prepared and drop-casted on 300 mesh copper grids covered with carbon film. XRD characterization was conducted on Bruker C2/D8 Discover powder diffractometer.

Chapter 5: Micelle-Templated LLZO Garnet Growth

5.1 **Introduction**

With the push towards wearable electronics, development of foldable phones, and the rise of mobile connected devices such as smart watches, smart glasses, etc. (*e.g.* the Internet of Things) to monitor individuals and daily life, the batteries for the future may have very different roles and requirements than current batteries and the batteries of the past. The next generation of batteries devices will continue to evolve to meet the needs of consumers and designs of emerging electronic devices.

One strategy for devising batteries for the future is the creation of high voltage and high energy density batteries. These batteries must meet fundamentally different requirements than current lithium ion batteries devices such as increased safety, a wide electrochemical stability window, processing and mechanical strength. For safety reasons, these batteries are predicted to be fully composed of solid materials, which is classified as an all solid-state battery. In order to build an all solid-state, a suitable replacement for the liquid electrolyte is needed. This substitution will allow for an increase in capacity and charging speed, which is currently limited by safety concerns of approaching the reduction and oxidation potentials of liquid electrolyte.

Replacing a liquid electrolyte with a solid is not trivial, as solids have well defined interfaces, higher resistances, and, generally, slower ion permeability (kinetics) than liquids. LLZO is a class of potential candidates to be used as solid-state electrolytes. LLZO contains lithium, lanthanum zirconium and sometimes an additional metal dopant. In 2007, Murugan *et al.* first reported garnet typed LLZO with a formula of $Li_7La_3Zr_2O_{12}$ as a promising solid-state electrolyte with a high bulk ionic conductivity of (~$10^{-3} - 10^{-4}$ S cm^{-1}) at 25°C.[36] LLZO meets the requirements for future battery devices because of its excellence thermal stability, mechanical strength and broad voltage window, coupled with high bulk conductivity and non-flammability.[37]

Although these material meets critical prerequisites to be a viable candidate for future devices, further research is needed to overcome the material's flaws. The flaws originating from the composition and properties of the LLZO materials and problems associated with the fabrication and processing method of the LLZO material. LLZO is conventionally unstable at room temperature in air and requires energy and time consuming preparation processes (*e.g.* temperatures around ~1100 °C and annealing times around 20 hours). In air, LLZO reacts with CO_2 to form Li_2CO_3, which decomposes the cubic phase garnet-type LLZO (c-LLZO) into a tetragonal phase (t-LLZO).[111] The combined formation of Li_2CO_3 and t-LLZO lead to a Li-ion conductive material, in which the exposed interfaces are especially highly resistive.[111-113]

The LLZO fabrication also suffers from low preparation efficiency and variable batch quality as the general synthetic routes form mixtures of the desire cubic garnet type LLZO with low ion conducting or insulating competing phases (*e.g*. t-LLZO, Li_2CO_3, $Li_2Zr_2O_3$, and $La_2Zr_2O_3$).[37] The fabrication procedures attempts to strike a balance between long synthesis times to allow atoms to diffuse their appropriate lattice position and complete the alloying reactions, high temperatures required high to melt reagents and format the desired c-LLZO energy, while preventing Li loss, which promote competitive phases to form.

Researchers have found methods to stabilize the structure using multivalent ions such as Al^{3+}, Ga^{3+}, Ta^{5+}, Nb^{5+} as dopants.[37, 112] The addition of the dopant ions have correlated with increased conductivity and improving stability, though their use may decrease the number sites for Li occupancy. Aluminum is the most common dopant and in addition to stabilizing the structure, the formation or use of Al_2O_3 as a reagent is proposed to migrate to the surface and to have significant concentrations at grain boundaries preventing the formation of Li_2CO_3. Al doped LLZO is also highly practical as alumina crucible are some of the most used containers for LLZO synthesis. In order to prevent Al diffusion from the crucible and to maintain strict dopant content, platinum crucibles are required.

One innovated solution to improve fabrication process is by the creation of small uniform garnet crystals to capitalize on the advantages report from the small LLZO particles. The creation of small LLZO particles can lead to lower calcination temperature and faster diffusion of ions to their lattice positions. Wolfenstine observed an improvement in conductivity of LLZO due to smaller grain sizes and large concentration of grain boundaries. Additionally, Wolfenstine reported that smaller grains lead to more stable in air, forming less Li_2CO_3.[114-115] Kun demonstrated an electrospun nano-structured LLZO system with 250 nm fibers and a conductivity of 2.5×10^{-4} S/cm.[116]

We focus on the fabrication of nano-structured LLZO as a method to improve conductivity and reduce the impact of the fabrication process. Though electrospinning is one of the prominent examples of LLZO nano-structuring, it is not easy to control and does not represent a facile method. For the best results, a dedicated set-up and humidity environment is needed. Still however, the results seem to be variable compounded the already poor fabrication efficiency of LLZO material. Figure 5.1 shows a survey of the some of the LLZO products with images of the calcined result.

Although each structure began from the same electrospinning solution and the heat process only differs by a few degrees, the morphologies are distinctly different. As the precursor was sintered, frequently the features and grains have merged, which removed the potential benefits of nano-structuring and fiber alignment. This same merging phenomenon can be seen in similar nanostructure garnet works.[117] To maximize the benefits of nano-structuring a methodology should maintain their initial morphology, structure, or reduce the possibility for features to merge.

We propose to fabricate nanostructured garnet using reverse micelle (water-in-oil) templates, which can sequester the precursor salt solution inside the core. As the micelle template undergoes the calcination process, solid-state reactions occur in the core while the polystyrene shell is carbonized. Using a reverse micelle templated growth strategy, it is not only possible to grow unique morphologies and a sample with grains of a consistent size and shape, but to tune morphologies by changing the ratio of the lengths of the polymer blocks.

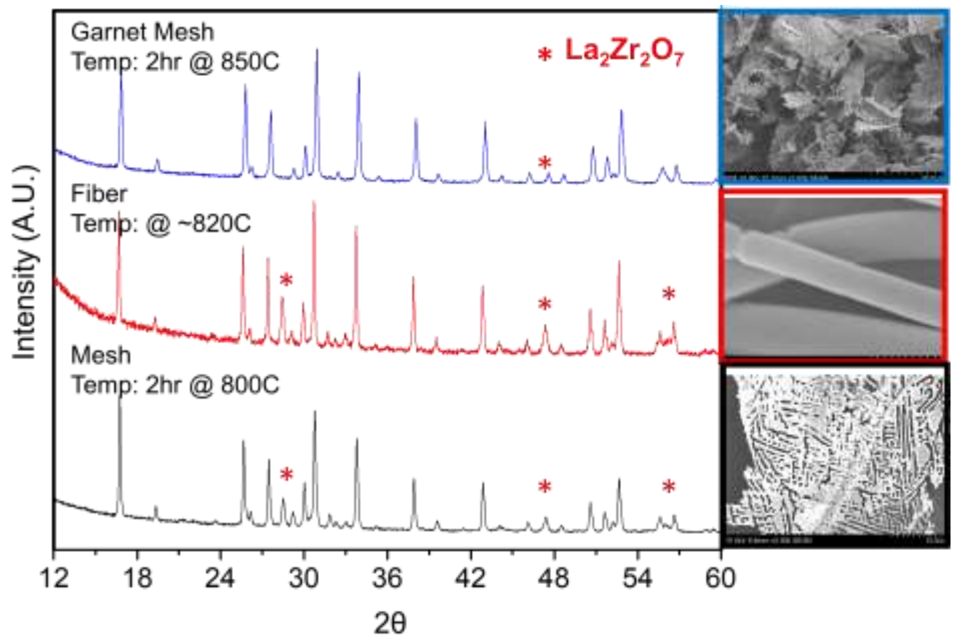

Figure 5.1. Comparisons of XRD spectra, morphologies, and calcination temperatures of garnet nanostructured by electrospinning.

5.2 Results

In the following, we systematically investigate the growth parameters of a novel fabrication approach to nano-structure a solid-state electrolyte material. We anticipate some unique and potentially groundbreaking possibilities to control morphology through the development of a one-step calcination/sintering process for garnet materials. This chapter will focus on two polymer compositions, and elucidating the experimental parameters that influence the synthesis of high quality $Li_7La_3Zr_2O_{12}$ garnet. We utilized two poly(styrene)-block-poly(acrylic acid) (PS-b-PAA) polymers with molecular weight (Mn) of 36,000. One polymer had a composition of ~70% PAA (PS(0.3)-b-PAA(0.7). and the other, a commercially available polymer, had a composition of ~20% PAA (PS(0.8)-b-PAA(0.2)). For the two polymer systems, we examined the effect of two key growth parameters, temperature and excess lithium content, on the garnet crystal structure. Figure 5.2 illustrates the reverse-micelle template strategy.

As the schematic illustrates, the general procedure to fabricate the garnet-type LLZO product was to initiate reverse-micellization with relevant garnet LLZO salts followed by drying in vacuum chamber at room temperature and calcination of the templated-precursor at 750 °C in air for 5 hours. The micellization process was modified from the procedure developed and reported by Jiang *et al.*[118] The process does not involve dialysis and solvent evaporation traditionally used for this process. Instead, the process uses the addition of a selective solvent, which is unfavorable to one polymer segment, to induce the micellization of the block copolymer. In this case, the PAA segment becomes less solvated with increasing toluene content while the solvation of the hydrophobic PS block increases. The solvent ratio is critical to this method; therefore, Jiang concluded that the favorable solvent should be limited to 10% v/v or less to generate the smallest micelles and the narrowest distribution.

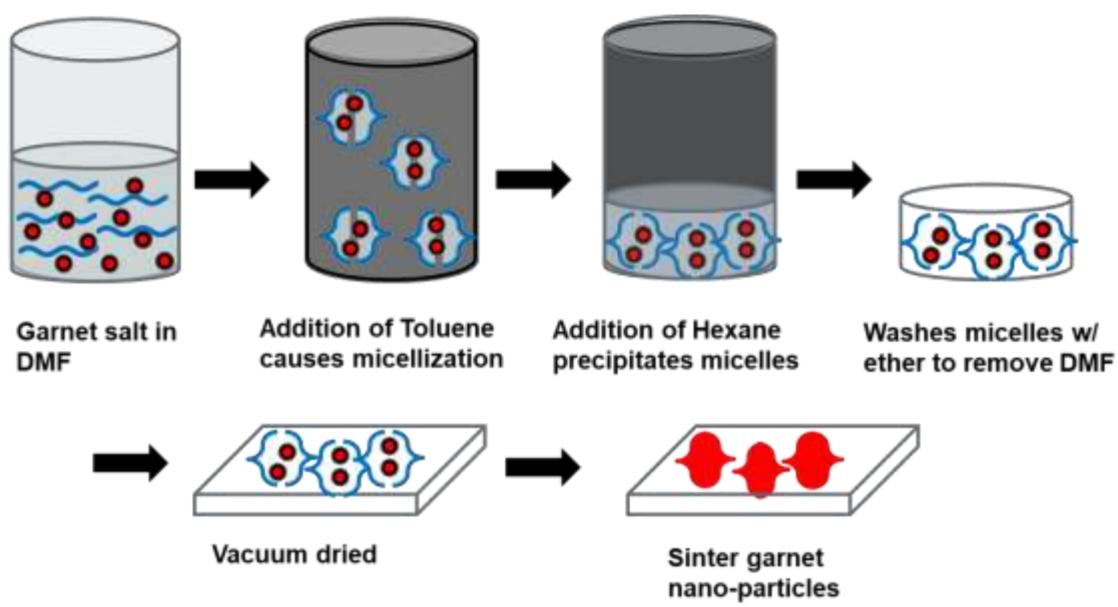

Figure 5.2. A schematic illustration of micelle-template growth process.

When the final solvent composition is reached, polymer will be "frozen" in this form and ready for the calcination step. For our system, the hydrophobic and salt sequestered within the micelle while the PS segment forms the shell. To maintain the micelle structure the leftover solvent must be removed quickly and heat should be avoided to prevent the polymer from re-dissolving in any remaining favorable solvent.

5.3.1 Temperature and Li Content Effect on Garnet Crystal Structure

To understand the growth process and determine the optimal synthesis conditions, the temperature and excess Li content were investigated. Figure 5.3 show crystal structure changes as the calcination temperature is changed for the (PS(0.3)-b-PAA(0.7) system. The optimal conditions were found to be an excess of 60% lithium content and 5 hour calcination (annealing) time. Characteristic garnet peaks are not seen until reaching 750 °C, which is consistent with literature. At 850 the XRD spectra, looks relatively similar, however, the first peak of $La_2Zr_2O_3$ at 28 degrees appears to be growing larger than the peak under 750 °C conditions.

To better understand the growth process and the emergence of various impurities as micelle-template is carbonized, a calcination step was set for two hours of the start of the calcination process, roughly midpoint of the process (Figure 5.3). The sample was removed at approximated 227 °C after about 2 total hours. The spectra has a very close agreement to that of a lithium rich zirconium phase $Li_2Zr_2O_3$.

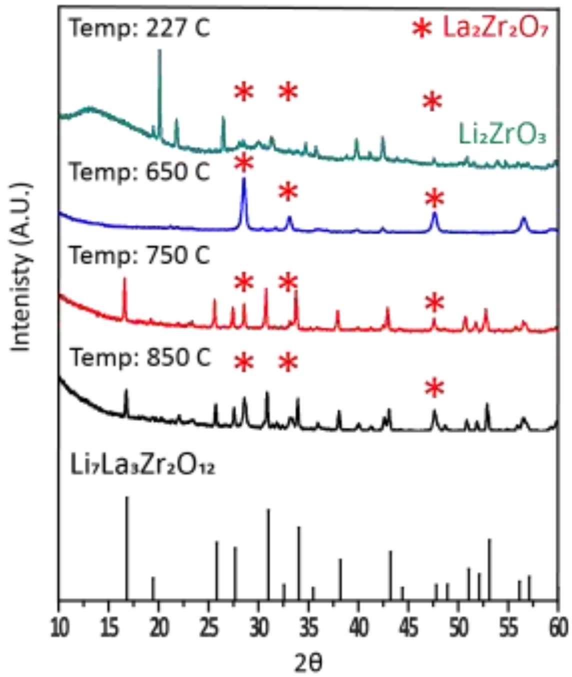

Figure 5.3. Comparison of garnet quality at varying calcine temperatures with 60 wt.% excess Li for the PS(0.3)-b-PAA(0.7). (PDF) of $Li_7La_3Zr_2O_{12}$. The $La_2Zr_2O_3$ phase is indicated by (*).

Similar evaluations were conducted with the PS(0.8)-b-PAA(0.2)) system. The optimal temperature was again found to be at 750 C. Nevertheless, a greater amount of excess lithium was required than the previous system. When a precursor with a 65% Li content was calcinated at the optimized temperature no $La_2Zr_2O_7$ peaks were seen.

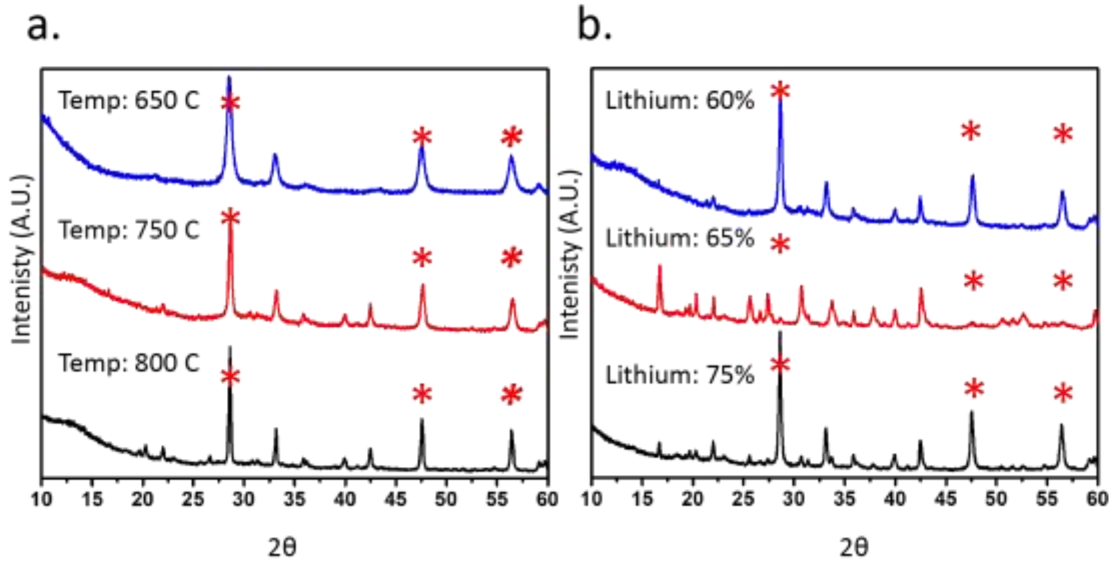

Figure 5.4. XRD comparisons after different synthesis parameters. a) varying calcine temperatures with 60 wt.% excess Li composition b) varying excess Li content with a calcine temperature of 750 C. The $La_2Zr_2O_3$ phase is indicated by (*).

5.3.2 Evaluation of Reverse Micelles Structure and Precursor Encapsulation

During the optimization, clear distinctions could be seen between the polymer systems. The cohesive ability and symmetric shrinking during the calcine process, seen in figure 5.5 for the PS(0.3)-b-PAA(0.7) system, leads to the consideration of attempting to form a one-step garnet pellet fabrication approach. To understand the differences and to confirm the presence particularly that of the zirconium (IV) oxynitrate salt, which is difficult to dissolve, within the micelles, the micelle templates were characterized by SEM with Energy-dispersive X-ray spectroscopy (EDX). The SEM micrographs shows variation of micelles for the two systems. The commercially purchase polymer shows uniform distribution of micelles of 200 nm and the PS(0.3)-b-PAA(0.7) shows a few micelles around the size but also contains a number of vesicles with dimension in the micron scale (Appendix A.14.). The EDX mapping displays the localization of zirconium and nitrogen within the polymer templates.

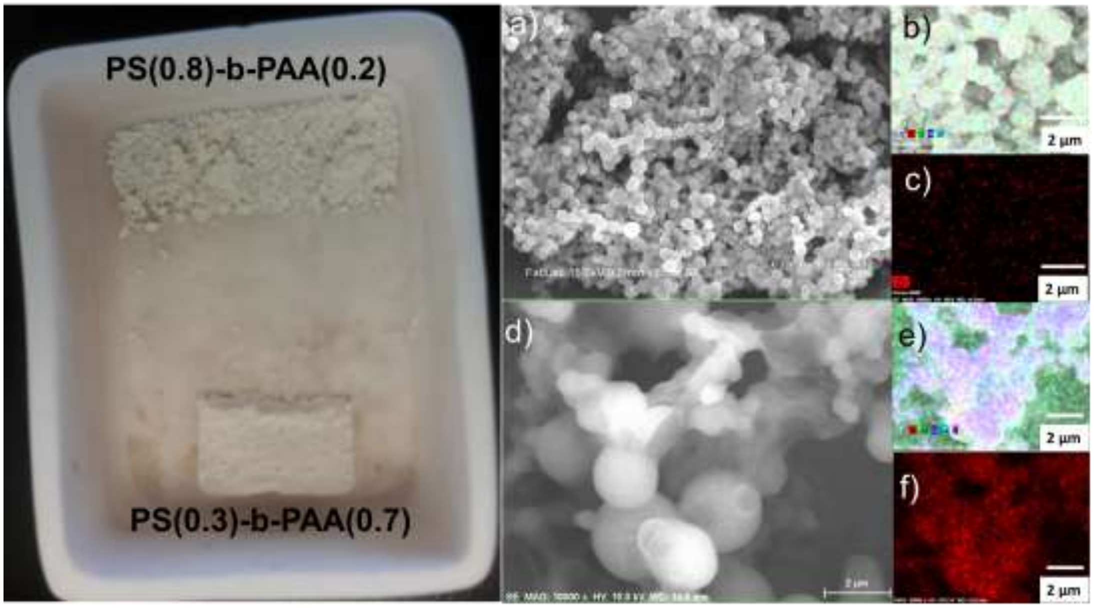

Figure 5.5. The first image (left) represents a comparison of the garnet formed under the same 750 °C for ~5hrs for the two polymer systems with a-c corresponding to PS(0.8)-b-PAA(0.2) and d-f corresponding to PS(0.3)-b-PAA(0.7). SEM image of approximately range of micelle and vesicles with EDX elemental mapping identifying localized presence of b&e) an assortment of atoms corresponding to the precursor salts c&f) zirconium

5.3.3 Micelle Drying Optimization

Upon achieving quality garnet, it is important to evaluate the nano-structuring of the grains, figure 4.6. While PS(0.8)-b-PAA(0.2) dries quickly in the vacuum leaving behind powder or small flakes, the micelles formed of PS(0.3)-b-PAA(0.7) require longer to dry. The longer drying time can be contributed to increased length of the PAA section and the presence of vesicles. This hydrophilic property causes drying to have a considerable influence on garnet grains.

After the precursor solution was dried for 3 days, the solution dried into a gel-like state. There was no visible moisture and no moisture detected when blotted with a Kimwipe. After the structure was calcinated, the product had an abstract shape, but no visible grains. The transformation from a blob-like shape to a smooth shape suggested that the micelle-template had to ability to shape-transform when calcined. To test the influence of the moisture content (drying duration) had over the morphology of product, an additional sample was made from same batch and was dried over several weeks then calcined into a powder. The further dried product showed uniform grains, using the same calcination parameters.

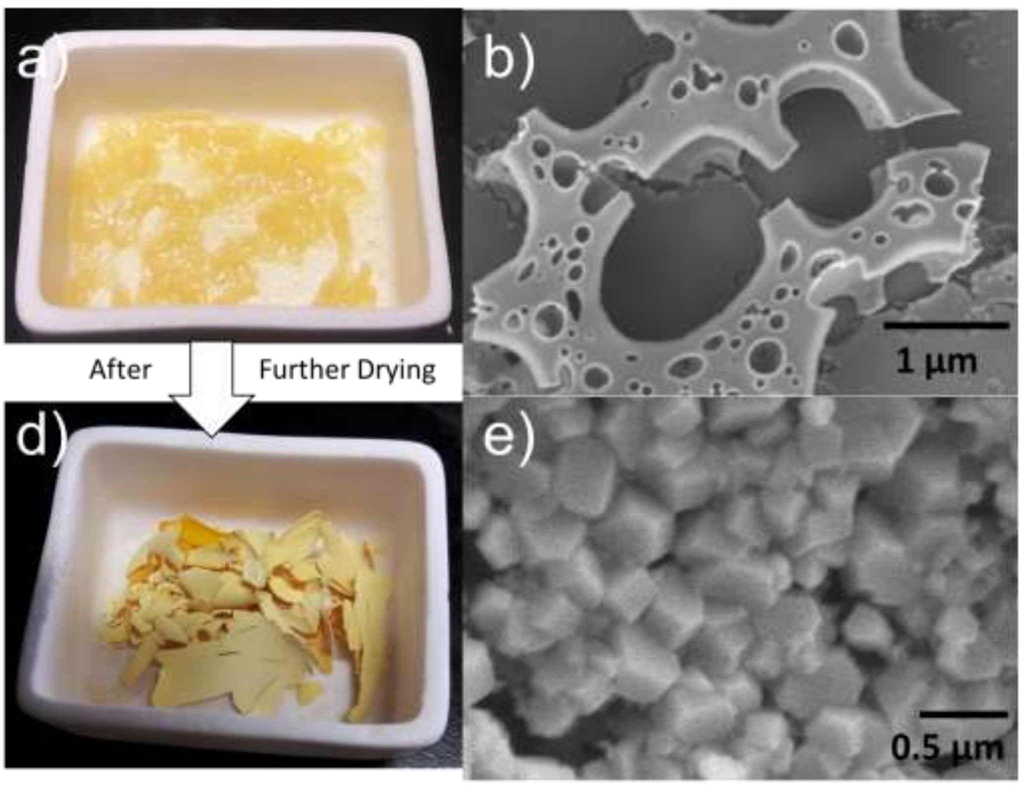

Figure 5.6. Photos of the differences between a) the moisture containing and b) further dried micelle-templates. The corresponding SEM images of the morphology differences after calcining between a) the moisture containing and b) further dried reverse-micelle. Reverse-micelles were created using PS(0.3)-b-PAA(0.7) laboratory synthesize.

5.3.4 Evaluating the Versatility of the Micelle Growth Process

To evaluate the conductivity of the nanostructure garnet, it is essential to form a high quality garnet pellet. The ability to combine the calcine and sintering step into a one-step procedure would increase the possibility to create high throughput nano-structured garnet pellets. We demonstrated the ability for the precursor to be molded then annealed into a pellet with nano-sized grains, which confirm the possibility of combining the steps. However, further optimization is needed to improve the conductivity. The results of the two pellets created through this process are shown in figures 5.7 and 5.10. Figure 5.7 displays a pellet with a smooth surface fabricated from the PS(0.8)-b-PAA(0.2) system unlike the rough surface seen in figure 5.10. The pellet created in the 1-step process was annealed at 1110 °C a standard temperature sintering temperature reported in literature.[119] The aim was to determine if the pellet could withstand high temperature and maintain the nanoscale features.

The PS(0.3)-b-PAA(0.7) was shown to create an uniform distribution of ~500 nm grains (figure 5.6e). We chose to explore the PS(0.8)-b-PAA(0.2) system due to its advantages of lack of vesicles and better micelle uniformity (figure 5.5a-d). To test the 1-step process, the dried powder composed of the precursor salts sequestered in the reverse micelles were pressed into a 10 mm pellet then annealed to 1100 °C at a ramp rate of 2.5 C/min. The SEM image of cross-section of the pellet displays uniform grains, which resemble the grain morphologies of the electrospun garnet systems (figure 5.7). However, the XRD spectra reveals that the pellet is largely composed of a Li_2CO_4 (zabuyelite) phase. Our early Rietveld refinement models estimate that the phase is approximately 30%. We evaluated a modified two-step calcination and sinter procedure using powder calcined at 650 °C and a sintering temperature around ~850 °C for 5 hours for the PS(0.8)-b-PAA(0.2) system, which also led to a mechanically strong, but non-conducting pellet. Figure 5.7 displays the XRD spectra the after sintering process, which was phase matched to be largely composed of many of the competitive garnet phases such as t-LLZO, Li_2CO_3, $Li_2Zr_2O_3$, and $La_2Zr_2O_3$. The amplitude of peak indicating the $La_2Zr_2O_3$ phase is small in comparison to characteristic XRD spectra of calcine c-LLZO products, which suggest the alloying reaction was near completion or fully complete. A lower La_2Zr_2O content typically coincides with greater amounts of the c-LLZO phase. The presence of additional peaks and lower amplitudes of c-LLZO peaks suggests that the low-temperature nanostructured garnet was dependent on the annealing time and the sintering process promoted the degradation of the cubic garnet crystal. The presence of the Li_2CO_3 peaks is significant, as it was not seen in the calcinated garnet powder.

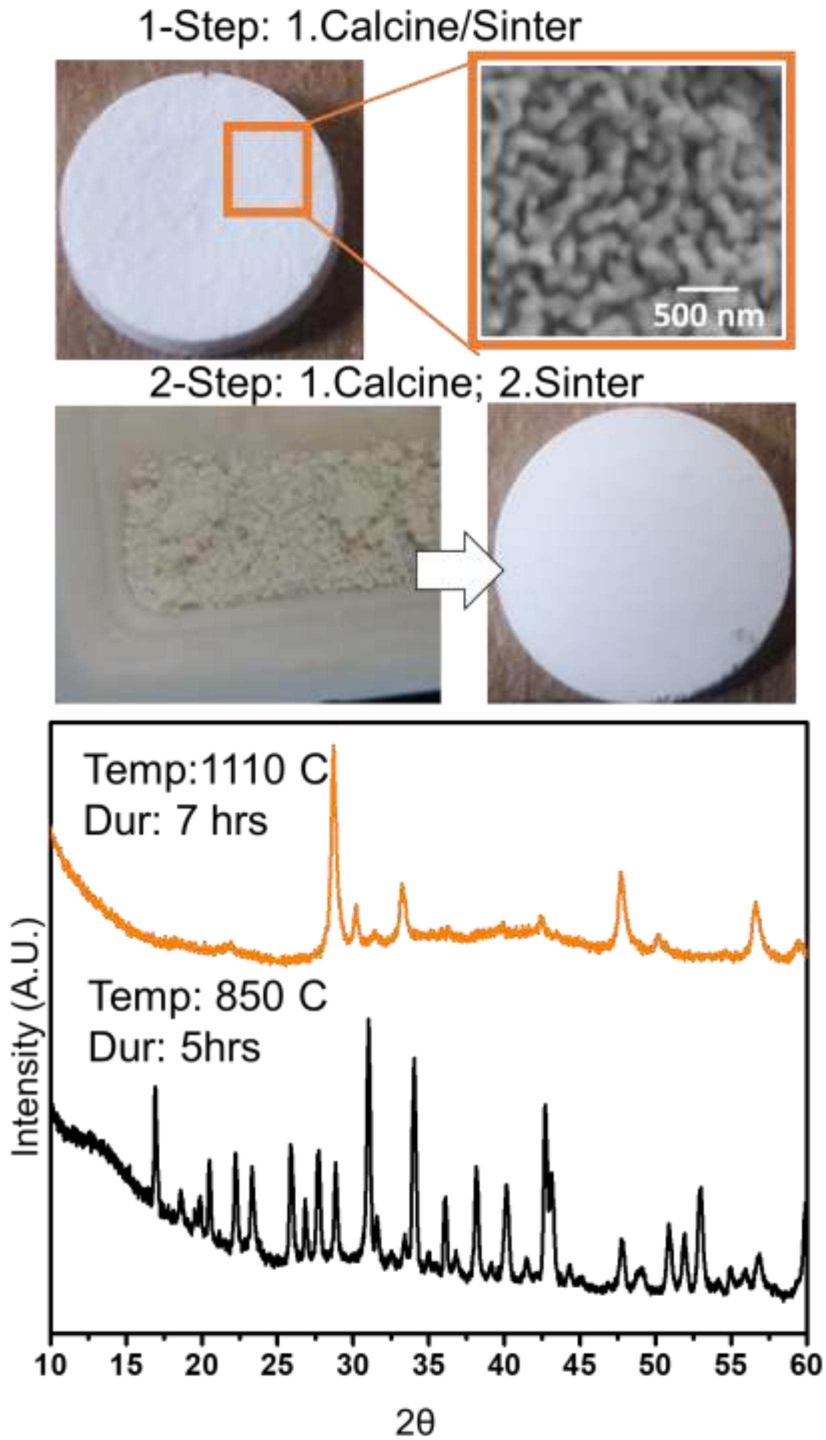

Figure 5.7. The diagram composed of images, SEM micrograms, and XRD spectra illustrates the procedures to places nano-scale features into sinter pellets. The top of the image and spectra correspond to a combined annealing step, and the bottom images and spectra correspond to a two-step annealing process each using PS(0.8)-b-PAA(0.2) polymer.

To investigate the degradation that occurs with increased annealing temperature, the optimal calcine duration was extended to 9 and 12 hours (figure 5.8). With the extended time, the spectra began to resemble that of the sintered pellet, showing increasing mixtures of t-LLZO, $Li_2Zr_2O_3$, and Li_2CO phases. The 5 hour spectra is characteristic of the quality of garnet produced by the reverse micelle method where peaks of c-LLZO are intermixed with peaks at 47 and 58 degrees, indicating the presence of a $La_2Zr_2O_3$ phase. As the calcination time was extended to 9 and 12 hours, the presence of the $La_2Zr_2O_3$ phase was removed and other peaks emerged in the 15-22 2θ degree range. After 9 hours, a large peak at 21 degrees appeared which is characteristic of a Li_2CO_3 phase.

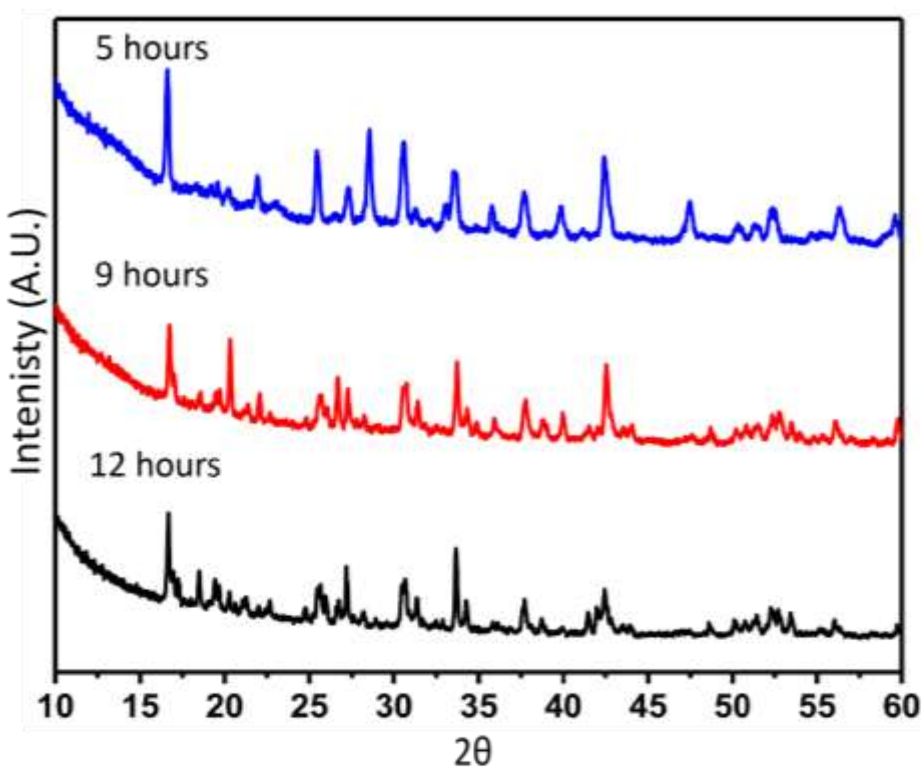

Figure 5.8. Comparison of XRD spectra of LLZO products at varying annealing times, where the batch, mass, temperatures, and polymer system (PS(0.8)-b-PAA(0.2)) are constants.

A more standard two-step process was implemented where garnet was initially formed using a fast calcination process at the optimal (750 C) temperature for the PS(0.3)-b-PAA(0.7) system and sintered under the optimal annealing procedure. The XRD spectra of the pellet was analyzed using the phase matching software EVA 5 and refined using TOPAS 4.2 to quantify the composition of the pellet in order to determine the causes of the low conductivity (figure 5.8). We chose to refine this product as the PS(0.3)-b-PAA(0.7) system has a smaller styrene shell, which may have contributed to the amount of Li_2CO_3 formed during the sintering process. Using the XRD spectra of samples stored for months in capped bottles or in a vacuum chamber, we determined that the calcined nano-structured garnet created through the micelle method was very stable against air during the XRD analysis, transport, sample preparation, and sample storage (Appendix A.14). Figure 5.9 shows the fitted spectrum for the refinement. The estimated compositions after the Rietveld refinement was 30% c-LLZO garnet-type, 30% Li_2CO_3 (Zabuyelite), ~37% Li_2ZrO_3 and 3% ZrO_2 (Baddelyeyite) (Appendix A.15).

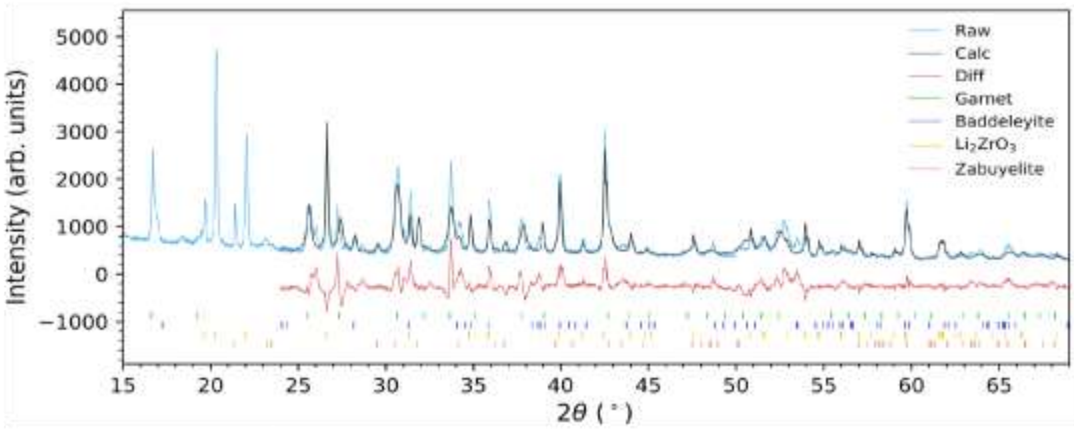

Figure 5.9. Representative refinement of an ex-situ X-ray powder diffraction pattern for calcined and sintered LLZO product. Shown are the observed (light blue), calculated (black line), and difference (red). Tick marks indicate the positions of allowed reflections for various phases. Baddelyeyite and zabuyelite are the mineral names of ZrO_2 and Li_2CO_3, respectively. Garnet represents the $Li_7La_3Zr_2O_{12}$ phase and Ia-3d space group.

The sintering of the powders that were calcinated at 650 °C (PS(0.8)-b-PAA(0.2)) and at 750 °C (PS(0.3)-b-PAA(0.7)) resulted in pellets with significant peaks from competitive phases (figures 5.7 and 5.9). The destabilization is consistent with recent reports of size-dependent phase transformations in which the process of sintering calcined c-LLZO electrospun fibers and ball-milled particles caused garnet powder to agglomerate.[117] Chan *et al.* proposed that the agglomerated pieces have a preference for forming the t-LLZO, while nano-sized particle are stabilized by the cubic structural arrangement.[117] While we could not confirmation the transition to t-LLZO phase for powders annealed for 9 and 12 hours, the pellet sinter with a 2-step process at 850 °C does show characteristic peaks of t-LLZO phase (figure 5.7).

Our final study involved determining the polymers ability to infuse pellets with morphologies dictated by controlling the polymer parameters. The pellet was created using a combined calcination/sintered procedure. Figure 5.10 displays a pellet with a rough surface unlike the pellets formed from the PS(0.8)-b-PAA(0.2) polymer in figure 5.7. The lab synthesized polymer of ~40K Mn PS(0.92)-b- PAA(0.08) was used to create the pellet. The pattern on the surface was similar to that seen of the vacuum dried precursor. SEM characterization revealed the surface was composed entirely of loops with diameters approximate 2µm, on average. The crack in the pellet seen in figure 5.10 could be a result of the nano-features or the high impurities within the pellet.

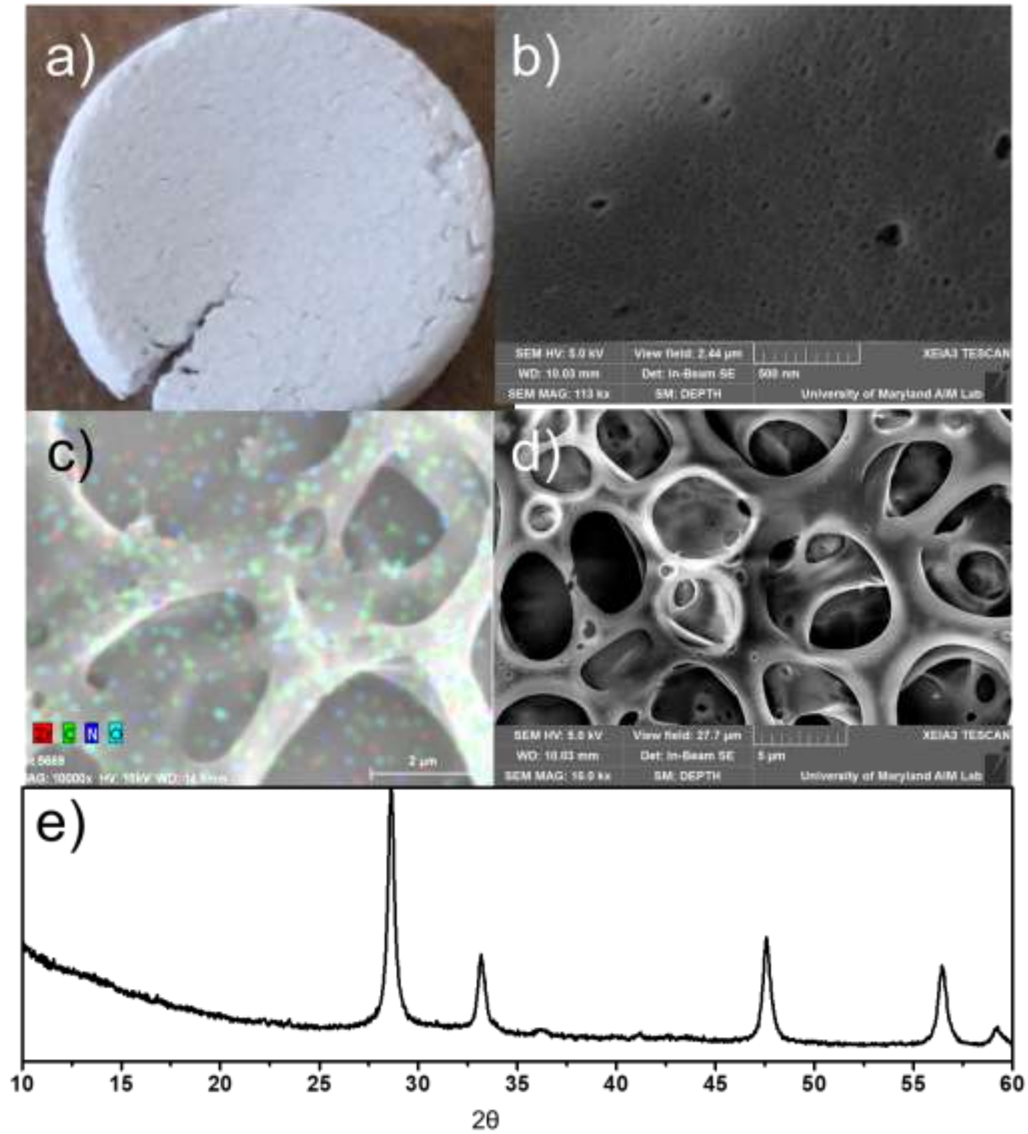

Figure 5.10. a) Photo of the calcined/sinter product from the pressed 10 mm pellet and corresponding SEM images b) wide shot c) EDX elemental mapping and d) zoomed reverse-micelle was created using 40K Mn PS(0.92)-b- PAA(0.08). e) XRD spectra from the pellet.

5.3 Discussion

Through our *ex situ* XRD experiments, we developed the parameters for our reverse micelle method to create high quality garnet. The optimal temperature was determined to be around 750 °C for each polymer system, which is consistent with that of other reported low-temperature LLZO synthesis methods.[120] The lithium content and calcination times were notable different. The lithium content for the PS(0.3)-b-PAA(0.7) and PS(0.8)-b-PAA(0.2) were found to be 60 wt.% and 65 wt.% excess lithium salt, respectively. A possible explanation for the differences in salt content could originate from differences between the polymer systems such as the number of PAA monomers or a higher population of longer polymer chains. The length of the PAA segments could contribute to the difference through a combination of sequestering more of initial DMF solvent and lithium salt with the increased hydrogen bonding. Trapped DMF solvent could aid in the retention of more lithium ions and after a diethyl ether wash, allow PS(0.3)-b-PAA(0.7) to require less excess lithium than the PS(0.8)-b-PAA(0.2) system. An alternate hypothesis is that the additional 5% lithium content matches the population of higher molecular weight polymers for the PS(0.8)-b-PAA(0.2) system. The amount of diethyl ether used is approximately half of the initial volume of DMF used. The diethyl ether wash was needed to maintain the micelle structure when heating. If larger amounts of DMF solvent remain, the micelles could possibly re-dissolve during the sintering process, which could lead to the morphology seen in figure 5.6b. Additionally, the formation of nano-sized garnet-type LLZO could promote faster lithium loss during the annealing process.

In general, it is known that the annealing procedure was to be based on the reagents used. The reagents used in this study were similar to that published by Goodenough *et al.* for their low-temperature garnet synthesis. The article reported that the garnet quality was independent of heating time at the optimized temperature and that first detection of the onset of the cubic type peaks occurred 4 hours.[120] To the contrary, our findings suggest that ~4 hours for the total calcination time is sufficient to produce c-LLZO, but the quality of the c-LLZO product could vary depending on the mass of the sample (Appendix A.16). Therefore, a standard 5 hours calcination time was followed for both systems with a sample mass of 300 mg (Appendix A.17). For our method, the minimum time for significant amounts of c-LLZO was found to be 3 hours.

Though the lithium content changed for this system, the growth was consistent. Using TGA, Xie reported that melting of zirconium and lithium salts occurred first below 400 C. Our data shows the emergence of the $Li_2Zr_2O_3$ phase occurs first, followed by the $La_2Zr_2O_7$ phase and finally the formation of the cubic garnet-type (c-LLZO) phase, which with increased heating transformed into the tetrahedral garnet type (t-LLZO) phase. Despite the existence of garnet-type phases at 650 °C and 850 °C, the $La_2Zr_2O_7$ phase appears dominant at both temperatures. Xie proposed that the dominance of this phase at the lower temperature was due to an incomplete alloying reaction and at higher temperatures due to the continuing removal of lithium leaving behind large amounts of $La_2Zr_2O_7$.[120]

Controlling for the parameters (*i.e.* drying, lithium content, and calcine temperature), we selected the commercial polymer, PS(0.8)-b-PAA(0.2), to evaluate the ability to make high quality garnet pellets. We evaluated two synthetic routes: a combined calcine/sinter step and a more conventional two-step calcine and sintering approach. With both routes, XRD analysis revealed that the pellets contained mixtures of other phases. Neither route produced a high quality garnet pellet. Therefore, no impedance data was shown as the presence of substantial amounts of competitive phase will lead to highly resistivity pellets. None of the pellets created using a combined calcine/sinter step lead to a garnet phase. Creating a pellet from garnet powder also led to a pellet with multiphase peaks or a pellet that quickly released Li content leading to $La_2Zr_2O_7$. A second pellet made from powder calcined under the conditions of 65% lithium excess and 750 °C and sintered at 850 °C lead to a multiphase pellet containing peaks of cubic garnet, $Li_2Zr_2O_3$ and Li_2CO_3.

5.4 **Conclusion**

We have systematically investigate the growth parameters of a novel fabrication process especially tailored toward nano-structuring of solid-state materials. We determined that the optimal synthesis conditions are at calcination temperature of 750 °C, ~4 h heating duration and a salt content of 60 wt.% and 65 wt.% excess lithium, for the PS(0.3)-b-PAA(0.7) and PS(0.8)-b-PAA(0.2 polymer systems, respectively. These conditions were used to produce high quality $Li_7La_3Zr_2O_{12}$ powder that was stable against air exposure and has demonstrated excellence stability when stored at room temperature for months. We believe the true potential of the reverse-micelle method lies in the versatility to be pair with a various polymer systems and solvents and the ability to fabricate nano-structured grains within the garnets pellets.

For a large scale production of nano-structured garnet, ball-milling must be removed from the standard garnet fabrication method. We demonstrated the ability to incorporate nano-structuring with a garnet pellet using a combine one-step calcination and sintering method or a modified two-step method. Although the sintering process requires more refinement in order to improve the conductivity, we have shown the ability to infuse two morphologies within a pellet, grains of 500 nm and 2uM loops. We suggest that one of the possible reasons for the low conductivity is due a decomposition of the more conductivity, cubic LLZO (c-LLZO), phase as a result of the agglomeration of our nano-size features into bigger pieces during the sintering process. This size change leads to a partial phase change within the pellets from a c-LLZO to other competitive phases. This structural and compositional change is consistent with a phenomenon of size-dependent transition, which was first report by Chan *et al*.[117] In addition to the size-dependent transition, it is widely known that the destabilization of the c-LLZO phase promotes formation of t-LLZO. The general cause of this destabilization is the loss of lithium, which leads to vacancies within the lattice and promotes the growth of competitive phases such as $La_2Zr_2O_7$ and t-LLZO during annealing. Therefore, at particular lithium content, the t-LLZO phase has a higher thermodynamic stability in contrast to the cubic phase. Since the composition and/or occupancy of lithium interstitial sites are important factors in the stability, the use of dopants or increasing the lithium content can suppress the t-LLZO formation. These strategies to promote c-LLZO phase even at high temperatures and extended annealing times.

We refined the XRD structure to quantify the phases within the pellet and determined that the pellet is composited of about 30% c-LLZO phase. We believe that obtaining c-LLZO nanostructured pellet still remains a possibility, but is a matter of kinetic sintering control.

5.5 **Experimental Methods**

5.5.1 Materials

The starting materials were $LiNO_3$ (99%, Sigma Aldrich), $La(NO_3)_3$ (99.9%, Sigma Aldrich), $ZrO(NO_3)_2$ (99.9%, Sigma Aldrich), Poly(styrene)-block-poly(acrylic acid) 38K, and Al_2O_3 (99.99%, Sigma Aldrich. For the electrospun fibers, the garnet salts were first dissolve in the acetic acid starting with zircounium oxynitrate first, due to its high insolubility. In a separate container, the polymer was dissolve first in Dimethylformamide (DMF) followed by any additional salts not added to the acetic acid then the two solution were combined into 1:1 ratio creating the garnet salt precursor solution. For the micelle-template, stoichiometric amounts of the inorganic salts chemicals were dissolved in the DMF and excess lithium was added. For both processes excess $LiNO_3$ was added to compensate for lithium loss during the calcination.

5.5.2 Electrospinning

Stoichiometric amounts of salts and excess lithium, and PVP were dissolved in dimethylformamide (DMF) with 15 vol % acetic acid. PVP (molecular weight, ∼1,300,000) was also dissolved in (DMF) with a concentration of 10 wt.%. The salt solution and PVP solution were mixed at a 1:1 ratio in volume to prepare the precursor solution for electrospinning. The salt concentration was ~ 7g per 200mL of PVP/DMF/Acetic Acid solution.

During electrospinning, a high voltage of 20 kV was applied between the needle and the drum collector. The drum collector was connected to the ground. The distance between the needle and the drum collector was 10 cm. The drum collector was covered with foil and above the foil a thin nonwoven fabric to allow removal of the as-spun nanofiber product. Rotation on the drum was not engaged. The fiber was electrospun onto a stationary position. The humidity was required to be less 20% to avoid moisture collection in the fibers and to provide smooth electrospinning of the solution. After electrospinning, the as-spun nanofibers were peeled off the nonwoven fabric and kept in a room-temperature vacuum oven for 24hours before storage in glovebox as multiple layer were required to be spun in order to counter the shrinkage due to calcination. The free-standing nanofiber mat was then calcinated at 800 °C for 2 h in air at a heating rate of 10 °C/min. After the calcination, a garnet nanofiber mat was obtained.

5.5.3 Micelle Template

To induce the millcellization, toluene was added to the DMF polymer and salt solution in a round-bottom flag under stirring at a rate of 1mL per minute either by syringe pump or burette. When 100mLs of toluene was reached a condenser the solution was reflux overnight. After cooling down to ambient temperature, the toluene addition was restarted until the desire volume ratio of DMF was reached $\leq$ 10%. The solution was move to a wide-mouth container for easy decanting and pouring. Hexane was added slowly to crash out the micelles. The micelles were allow to settle by weighting overnight or rarely the solution was centrifuged to remove micelles. The solution was then washed by small amounts ethyl either and dried in vacuum chamber at room temperature.

5.5.4 Characterization

The electrolyte LLZO garnet was imaged using a Hitachi SU-70 Schottky field emission gun Scanning Electron Microscope (FEG-SEM) and a JEOL FEG Transmission Electron Microscope (TEM). TEM samples were prepared and drop-casted on 300 mesh copper grids covered with carbon film. XRD characterization was conducted on Bruker C2/D8 Discover powder diffractometer.

Chapter 6: Conclusion

This dissertation was divided into two studies of nano-structured material fabricated with the aid of polymer. Each study probed fundamental characteristics of two potential battery components, a composite MoS_2-PANI electrode (Chapter 4) and a solid-state $Li_7La_3Zr_2O_{12}$ electrolyte (Chapter 5).

Using the composite electrode, through a combination of the CV and corroborating XPS, we were able to obtain new knowledge on the redox chemistry (and assign CV features)) in a voltage range where this interaction was assumed to be minimal. We demonstrated the presence of sulfur redox chemistry through detailed CV measurements, corroborated by XPS of the composite electrode. Based upon our measurements, we were able to infer that the sulfur formation occurs at the surface of the electrode, where spontaneous sulfur polymerization/electrode coating ensues in the firs cycle. We believe the PANI coating is primarily responsible for the detection sulfur redox couples and the duration of this chemistry can be seen for the lifetime of battery for the first time in for the sodium MoS_2 system. These results were further corroborated by previously reported conformal PEO polymer systems.

With various proposed strategies to utilize MoS_2 in future battery devices, it is important to understand all potential redox reactions that occur in this regime. We developed a methodology to fabricate an alternating polymer MoS_2 structure using a polymer assisted assembly method. We proposed that the conformal coating and the simplicity of our system could be ideal in harnessing the resolving power of cyclic voltammetry (CV). We used the composite electrode to examine the potential sulfur and MoS_2 reactions, and proposed a coupled redox mechanism.

Using two polystyrene-b-polyacrylic acid (PS-b-PAA) copolymer as reverse-micelle template, we investigate the fabrication parameters of cubic $Li_7La_3Zr_2O_{12}$ (c-LLZO) powder and pellets through XRD analysis. C-LLZO materials were successfully synthesized under similar conditions and reproducibility was characterized to varying extents. The garnet quality and composition changes emerged when attempts were made to quantify the composition of sintered the garnet pellet. Although the powder used for the pellet formation was high quality 500 nm size garnet grains, the sintered pellet contain low quantities of c-LLZO. In the case of PS(0.3)-b-PAA(0.7), the pellet composition was approximately 40% of the low conductive tetra-LLZO (t-LLZO) phase. The investigation into the formation of high quality garnet pellets has just begun.

6.1. Future Work

Future studies of TMD redox chemistry could be evaluated using our unique polymer coating procedure. Specifically, ditelluride systems could be investigated for their higher probability than other TMD systems to form anti-bonding pairs, which might also show substantial chalcogenide redox behavior.

For future work in the LLZO system, we suggest further study of the annealing parameters of our low-temperature garnet powders and pellets. The ability for the PS(0.3)-b-PAA(0.7) micelle to form garnet powder and a pellet of approximately 30% cubic garnet phase would suggest that the control of the sintering time could lead to increased garnet composition within the pellet. Furthermore, the optimization of fabrication steps and treatment after the pellet preparation should as acid washes could reduce the lithium carbonate phase and lead to potential increase in conductivity. A potential fabrication step in need of optimization is the ethyl ether washing step, which is predicted to remove some of the critical $LiNO_3$ salt. The optimization of this step would allow increase lithium content which would promote a high abundance of the garnet $Li_7La_3Zr_2O_{12}$ within a pellet.

6.2. Contribution to Society

These studies contributes to a greater understanding of fundamental properties of inorganic materials that can be determined by polymers used in the fabrication or assembly stages of nanomaterials. The findings in this dissertation have direct implications electrical energy storage for improving sulfur utilization in sulfur batteries or preparation of more amorphous LLZO with varying lithium mobility.

The impact of this work is not limited to batteries, but can expanded into potential binding studies of biological samples to sulfur or the detection of sulfide analytes in various environmental samples. Sulfur is chemistry vital to many industrial and biological processes. Our electrode composite offers the ability to promote and detect sulfur redox continuously at a surface could lead to greater understanding of role sulfur plays in various systems. Likewise, the LLZO material could provide a tool to study its selectivity with lithium ions, such as a filter with high lithium mobile could restrict other ions or atoms providing potential to be as a filter.

Appendices

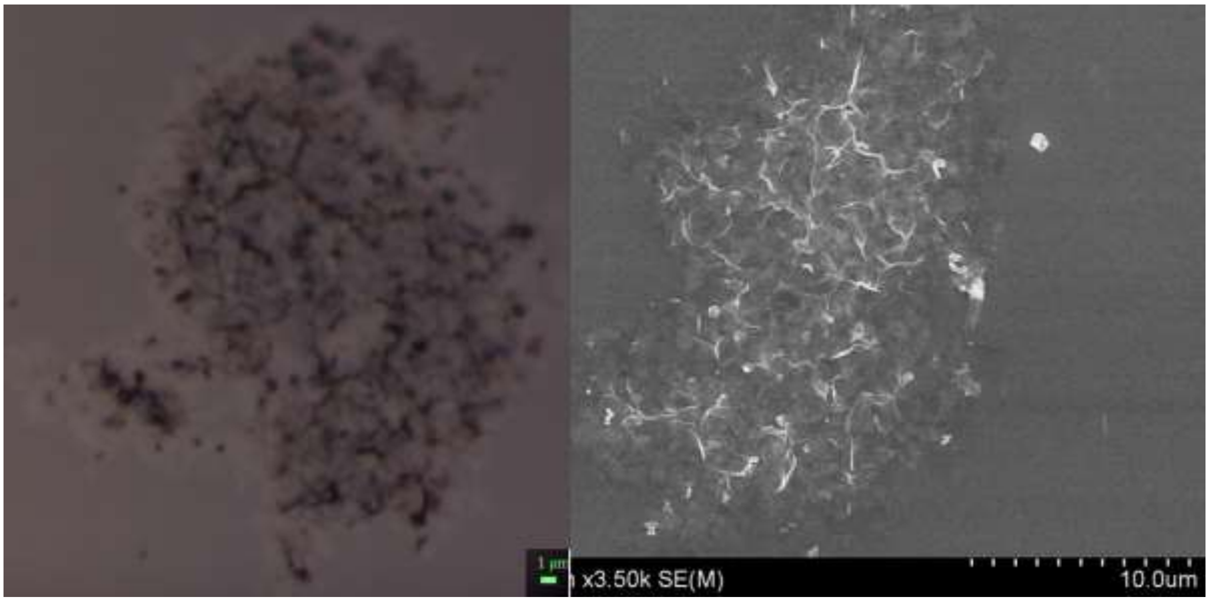

A.1 Optical and SEM image of 10 µm MoS_2 monolayer flake exfoliated through electrochemical sodium insertion and exfoliated with hydration of lithium ions.

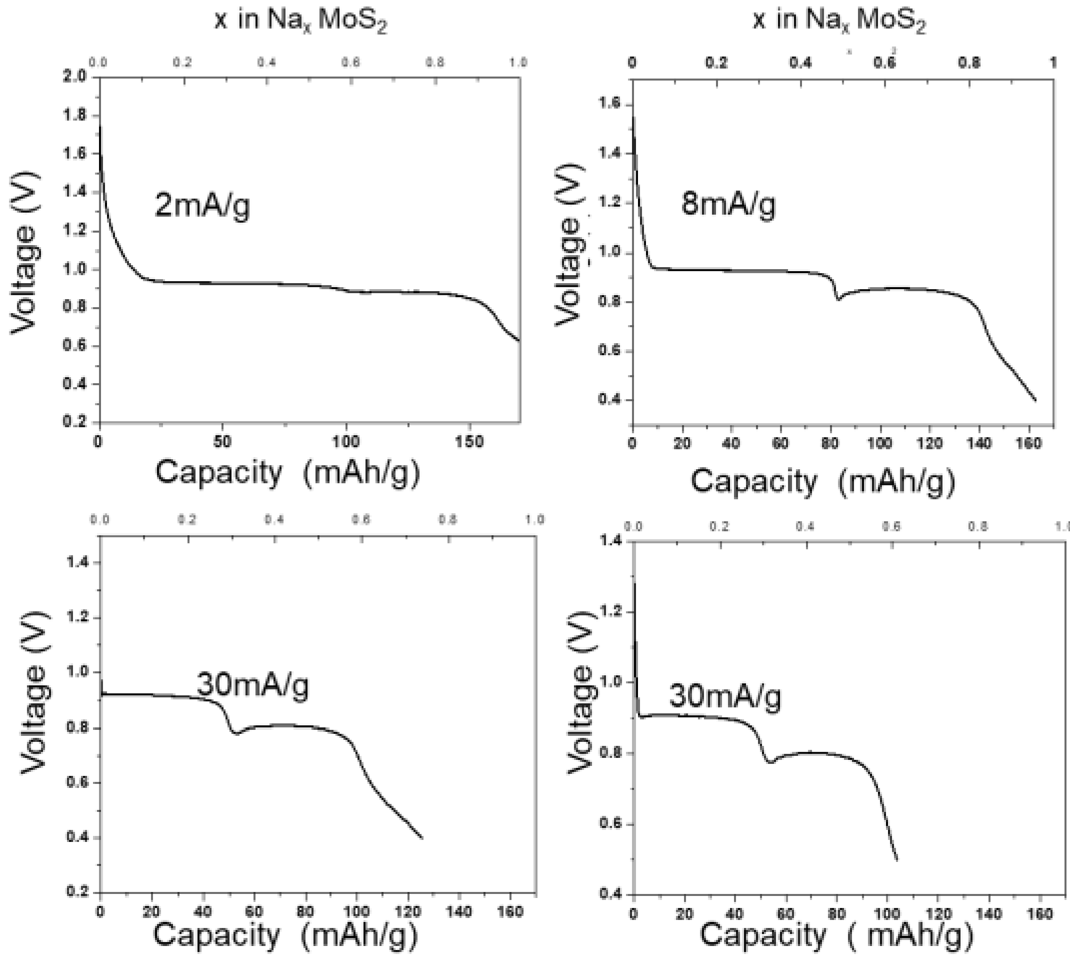

A.2 The first discharge capacity with under different current rates. The discharge dependence on the current suggestions the presence of an electrochemically active species.

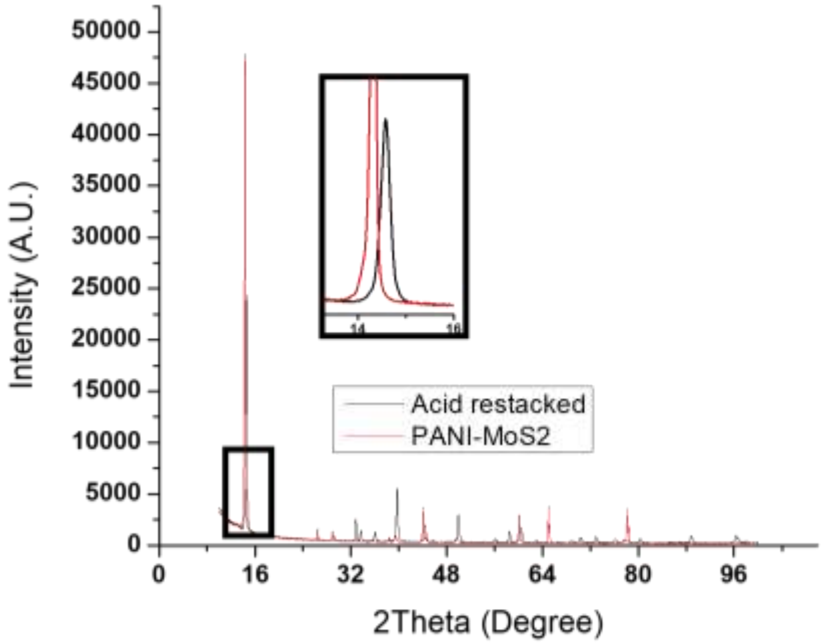

A.3. XRD spectra compares the spectra of restacked few-layer MoS_2 sheets induced by acid to the spectra of polyaniline modified then restacked few-layer MoS_2 sheets. The inset shows a shift of MoS_2-PANI to lower 2θ, which corresponds to an increase in the interlayer spacing in real space. The increase suggest PANI resides within the laminar structure.

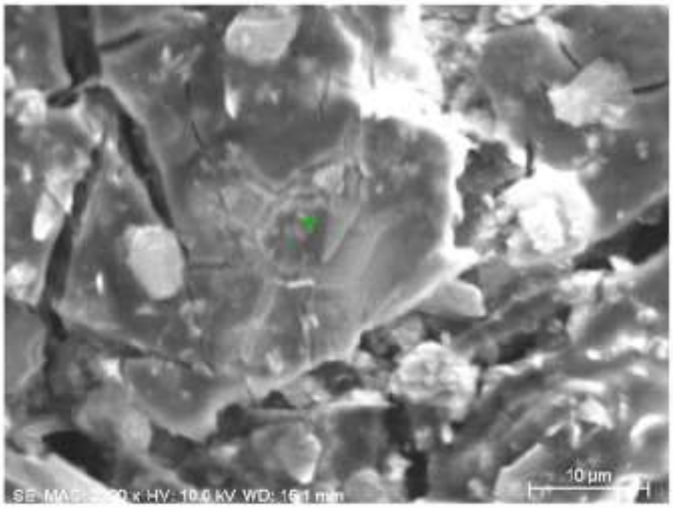

El	AN	Series	unn. C [wt.%]	norm. C [wt.%]	Atom. C [at.%]	Error [%]
C	6	K-series	0.00	0.00	0.00	0.0
N	7	K-series	40.68	47.03	73.79	5.5
Al	13	K-series	17.89	20.69	16.85	0.8
S	16	K-series	3.72	4.30	2.95	2.7
Mo	42	L-series	24.20	27.98	6.41	4.3
		Total:	86.49	100.00	100.00	

A.4. SEM image shows the surface of uncycled MoS_2-PANI electrode. Elemental analysis reveals (highlighted) the presence of nitrogen on the surface, indicating polyaniline modification. However, the analysis cannot be used to estimate molar ratios.

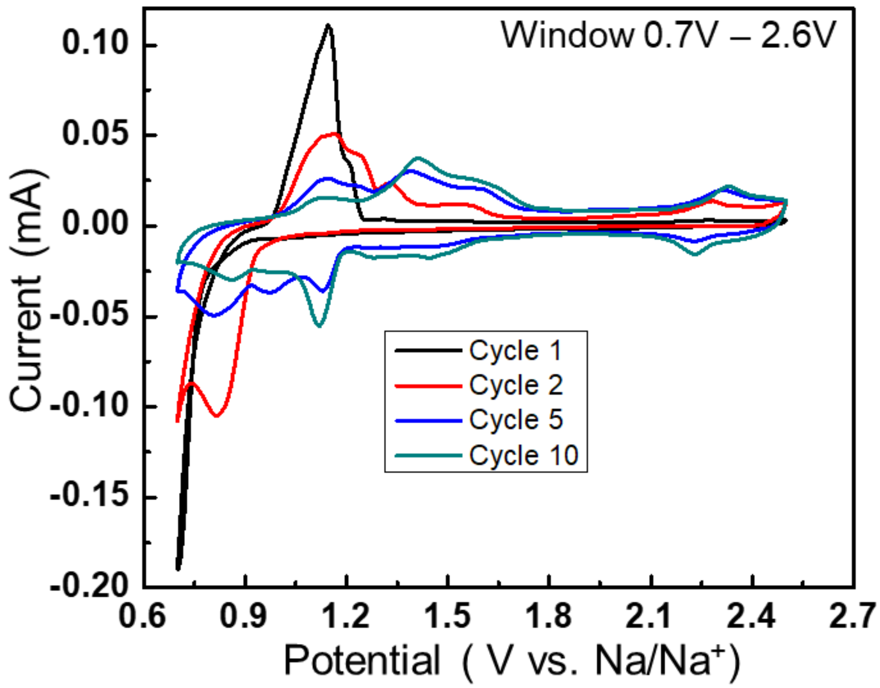

A.5. Cyclic voltammetry of MoS_2-PANI in the voltage window 0.7-2.6 V vs. Na/Na+ which shows similar peaks to that of figure 2.2. The trend in peak decline and increase of peak appears more drastic than the systematic, gradual decline and increase of anodic peak at 1.0 V and 1.34 V respectively. The anodic peak at 1.0 from the 1^{st} cycle transforms into a shoulder in the 2^{nd} cycle. The anodic peak at 1.34 V goes from a flat plateau to small peak.

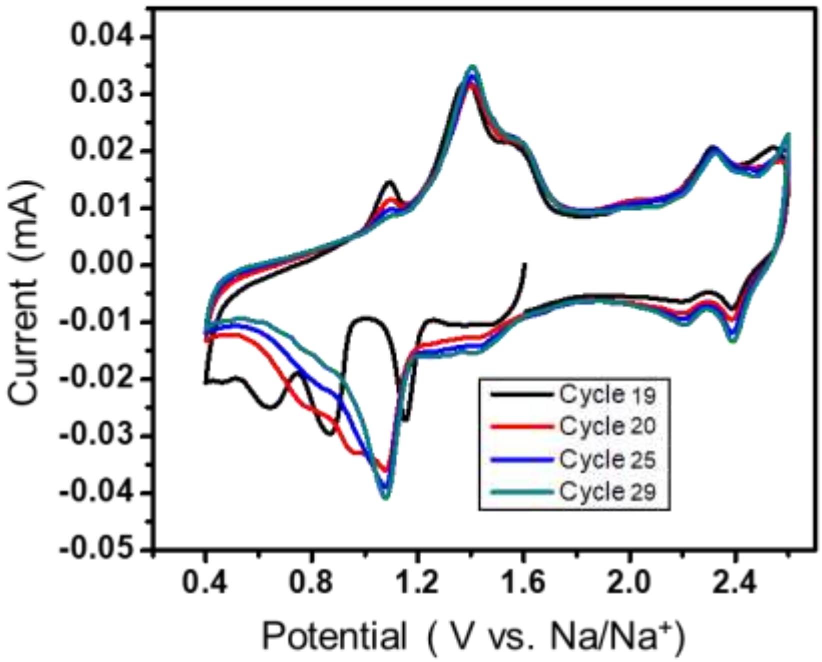

A.6. Cyclic voltammetry of MoS_2-PANI (20% wt.) Na-ion half-cells where cycling has continued on the same battery (figure 2.2). The lower bound of the voltage window is lowered to 0.4, which makes the window 0.4-2.6 V vs. Na/Na^+ at a scan rate of 0.1 mA/s

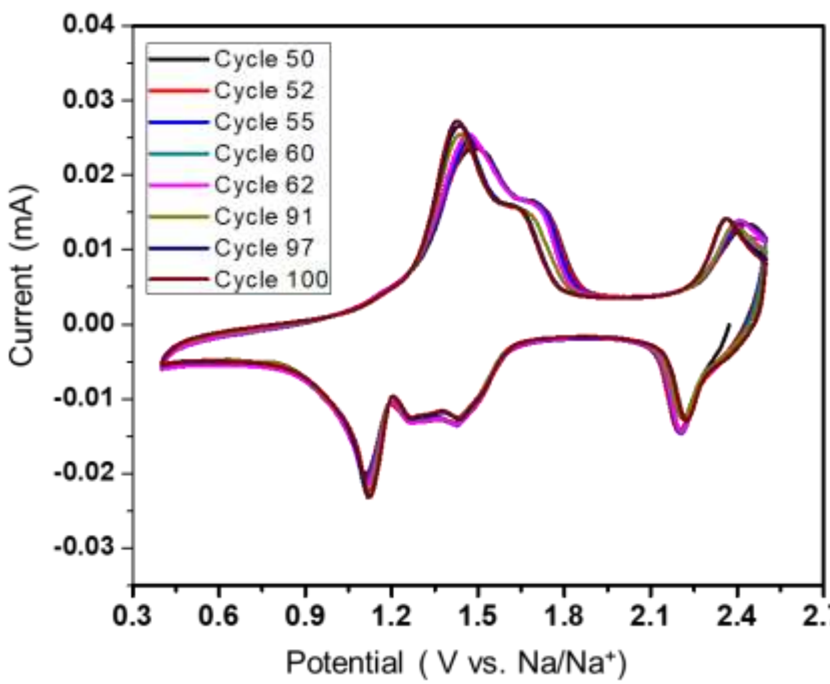

A.7. Extended cyclic voltammetry of MoS_2-PANI (20% wt.) peak current remains constant after 50 and 100 cycles showing that the electrode material is stable. The highlighted features to fluctuates slightly which suggests that major contribution for irreversibility might be influence by Na_2S_{3-4} polysulfides (1.6 V) and longer chain polysulfides (2.4 V). The changes in the peak (1.3 V) can be interpreted as Na_2S_{3-4} conversion to Na_2S_2 on subsequent cycles.

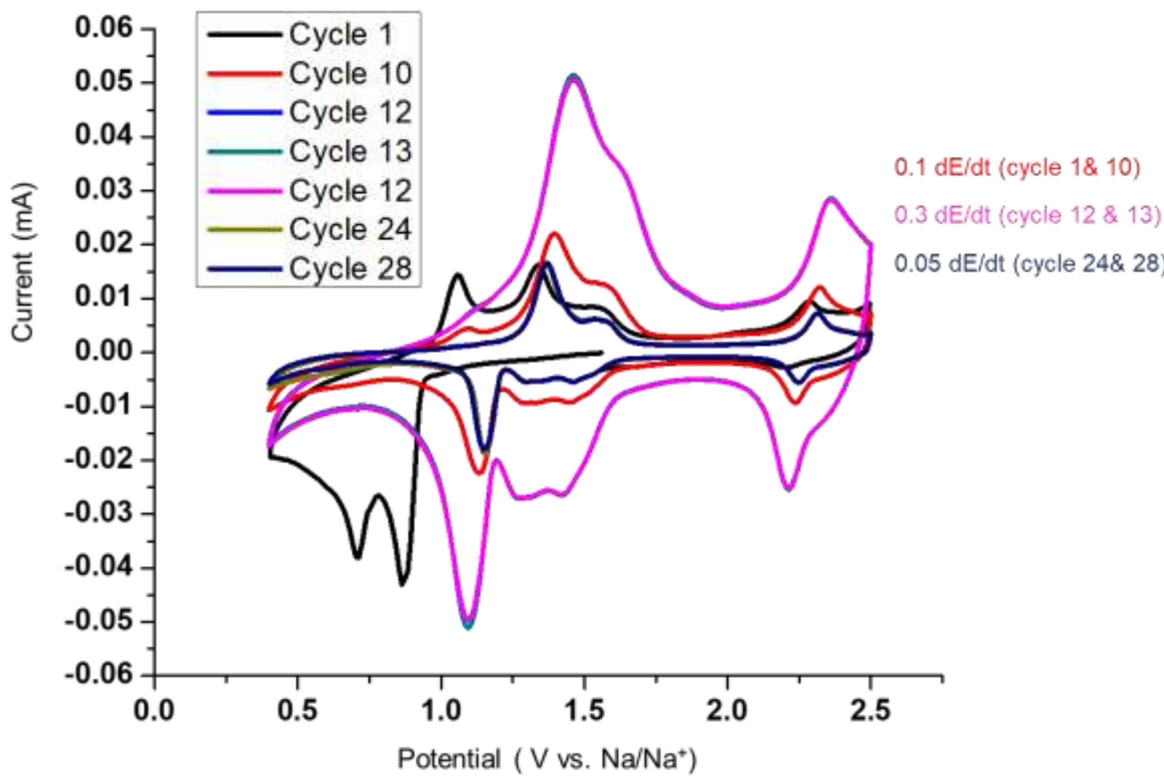

Rate 0.05 mV/s

Intermediate: S_x^{2-}	i_{pa}/i_{pc}	Oxidation	Reduction
		0.9 V – 1.9 V	
Na_2S	0.017/0.0180 =~ 1	(1.37 V, 0.017)	(1.14 V, 0.0180)
Na_2S_{1-2}	0.006/0.005 = ~1.2	(1.50 V, 0.006)	AVG (1.38 V, 0.005)
Na_2S_{2-4}	0.0035/0.006 = ~0.6	(2.31, 0.0073)	2.23 V (2.24 V, 0.006)
$Na_2S_{5\leq x}$		(2.5 V, 0.0035)	2.23 V (2.24 V, 0.006)

Rate 0.1 m V/s

	i_{pa}/i_{pc}	Oxidation	Reduction
Intermediate: S_x^{2-}			
Na_2S	0.0221/0.0224 = ~1	(1.39 V ,0.0221)	(1.13 V, 0.0224)
Na_2S_{1-2}	0.0125/0.009 = ~1.4	(1.57 V ,0.0125)	AVG (1.38 V, 0.009)
Na_2S_{2-4}	0.0121/0.0935 = ~0.13	(2.33 V, 0.0121)	2.23 V (2.23 V, 0.0935)
$Na_2S_{5\leq x}$		(2.50, 0.007)	2.23 V (2.23 V, 0.0935)

Rate 0.3 mV/s

	i_{pa}/i_{pc}	Oxidation	Reduction
Intermediate: S_x^{2-}			
Na_2S	0.0505/0.0490 = ~1	1.39 V (1.47 V, 0.0505)	1.12 V (1.08 V, 0.0490)
Na_2S_{1-2}	0.0351/0.0256 = ~1.4	1.50 V (1.62 V, 0.0351)	AVG(1.36 V, 0.0256)
Na_2S_{2-4}	0.0283/0.0251 = ~1.1	(2.37 V, 0.0283)	2.23 V(2.21 V, 0.0251)
$Na_2S_{5\leq x}$		(2.50 V, 0.0203)	2.23 V(2.21 V, 0.0251)

A.8. Extended cyclic voltammetry of MoS_2-PANI (20% wt.) at varying rates. The charts above display the major peaks

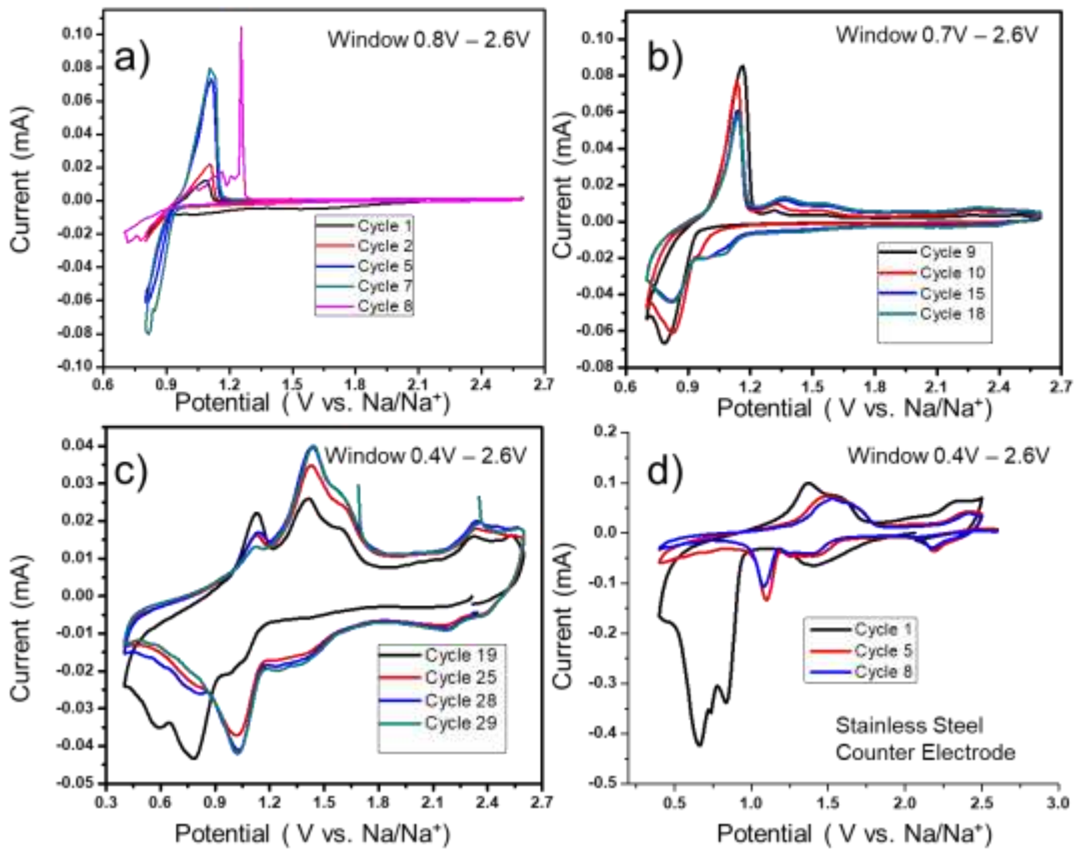

A.9. Cyclic voltammetry conducted at a scan rate of 0.1 mA/s of MoS_2-PANI electrodes. a-c Display the profile of continuous cycling test of MoS_2-PANI (40% wt.) Na-ion half-cells where the cut-off voltage begins at 0.8 V and is lower to 0.7 and 0.4 sequentially. The lower bound of the voltage window is lowered to 0.4, which makes the window 0.4-2.6 V vs. Na/Na^+. d) to rule out an influence of the current collector a stainless steel current collector was substituted, but the slurry could not adhere well to the surface.

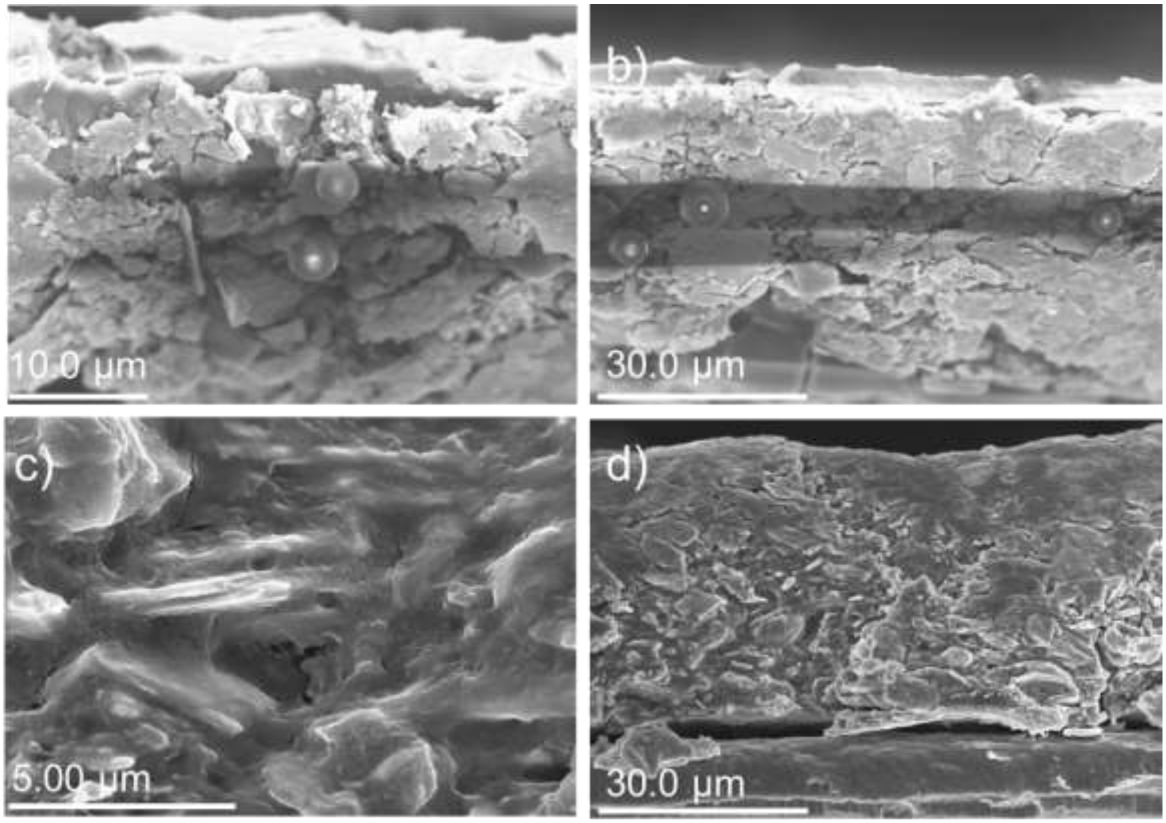

A.10. SEM cross section of 40% MoS_2-PANI battery electrode a) before and b) after cycling. Attempts to increase the amount of aniline absorption to improve sensing capabilities did not work. Instead, increasing the amount of aniline during the polymerization processes leads to fiber formation, which reduces the redox enhancement and sensing capabilities.

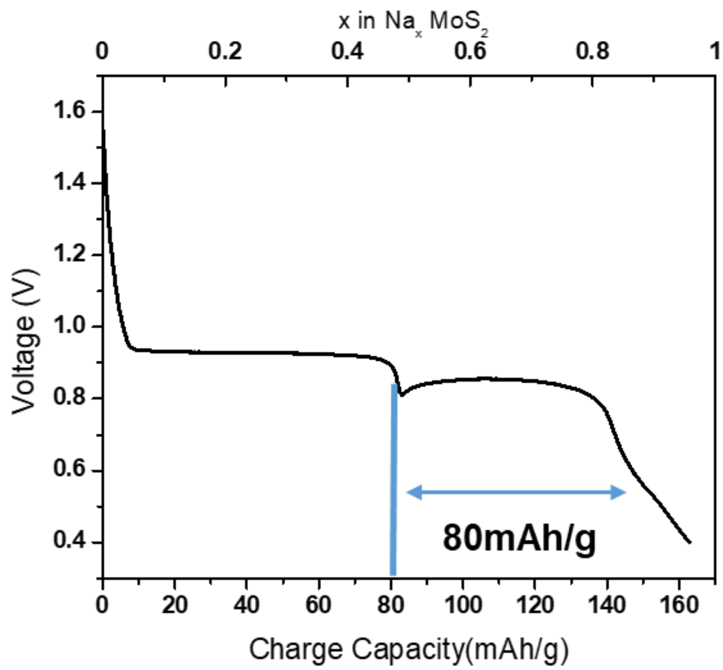

A.11. Though the composition of the MoS_2 hybrid electrode varies both in the size of the as purchased powder (130nm -10uM) and layers 3-5 layers the battery profile matches extremely well for the first sodiation cycle with that of Park's data from literature. The first discharge profile shows the presence of three plateaus starting at 1.2V, 1.5V and 2.2V, with the 1.5V plateau matching that of the most recent literature, which shows features in the 1.5-1.8 range

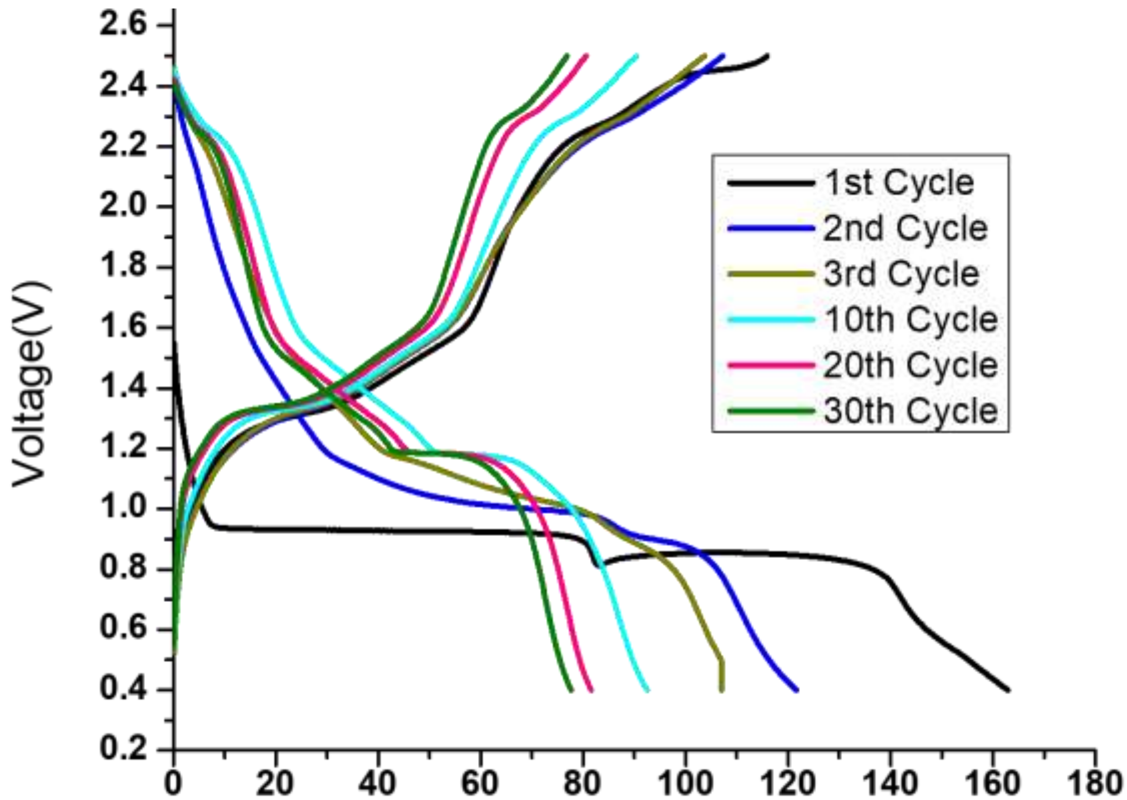

A.12. Standard Charge and discharge curves for MoS_2-PANI batteries. The first discharge cycle (sodiation) capacity ranges from 130-160 mAh/g. The second cycle shows a 25 percent drop of from the first.

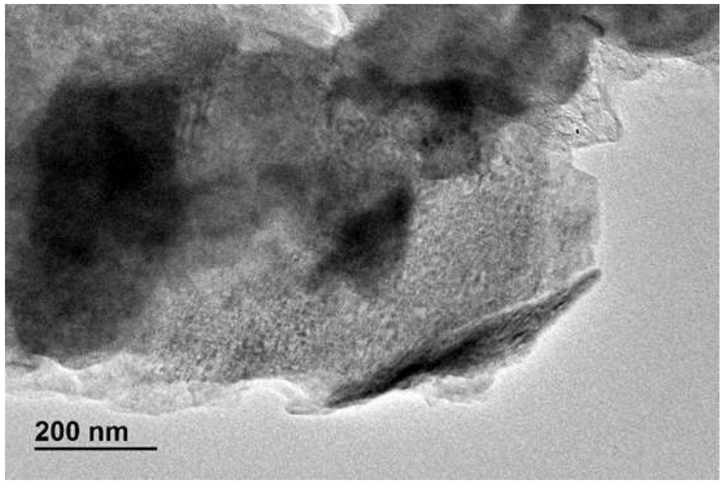

A.13. TEM of a cycled MoS_2-PANI electrode. The lattice fringes in the darker and overlapping areas are contrast with a growing amorphous region in the center of the sheet.

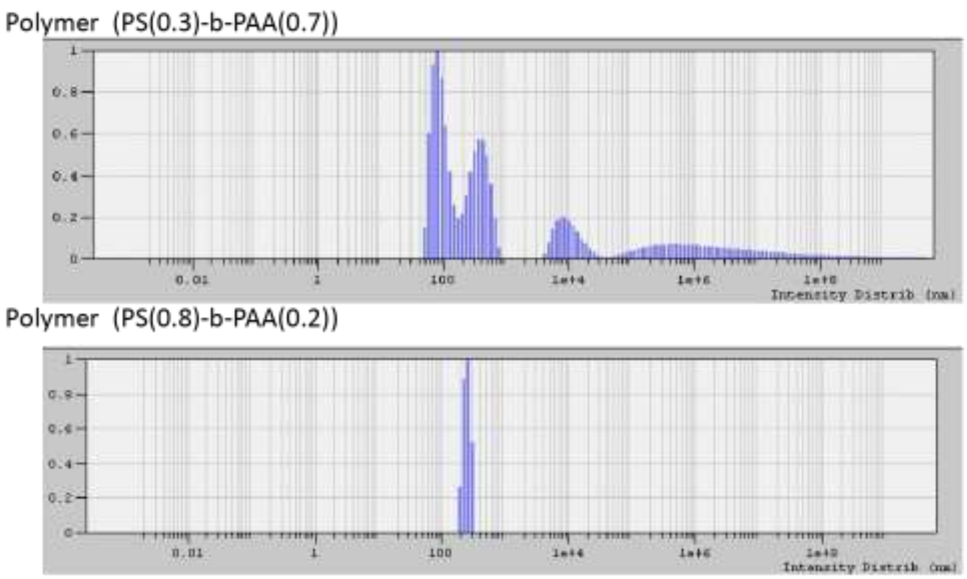

A.14. Dynamic Light Scattering technique confirms the populations of micelles of the precursor solution.

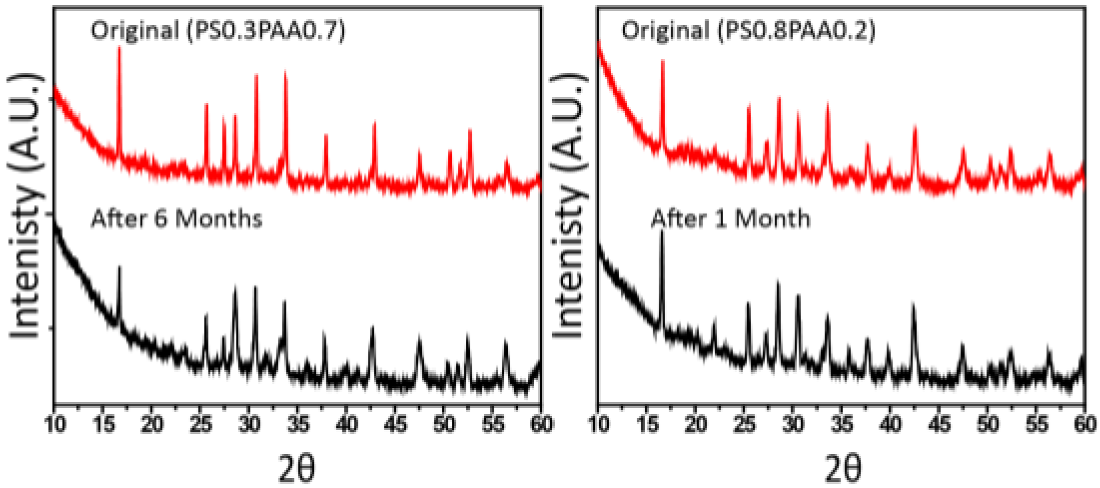

A.15. Comparisons of XRD spectra from various micelle-templated nano-structured garnet showing the stability against air during the XRD analysis, transport, sample preparation, and sample storage over months.

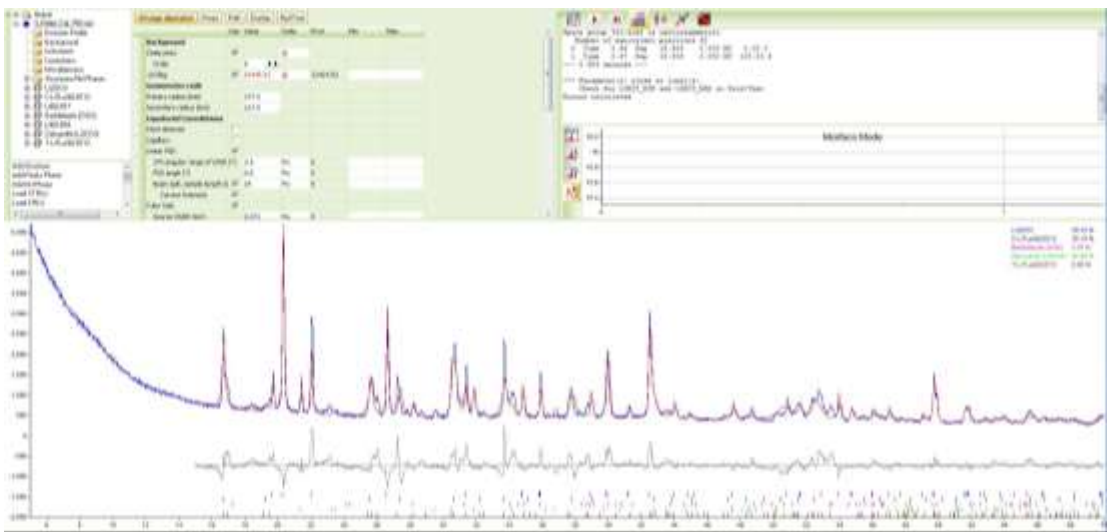

A.16. A caption of the TOPAS 4.2 software window showing the estimated composition of each phase after a Rietveld refinement.

Initial Mass:	Garnet Phase:
0.3000 g	+ $La_2Zr_2O_7$ /$Li_7La_3Zr_2O_{12}$
1.2000 g	- $La_2Zr_2O_7$
0.6700 g	+ $Li_7La_3Zr_2O_{12}$/ $La_2Zr_2O_7$

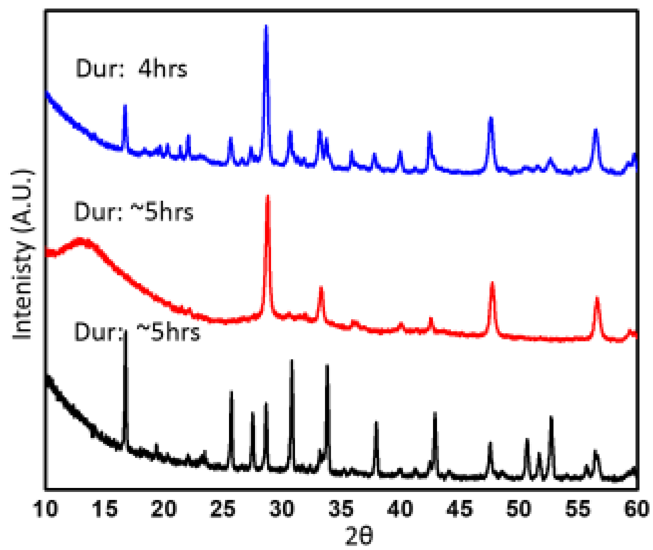

A.17. Figure displaying the mass dependent behavior on the nano-structured garnet product, where the annealing process, precursor composition, polymer system (PS (0.3)-b-PAA(0.7)) are fixed.

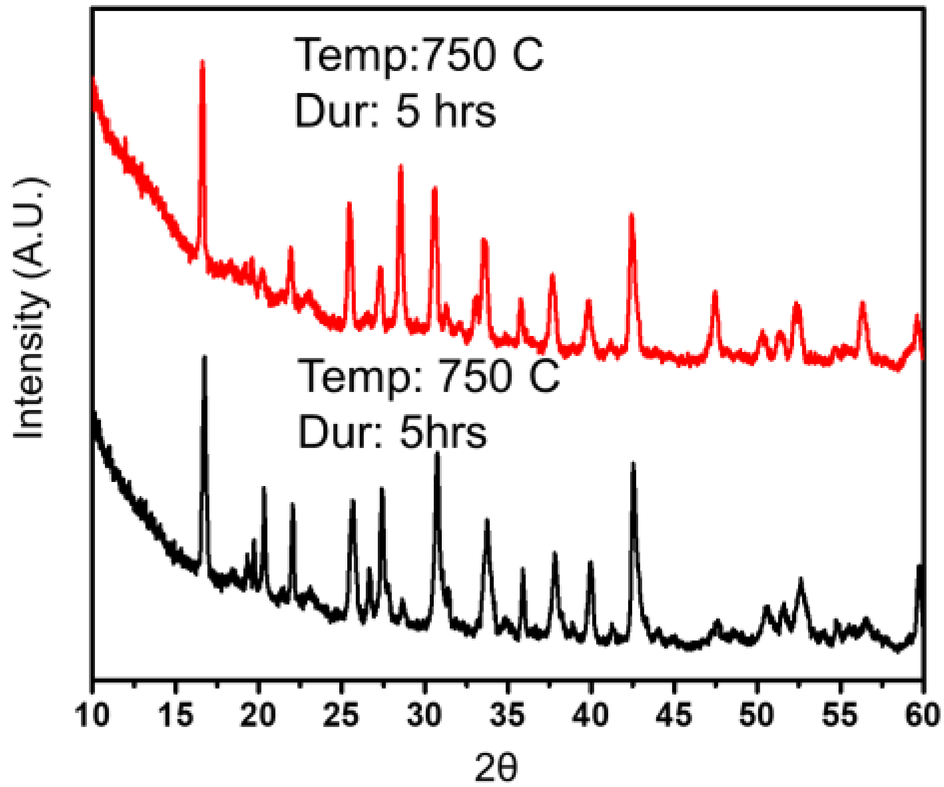

A.18. Comparison of XRD spectra from nano-structured LLZO products where the batch, mass (300 mg), and annealing process remain constant to evaluate the repeatability of the reverse micelle process.

Bibliography

1. Butt, H.; Yetisen, A. K.; Mistry, D.; Khan, S. A.; Hassan, M. U.; Yun, S. H., Morpho Butterfly-Inspired Nanostructures. *Advanced Optical Materials* **2016,** *4* (4), 497-504.
2. Li, X.; Sun, X., Nanostructured Materials for Li-Ion Batteries and Beyond. *Nanomaterials (Basel, Switzerland)* **2016,** *6* (4), 63.
3. Fang, X.; Hua, C.; Guo, X.; Hu, Y.; Wang, Z.; Gao, X.; Wu, F.; Wang, J.; Chen, L., Lithium storage in commercial MoS2 in different potential ranges. *Electrochim. Acta* **2012,** *81* (0), 155-160.
4. Sha, C.; Lu, B.; Mao, H.; Cheng, J.; Pan, X.; Lu, J.; Ye, Z., 3D ternary nanocomposites of molybdenum disulfide/polyaniline/reduced graphene oxide aerogel for high performance supercapacitors. *Carbon* **2016,** *99*, 26-34.
5. Li, Y.; Liang, Y.; Robles Hernandez, F. C.; Deog Yoo, H.; An, Q.; Yao, Y., Enhancing sodium-ion battery performance with interlayer-expanded MoS2–PEO nanocomposites. *Nano Energy* **2015,** *15*, 453-461.
6. Wang, Y.-X.; Chou, S.-L.; Wexler, D.; Liu, H.-K.; Dou, S.-X., High-Performance Sodium-Ion Batteries and Sodium-Ion Pseudocapacitors Based on MoS2/Graphene Composites. *Chem. Eur. J.* **2014,** *20* (31), 9607-9612.
7. Xuefeng, W.; Yejing, L.; Zhaoruxin, G.; Zhaoxiang, W.; Liquan, C., Micro-MoS2 with Excellent Reversible Sodium-Ion Storage. *Chem. Eur. J.* **2015,** *21* (17), 6465-6468.
8. Fu, K.; Gong, Y.; Dai, J.; Gong, A.; Han, X.; Yao, Y.; Wang, C.; Wang, Y.; Chen, Y.; Yan, C.; Li, Y.; Wachsman, E. D.; Hu, L., Flexible, solid-state, ion-conducting membrane with 3D garnet nanofiber networks for lithium batteries. *Proc. Natl. Acad. Sci.* **2016,** *113* (26), 7094.
9. Liu, Y.; He, X.; Hanlon, D.; Harvey, A.; Khan, U.; Li, Y.; Coleman, J. N., Electrical, Mechanical, and Capacity Percolation Leads to High-Performance MoS2/Nanotube Composite Lithium Ion Battery Electrodes. *ACS Nano* **2016,** *10* (6), 5980-5990.
10. Zhang, H.; Zhao, H.; Khan, M. A.; Zou, W.; Xu, J.; Zhang, L.; Zhang, J., Recent progress in advanced electrode materials, separators and electrolytes for lithium batteries. *Journal of Materials Chemistry A* **2018,** *6* (42), 20564-20620.
11. Zhan, H.; Xiao, J.; Nie, Z.; Li, X.; Wang, C.; Zhang, J.-G.; Liu, J., Nanostructured materials for rechargeable batteries: synthesis, fundamental understanding and limitations. *Current Opinion in Chemical Engineering* **2013,** *2* (2), 151-159.
12. Guan, C.; Wang, J., Recent Development of Advanced Electrode Materials by Atomic Layer Deposition for Electrochemical Energy Storage. *Advanced Science* **2016,** *3* (10).
13. Cölfen, H.; Mann, S., Higher-Order Organization by Mesoscale Self-Assembly and Transformation of Hybrid Nanostructures. *Angew. Chem., Int. Ed.* **2003,** *42* (21), 2350-2365.

14. Wang, R.; Gao, S.; Wang, K.; Zhou, M.; Cheng, S.; Jiang, K., MoS2@rGO Nanoflakes as High Performance Anode Materials in Sodium Ion Batteries. *Scientific Reports* **2017,** *7* (1), 7963.
15. Yu, L.; Wang, Q.; Yang, H.; Zhang, Q.; Luo, Z., Facile synthesis and enhanced electrochemical properties of reduced graphene oxide/MoS2/polyaniline ternary composites. *Dalton Trans.* **2017,** *46* (30), 9868-9874.
16. Kumar, P., Directed Self-Assembly: Expectations and Achievements. *Nanoscale Res Lett* **2010,** *5* (9), 1367-1376.
17. Bommier, C.; Ji, X., Electrolytes, SEI Formation, and Binders: A Review of Nonelectrode Factors for Sodium‐Ion Battery Anodes. *Small* **2018,** *14* (16).
18. Xiao, J.; Choi, D.; Cosimbescu, L.; Koech, P.; Liu, J.; Lemmon, J. P., Exfoliated MoS2 Nanocomposite as an Anode Material for Lithium Ion Batteries. *Chem. Mater.* **2010,** *22* (16), 4522-4524.
19. Ryu, W.-H.; Jung, J.-W.; Park, K.; Kim, S.-J.; Kim, I.-D., Vine-like MoS2 anode materials self-assembled from 1-D nanofibers for high capacity sodium rechargeable batteries. *Nanoscale* **2014,** *6* (19), 10975-10981.
20. Wang, J.; Luo, C.; Gao, T.; Langrock, A.; Mignerey, A. C.; Wang, C., An Advanced MoS2/Carbon Anode for High-Performance Sodium-Ion Batteries. *Small* **2015,** *11* (4), 473-481.
21. Jiao, Y.; Mukhopadhyay, A.; Ma, Y.; Yang, L.; Hafez, A. M.; Zhu, H., Ion Transport Nanotube Assembled with Vertically Aligned Metallic MoS2 for High Rate Lithium‐Ion Batteries. *Advanced Energy Materials* **2018,** *8* (15).
22. David, L.; Bhandavat, R.; Singh, G., MoS2/Graphene Composite Paper for Sodium-Ion Battery Electrodes. *ACS Nano* **2014,** *8* (2), 1759-1770.
23. Hu, L.; Ren, Y.; Yang, H.; Xu, Q., Fabrication of 3D Hierarchical MoS2/Polyaniline and MoS2/C Architectures for Lithium-Ion Battery Applications. *ACS Appl. Mater. Interfaces* **2014,** *6* (16), 14644-14652.
24. Nitta, N.; Wu, F.; Lee, J. T.; Yushin, G., Li-ion battery materials: present and future. *Materials Today* **2015,** *18* (5), 252-264.
25. Sahu, T. S.; Mitra, S., Exfoliated MoS2 Sheets and Reduced Graphene Oxide-An Excellent and Fast Anode for Sodium-ion Battery. *Scientific Reports* **2015,** *5*, 12571.
26. Stephenson, T.; Li, Z.; Olsen, B.; Mitlin, D., Lithium ion battery applications of molybdenum disulfide (MoS2) nanocomposites. *Energy & Environmental Science* **2014,** *7* (1), 209-231.
27. Xiao, J.; Wang, X.; Yang, X.-Q.; Xun, S.; Liu, G.; Koech, P. K.; Liu, J.; Lemmon, J. P., Electrochemically Induced High Capacity Displacement Reaction of PEO/MoS2/Graphene Nanocomposites with Lithium. *Adv. Funct. Mater.* **2011,** *21* (15), 2840-2846.
28. Bugga, R. V.; Jones, S. C.; Pasalic, J.; Seu, C. S.; Jones, J.-P.; Torres, L., Metal Sulfide-Blended Sulfur Cathodes in High Energy Lithium-Sulfur Cells. *J. Electrochem. Soc.* **2017,** *164* (2), A265-A276.
29. Julien, C.; Gholam-Abbas, N., *Solid State Batteries: Materials Design and Optimization.* . Springer Verlag: 2014.
30. Whittingham, M. S., Chemistry of intercalation compounds: Metal guests in chalcogenide hosts. *Prog. Solid State Chem.* **1978,** *12* (1), 41-99.

31. Hu, Z.; Wang, L.; Zhang, K.; Wang, J.; Cheng, F.; Tao, Z.; Chen, J., MoS2 Nanoflowers with Expanded Interlayers as High-Performance Anodes for Sodium-Ion Batteries. *Angew. Chem., Int. Ed.* **2014,** *53* (47), 12794-12798.
32. Joensen, P.; Frindt, R. F.; Morrison, S. R., Single-layer MoS2. *Mater. Res. Bull.* **1986,** *21* (4), 457-461.
33. Cao, R.; Zhuang, Q.-C.; Tian, L.-L.; Qiu, X.-Y.; Shi, Y.-L., Electrochemical impedance spectroscopic study of the lithium storage mechanism in commercial molybdenum disulfide. *Ionics* **2014,** *20* (4), 459-469.
34. Chang, K.; Chen, W., l-Cysteine-Assisted Synthesis of Layered MoS2/Graphene Composites with Excellent Electrochemical Performances for Lithium Ion Batteries. *ACS Nano* **2011,** *5* (6), 4720-4728.
35. Simon, P.; Gogotsi, Y.; Dunn, B., Where Do Batteries End and Supercapacitors Begin? *Science* **2014,** *343* (6176), 1210-1211.
36. Murugan, R.; Thangadurai, V.; Weppner, W., Fast Lithium Ion Conduction in Garnet-Type Li7La3Zr2O12. *Angew. Chem., Int. Ed.* **2007,** *46* (41), 7778-7781.
37. Liu, Q.; Geng, Z.; Han, C.; Fu, Y.; Li, S.; He, Y.-b.; Kang, F.; Li, B., Challenges and perspectives of garnet solid electrolytes for all solid-state lithium batteries. *J. Power Sources* **2018,** *389*, 120-134.
38. Blanazs, A.; Armes, S. P.; Ryan, A. J., Self-Assembled Block Copolymer Aggregates: From Micelles to Vesicles and their Biological Applications. *Macromol. Rapid Commun.* **2009,** *30* (4‐5), 267-277.
39. Mai, Y.; Eisenberg, A., Self-assembly of block copolymers. *Chem. Soc. Rev.* **2012,** *41* (18), 5969-5985.
40. Hocine, S.; Li, M.-H., Thermoresponsive self-assembled polymer colloids in water. *Soft Matter* **2013,** *9* (25), 5839-5861.
41. Yu, X.; Manthiram, A., Highly Reversible Room-Temperature Sulfur/Long-Chain Sodium Polysulfide Batteries. *The Journal of Physical Chemistry Letters* **2014,** *5* (11), 1943-1947.
42. Liang, K. S.; Chianelli, R. R.; Chien, F. Z.; Moss, S. C., Structure of poorly crystalline MoS2 — A modeling study. *J. Non-Cryst. Solids* **1986,** *79* (3), 251-273.
43. Py, M. A.; Haering, R. R., Structural destabilization induced by lithium intercalation in MoS2 and related compounds. *Can. J. Phys.* **1983,** *61* (1), 76-84.
44. Fan, X.; Xu, P.; Li, Y. C.; Zhou, D.; Sun, Y.; Nguyen, M. A. T.; Terrones, M.; Mallouk, T. E., Controlled Exfoliation of MoS2 Crystals into Trilayer Nanosheets. *J. Am. Chem. Soc.* **2016,** *138* (15), 5143-5149.
45. Koyama, T.; Takayanagi, K.; Togawa, Y.; Mori, S.; Harada, K., Small angle electron diffraction and deflection. *AIP Advances* **2012,** *2* (1), 012195.
46. Bendersky, L. A.; Gayle, F. W., Electron Diffraction Using Transmission Electron Microscopy. *J Res Natl Inst Stand Technol* **2001,** *106* (6), 997-1012.
47. Bard, A. J.; Faulkner, L. R., *Electrochemical methods : fundamentals and applications*. 2nd ed. ed.; Wiley: New York, 2001.
48. Bilal, S., Cyclic Voltammetry. In *Encyclopedia of Applied Electrochemistry*, Kreysa, G.; Ota, K.-i.; Savinell, R. F., Eds. Springer New York: New York, NY, 2014; pp 285-289.

49. Harnisch, F.; Freguia, S., A Basic Tutorial on Cyclic Voltammetry for the Investigation of Electroactive Microbial Biofilms. *Chemistry – An Asian Journal* **2012,** *7* (3), 466-475.
50. Elgrishi, N.; Rountree, K. J.; McCarthy, B. D.; Rountree, E. S.; Eisenhart, T. T.; Dempsey, J. L., A Practical Beginner's Guide to Cyclic Voltammetry. *J. Chem. Educ.* **2018,** *95* (2), 197-206.
51. Cardoso, M. J. R.; Lima, M. F. S.; Lenz, D. M., Polyaniline synthesized with functionalized sulfonic acids for blends manufacture. *Mat. Res.* **2007,** *10*, 425-429.
52. Stejskal, J.; Sapurina, I., Polyaniline: Thin films and colloidal dispersions (IUPAC Technical Report). In *Pure Appl. Chem.*, 2005; Vol. 77, p 815.
53. Vachon, D.; Angus, R. O.; Lu, F. L.; Nowak, M.; Liu, Z. X.; Schaffer, H.; Wudl, F.; Heeger, A. J., Polyaniline is poly-para-phenyleneamineimine: proof of structure by synthesis. *Synth. Met.* **1987,** *18* (1), 297-302.
54. Sapurina, I.; Stejskal, J., The mechanism of the oxidative polymerization of aniline and the formation of supramolecular polyaniline structures. *Polym. Int.* **2008,** *57* (12), 1295-1325.
55. Li, D.; Kaner, R. B., Shape and Aggregation Control of Nanoparticles: Not Shaken, Not Stirred. *J. Am. Chem. Soc.* **2006,** *128* (3), 968-975.
56. Zhang, S. S., The redox mechanism of FeS2 in non-aqueous electrolytes for lithium and sodium batteries. *Journal of Materials Chemistry A* **2015,** *3* (15), 7689-7694.
57. Acrivos, J. V.; Liang, W. Y.; Wilson, J. A.; Yoffe, A. D., Optical studies of metal-semiconductor transmutations produced by intercalation. *Journal of Physics C: Solid State Physics* **1971,** *4* (1), L18.
58. Wang, Q. H.; Kalantar-Zadeh, K.; Kis, A.; Coleman, J. N.; Strano, M. S., Electronics and optoelectronics of two-dimensional transition metal dichalcogenides. *Nat. Nanotechnol.* **2012,** *7*, 699.
59. Cooper, R. C.; Lee, C.; Marianetti, C. A.; Wei, X.; Hone, J.; Kysar, J. W., Nonlinear elastic behavior of two-dimensional molybdenum disulfide. *Physical Review B* **2013,** *87* (3), 035423.
60. Huang, K.-J.; Wang, L.; Liu, Y.-J.; Wang, H.-B.; Liu, Y.-M.; Wang, L.-L., Synthesis of polyaniline/2-dimensional graphene analog MoS2 composites for high-performance supercapacitor. *Electrochim. Acta* **2013,** *109* (0), 587-594.
61. Li, X.; Zhu, H., Two-dimensional MoS2: Properties, preparation, and applications. *Journal of Materiomics* **2015,** *1* (1), 33-44.
62. Tan, C.; Zhang, H., Two-dimensional transition metal dichalcogenide nanosheet-based composites. *Chem. Soc. Rev.* **2015**.
63. Chhowalla, M.; Shin, H. S.; Eda, G.; Li, L.-J.; Loh, K. P.; Zhang, H., The chemistry of two-dimensional layered transition metal dichalcogenide nanosheets. *Nat. Chem.* **2013,** *5*, 263.
64. Brec, R.; Deniard, P.; Rouxel, J., Chalcogenides: Electronic Properties. In *Progress in Intercalation Research*, Schollhorn, R.; Muller-Warmuth, W., Eds. Kluwer Academic Publishers: Netherlands, 1994; pp 177-221.
65. Cheetham, A. K.; Day, P., *Solid state chemistry : compounds*. Clarendon Press ;
Oxford University Press: Oxford [England]

New York, 1992.
66. Lévy, F., *Intercalated layered materials*. D. Reidel Pub. Co.: Dordrecht, Holland ;, 1979.
67. Kanatzidis, M. G.; Bissessur, R.; DeGroot, D. C.; Schindler, J. L.; Kannewurf, C. R., New intercalation compounds of conjugated polymers. Encapsulation of polyaniline in molybdenum disulfide. *Chem. Mater.* **1993,** *5* (5), 595-596.
68. Bissessur, R.; Kanatzidis, M. G.; Schindler, J. L.; Kannewurf, C. R., Encapsulation of polymers into MoS2 and metal to insulator transition in metastable MoS2. *J. Chem. Soc., Chem. Commun.* **1993,** (20), 1582-1585.
69. Coleman, J. N.; Lotya, M.; O'Neill, A.; Bergin, S. D.; King, P. J.; Khan, U.; Young, K.; Gaucher, A.; De, S.; Smith, R. J.; Shvets, I. V.; Arora, S. K.; Stanton, G.; Kim, H.-Y.; Lee, K.; Kim, G. T.; Duesberg, G. S.; Hallam, T.; Boland, J. J.; Wang, J. J.; Donegan, J. F.; Grunlan, J. C.; Moriarty, G.; Shmeliov, A.; Nicholls, R. J.; Perkins, J. M.; Grieveson, E. M.; Theuwissen, K.; McComb, D. W.; Nellist, P. D.; Nicolosi, V., Two-Dimensional Nanosheets Produced by Liquid Exfoliation of Layered Materials. *Science* **2011,** *331* (6017), 568.
70. Somoano, R. B.; Hadek, V.; Rembaum, A.; Samson, S.; Woollam, J. A., The alkaline earth intercalates of molybdenum disulfide. *The Journal of Chemical Physics* **1975,** *62* (3), 1068-1073.
71. Whangbo, M. H.; Rouxel, J.; Trichet, L., Effects of sodium intercalation in titanium disulfide on the electronic structure of a TiS2 slab. *Inorg. Chem.* **1985,** *24* (12), 1824-1827.
72. Benavente, E.; Santa Ana, M. A.; Mendizábal, F.; González, G., Intercalation chemistry of molybdenum disulfide. *Coord. Chem. Rev.* **2002,** *224* (1), 87-109.
73. Hibma, T., X-ray study of the ordering of the alkali ions in the intercalation compounds NaxTiS2 and LixTiS2. *J. Solid State Chem.* **1980,** *34* (1), 97-106.
74. Saitō, S.; Yanagida, H.; Fukunaga, O.; Kogyo-seihin Gijyutsu, K., *Ceramics databook*. Gordon and Breach Science Publishers: New York, 1987.
75. Kertesz, M.; Hoffmann, R., Octahedral vs. trigonal-prismatic coordination and clustering in transition-metal dichalcogenides. *J. Am. Chem. Soc.* **1984,** *106* (12), 3453-3460.
76. Heising, J.; Kanatzidis, M. G., Structure of Restacked MoS2 and WS2 Elucidated by Electron Crystallography. *J. Am. Chem. Soc.* **1999,** *121* (4), 638-643.
77. Julien, C. M., Lithium intercalated compounds: Charge transfer and related properties. *Materials Science and Engineering: R: Reports* **2003,** *40* (2), 47-102.
78. McKinnon, W. R., Insertion electrodes I: Atomic and electronic structure of the hosts and their insertion compounds. In *Solid State Electrochemistry*, 1st paperback ed. ed.; Bruce, P. G., Ed. Cambridge University Press: Cambridge, U.K. ;, 1997; pp 163-196.
79. Liyanage, A. U.; Lerner, M. M., Use of amine electride chemistry to prepare molybdenum disulfide intercalation compounds. *RSC Advances* **2014,** *4* (87), 47121-47128.
80. Castellanos-Gomez, A.; van der Zant, H. S. J.; Steele, G. A., Folded MoS2 layers with reduced interlayer coupling. *Nano Res.* **2014,** *7* (4), 572-578.

81. Wilson, J. A.; Yoffe, A. D., The transition metal dichalcogenides discussion and interpretation of the observed optical, electrical and structural properties. *Advances in Physics* **1969,** *18* (73), 193-335.
82. Jacobson, A. J.; Chianelli, R. R.; Whittingham, M. S., Amorphous Molybdenum Disulfide Cathodes. *J. Electrochem. Soc.* **1979,** *126* (12), 2277-2278.
83. Xu, W.; Yan, S.; Qiao, W., Magnetism in monolayer 1T-MoS2 and 1T-MoS2H tuned by strain. *RSC Advances* **2018,** *8* (15), 8435-8441.
84. Divigalpitiya, W. M. R.; Morrison, S. R.; Frindt, R. F., Thin oriented films of molybdenum disulphide. *Thin Solid Films* **1990,** *186* (1), 177-192.
85. O'Neill, A.; Khan, U.; Coleman, J. N., Preparation of High Concentration Dispersions of Exfoliated MoS2 with Increased Flake Size. *Chem. Mater.* **2012,** *24* (12), 2414-2421.
86. Paton, K. R.; Varrla, E.; Backes, C.; Smith, R. J.; Khan, U.; O'Neill, A.; Boland, C.; Lotya, M.; Istrate, O. M.; King, P.; Higgins, T.; Barwich, S.; May, P.; Puczkarski, P.; Ahmed, I.; Moebius, M.; Pettersson, H.; Long, E.; Coelho, J.; O'Brien, S. E.; McGuire, E. K.; Sanchez, B. M.; Duesberg, G. S.; McEvoy, N.; Pennycook, T. J.; Downing, C.; Crossley, A.; Nicolosi, V.; Coleman, J. N., Scalable production of large quantities of defect-free few-layer graphene by shear exfoliation in liquids. *Nat. Mater.* **2014,** *13* (6), 624-630.
87. Yi, M.; Shen, Z., A review on mechanical exfoliation for the scalable production of graphene. *Journal of Materials Chemistry A* **2015,** *3* (22), 11700-11715.
88. Eda, G.; Yamaguchi, H.; Voiry, D.; Fujita, T.; Chen, M.; Chhowalla, M., Photoluminescence from Chemically Exfoliated MoS2. *Nano Lett.* **2011,** *11* (12), 5111-5116.
89. Liang, X.; Hart, C.; Pang, Q.; Garsuch, A.; Weiss, T.; Nazar, L. F., A highly efficient polysulfide mediator for lithium–sulfur batteries. *Nat. Commun.* **2015,** *6*.
90. Meini, S.; Elazari, R.; Rosenman, A.; Garsuch, A.; Aurbach, D., The Use of Redox Mediators for Enhancing Utilization of Li2S Cathodes for Advanced Li–S Battery Systems. *The Journal of Physical Chemistry Letters* **2014,** *5* (5), 915-918.
91. Pang, Q.; Kundu, D.; Cuisinier, M.; Nazar, L. F., Surface-enhanced redox chemistry of polysulphides on a metallic and polar host for lithium-sulphur batteries. *Nat. Commun.* **2014,** *5*.
92. Wagner, M. W.; Liebenow, C.; Besenhard, J. O., Effect of polysulfide-containing electrolyte on the film formation of the negative electrode. *J. Power Sources* **1997,** *68* (2), 328-332.
93. Whittingham, M. S., Lithium incorporation in crystalline and amorphous chalcogenides: Thermodynamics, mechanism and structure. *Journal of Electroanalytical Chemistry and Interfacial Electrochemistry* **1981,** *118*, 229-239.
94. Park, J.; Kim, J.-S.; Park, J.-W.; Nam, T.-H.; Kim, K.-W.; Ahn, J.-H.; Wang, G.; Ahn, H.-J., Discharge mechanism of MoS2 for sodium ion battery: Electrochemical measurements and characterization. *Electrochim. Acta* **2013,** *92* (0), 427-432.
95. Cook, J. B.; Kim, H.-S.; Yan, Y.; Ko, J. S.; Robbennolt, S.; Dunn, B.; Tolbert, S. H., Mesoporous MoS2 as a Transition Metal Dichalcogenide Exhibiting

Pseudocapacitive Li and Na-Ion Charge Storage. *Advanced Energy Materials* **2016,** *6* (9), 1501937.
96. Besenhard, J. O.; Meyer, H.; Schöllhorn, R., Defined Intercalation Stages from Cathodic Reduction of MoS2 in Organic Electrolytes. In *Zeitschrift für Naturforschung B*, 1976; Vol. 31, p 907.
97. Garsuch, A.; Herzog, S.; Montag, L.; Krebs, A.; Leitner, K., Performance of Blended TiS2/Sulfur/Carbon Cathodes in Lithium-Sulfur Cells. *ECS Electrochemistry Letters* **2012,** *1* (1), A24-A26.
98. Lacey, S. D.; Wan, J.; Cresce, A. v. W.; Russell, S. M.; Dai, J.; Bao, W.; Xu, K.; Hu, L., Atomic Force Microscopy Studies on Molybdenum Disulfide Flakes as Sodium-Ion Anodes. *Nano Lett.* **2015,** *15* (2), 1018-1024.
99. Imanishi, N.; Toyoda, M.; Takeda, Y.; Yamamoto, O., Study on lithium intercalation into MoS2. *Solid State Ionics* **1992,** *58* (3), 333-338.
100. Gigot, A.; Fontana, M.; Serrapede, M.; Castellino, M.; Bianco, S.; Armandi, M.; Bonelli, B.; Pirri, C. F.; Tresso, E.; Rivolo, P., Mixed 1T–2H Phase MoS2/Reduced Graphene Oxide as Active Electrode for Enhanced Supercapacitive Performance. *ACS Appl. Mater. Interfaces* **2016,** *8* (48), 32842-32852.
101. Carter, R.; Oakes, L.; Douglas, A.; Muralidharan, N.; Cohn, A. P.; Pint, C. L., A Sugar-Derived Room-Temperature Sodium Sulfur Battery with Long Term Cycling Stability. *Nano Lett.* **2017,** *17* (3), 1863-1869.
102. Xin, S.; Yin, Y.-X.; Guo, Y.-G.; Wan, L.-J., A High-Energy Room-Temperature Sodium-Sulfur Battery. *Adv. Mater.* **2014,** *26* (8), 1261-1265.
103. Komaba, S.; Murata, W.; Ishikawa, T.; Yabuuchi, N.; Ozeki, T.; Nakayama, T.; Ogata, A.; Gotoh, K.; Fujiwara, K., Electrochemical Na Insertion and Solid Electrolyte Interphase for Hard - Carbon Electrodes and Application to Na - Ion Batteries. *Adv. Funct. Mater.* **2011,** *21* (20), 3859-3867.
104. Li, Q.; Yao, Z.; Wu, J.; Mitra, S.; Hao, S.; Sahu, T. S.; Li, Y.; Wolverton, C.; Dravid, V. P., Intermediate phases in sodium intercalation into MoS2 nanosheets and their implications for sodium-ion batteries. *Nano Energy* **2017,** *38*, 342-349.
105. Wu, C., Inorganic two-dimensional nanomaterials : fundamental understanding, characterizations and energy applications. Royal Society of Chemistry: [Cambridge], 2017. http://dx.doi.org/10.1039/9781788010306
http://search.ebscohost.com/login.aspx?direct=true&scope=site&db=nlebk&db=nlabk&AN=1591833
http://lib.myilibrary.com?id=1035349
http://public.eblib.com/choice/PublicFullRecord.aspx?p=5043111
https://ebookcentral.proquest.com/lib/UWY/detail.action?docID=5043111
http://www.vlebooks.com/vleweb/product/openreader?id=none&isbn=9781788010306.
106. Cai, L.; He, J.; Liu, Q.; Yao, T.; Chen, L.; Yan, W.; Hu, F.; Jiang, Y.; Zhao, Y.; Hu, T.; Sun, Z.; Wei, S., Vacancy-Induced Ferromagnetism of MoS2 Nanosheets. *J. Am. Chem. Soc.* **2015,** *137* (7), 2622-2627.
107. Wenzel, S.; Metelmann, H.; Raiß, C.; Dürr, A. K.; Janek, J.; Adelhelm, P., Thermodynamics and cell chemistry of room temperature sodium/sulfur cells with liquid and liquid/solid electrolyte. *J. Power Sources* **2013,** *243* (0), 758-765.

108. Volkovich, V. A.; Ivanov, A. B.; Kamalov, R. V.; Maltsev, D. S.; Vasin, B. D.; Griffiths, T. R., Electrode and Redox Potentials of Molybdenum and Stability of Molybdenum Chloro-Species in Alkali Chloride Melts. *J. Electrochem. Soc.* **2017,** *164* (8), H5336-H5344.
109. Goto, F.; Asaoka, T.; Okabayashi, K.; Abe, K.; Yoshida, T., Effects of Electrolyte Quantity on the Charge Discharge Characteristic of Polyaniline Lithium Secondary Batteries. *Denki Kagaku* **1989,** *57* (8), 798-805.
110. Huang, J.; Kaner, R. B., A General Chemical Route to Polyaniline Nanofibers. *J. Am. Chem. Soc.* **2004,** *126* (3), 851-855.
111. Tsai, C.-L.; Ma, Q.; Dellen, C.; Lobe, S.; Vondahlen, F.; Windmüller, A.; Grüner, D.; Zheng, H.; Uhlenbruck, S.; Finsterbusch, M.; Tietz, F.; Fattakhova-Rohlfing, D.; Buchkremer, H. P.; Guillon, O., A garnet structure-based all-solid-state Li battery without interface modification: resolving incompatibility issues on positive electrodes. *Sustainable Energy & Fuels* **2019,** *3* (1), 280-291.
112. Huang, X.; Lu, Y.; Song, Z.; Xiu, T.; Badding, M. E.; Wen, Z., Preparation of dense Ta-LLZO/MgO composite Li-ion solid electrolyte: Sintering, microstructure, performance and the role of MgO. *Journal of Energy Chemistry* **2019,** *39*, 8-16.
113. Cheng, L.; Crumlin, E. J.; Chen, W.; Qiao, R.; Hou, H.; Franz Lux, S.; Zorba, V.; Russo, R.; Kostecki, R.; Liu, Z.; Persson, K.; Yang, W.; Cabana, J.; Richardson, T.; Chen, G.; Doeff, M., The origin of high electrolyte–electrode interfacial resistances in lithium cells containing garnet type solid electrolytes. *Phys. Chem. Chem. Phys.* **2014,** *16* (34), 18294-18300.
114. Sakamoto, J.; Rangasamy, E.; Kim, H.; Kim, Y.; Wolfenstine, J., Synthesis of nano-scale fast ion conducting cubic Li7La3Zr2O12. *Nanotechnology* **2013,** *24* (42), 424005.
115. Cheng, L.; Wu, C. H.; Jarry, A.; Chen, W.; Ye, Y.; Zhu, J.; Kostecki, R.; Persson, K.; Guo, J.; Salmeron, M.; Chen, G.; Doeff, M., Interrelationships among Grain Size, Surface Composition, Air Stability, and Interfacial Resistance of Al-Substituted Li7La3Zr2O12 Solid Electrolytes. *ACS Appl. Mater. Interfaces* **2015,** *7* (32), 17649-17655.
116. Fu, K.; Gong, Y.; Hitz, G. T.; McOwen, D. W.; Li, Y.; Xu, S.; Wen, Y.; Zhang, L.; Wang, C.; Pastel, G.; Dai, J.; Liu, B.; Xie, H.; Yao, Y.; Wachsman, E. D.; Hu, L., Three-dimensional bilayer garnet solid electrolyte based high energy density lithium metal–sulfur batteries. *Energy & Environmental Science* **2017,** *10* (7), 1568-1575.
117. Yang, T.; Gordon, Z. D.; Li, Y.; Chan, C. K., Nanostructured Garnet-Type Solid Electrolytes for Lithium Batteries: Electrospinning Synthesis of Li7La3Zr2O12 Nanowires and Particle Size-Dependent Phase Transformation. *The Journal of Physical Chemistry C* **2015,** *119* (27), 14947-14953.
118. Jiang, B.; Li, C.; Tang, J.; Takei, T.; Kim, J. H.; Ide, Y.; Henzie, J.; Tominaka, S.; Yamauchi, Y., Tunable-Sized Polymeric Micelles and Their Assembly for the Preparation of Large Mesoporous Platinum Nanoparticles. *Angew. Chem., Int. Ed.* **2016,** *55* (34), 10037-10041.
119. Tang, Y.; Luo, Z.; Liu, T.; Liu, P.; Li, Z.; Lu, A., Effects of B2O3 on microstructure and ionic conductivity of Li6.5La3Zr1.5Nb0.5O12 solid electrolyte. *Ceram. Int.* **2017,** *43* (15), 11879-11884.

120. Xie, H.; Li, Y.; Goodenough, J. B., Low-temperature synthesis of $Li_7La_3Zr_2O_{12}$ with cubic garnet-type structure. *Mater. Res. Bull.* **2012,** *47* (5), 1229-1232.